8-2014

Fatigue-Induced Failure in Horizontal-Axis Wind-Turbine (HAWT) Blades and HAWT Drivetrain Gears

Varun Chenna
Clemson University, vchenna@g.clemson.edu

FATIGUE–INDUCED FAILURE IN HORIZONTAL–AXIS WIND–TURBINE (HAWT) BLADES AND HAWT DRIVETRAIN GEARS

A Thesis
Presented to
the Graduate School of
Clemson University

In Partial Fulfillment
of the Requirements for the Degree
Master of Science
Mechanical Engineering

---

by
Varun Chenna
August 2014

Accepted by:
Dr. Mica Grujicic, Committee Chair
Dr. Chenning Tong
Dr. Jay Ochterbeck

ABSTRACT

Wind energy is one of the most promising and the fastest growing installed alternative-energy production technologies. In fact, it is anticipated that by 2030, at least 20% of the U.S. energy needs will be met by various onshore and offshore wind-farms [a collection of wind-turbines (converters of wind energy into electrical energy) at the same location]. A majority of wind turbines nowadays fall into the class of the so-called Horizontal Axis Wind Turbines (HAWTs).

Turbine blades and the gearbox are perhaps the most critical components/subsystems in the present designs of HAWTs. The combination of high failure rates (particularly those associated with turbine-blades and gear-boxes), long downtimes and the high cost of repair remains one of the major problems to the wind-energy industry today.

In the case of HAWT blades, one is typically concerned about the following two quasi-static structural-performance requirements: (a) sufficient "*flap-wise*" bending strength to withstand highly-rare extreme static-loading conditions (e.g., 50-year return-period gust, a short strong blast of wind); and (b) sufficient turbine blade "*flap-wise*" bending stiffness in order to ensure that a minimal clearance is maintained between blade tip and the turbine tower at all times during wind turbine operation. If these two structural requirements are not met, HAWT blades typically fail prematurely. In addition to the aforementioned quasi-static structural-performance requirements, one is also concerned about the premature-failure caused by inadequate fatigue-based durability of the HAWT blades. The durability requirement for the turbine blades is typically defined as a minimum of 20-year fatigue life (which corresponds roughly to ca. 10^8 cycles) when subjected to stochastic wind-loading conditions and cyclic gravity-induced edge-wise bending loads in the presence of thermally-fluctuating and environmentally challenging

conditions. In the present work, a computational framework has been developed to address: (a) structural response of HAWT blades subjected to extreme loading conditions; (b) high-cycle-fatigue-controlled durability of the HAWT blades; and (c) methodology for HAWT-blade material selection. To validate the computational approach used, key results are compared with their experimental counterparts available in the public-domain literature.

As far as the HAWT gear-boxes are concerned, while they are designed for the entire life (ca. 20 years) of the HAWT, in practice, most gear-boxes have to be repaired or even overhauled considerably earlier (3–5 years). Typically, a HAWT gear-box fails either due to the bending-fatigue-induced failure of its gears, or by tribo-chemical degradation and failure of its bearings. In the present work, a computational framework has been developed to predict HAWT service-life under extreme loading and unfavorable kinematic conditions, for the case when the gear-box service-life is controlled by gear-tooth bending-fatigue failure. In addition, a preliminary investigation of gear-box bearing kinematics, which can result in undesirable rolling-element skidding conditions, is conducted.

Keywords: Horizontal Axis Wind Turbine, Composite Material Selection, Fatigue Life Assessment, Gearbox Reliability

DEDICATION

This thesis would have been impossible without the unwavering love and support from my father, Mr. Keshava Chand Chenna, my mother, Mrs. Uma Rani Chenna, and my sister Yeshashwini Chenna to whom this thesis is dedicated.

ACKNOWLEDGEMENTS

I wish to express my sincere gratitude to my advisor, Professor Mica Grujicic, for his continuous encouragement, supervision, useful suggestions, and support throughout this research endeavor. His extensive knowledge and timely suggestions have been helpful in providing elegant solutions to the problems encountered throughout this research project.

My sincere thanks is also due to my advisory committee members Professor Chenning Tong, and Professor Jay Ochterbeck for their valuable suggestions during the course of this research project. Other faculty members of the department of Mechanical Engineering at Clemson University and the administrative staff are also greatly acknowledged for their support.

This acknowledgement will not be complete without the mention of my friends and colleagues at Clemson University whose valuable support and insightful discussions have helped mold this research into its existing form. Finally, I would like to thank my family and friends for their continuous support and encouragement during the whole tenure of my research.

TABLE OF CONTENTS

Page

TITLE PAGE I

ABSTRACT II

DEDICATION IV

ACKNOWLEDGEMENTS V

LIST OF TABLES X

LIST OF FIGURES XI

CHAPTER

CHAPTER 1: INTRODUCTION AND BACKGROUND, AND THESIS OUTLINE 1

1.1. Introduction and Background 1

1.2 Thesis Outline 6

1.3 References 7

CHAPTER 2: HORIZONTAL–AXIS WIND–TURBINE BLADES: STRUCTURAL–RESPONSE ANALYSIS, FATIGUE–LIFE PREDICTION, AND MATERIAL SELECTION 8

2.1. Abstract 8

2.2. Introduction 9

2.2.1 Wind Energy 10

2.2.2 Structural/Dynamics Requirements for HAWTs and HAWT Blades 12

2.2.3 Typical Construction of HAWTs and HAWT Blades 14

Table of Contents (Continued)

Page

2.2.4 Main Objectives 18

2.2.5 Chapter Organization 19

2.3. Computational Methods and Tools 20

2.3.1 Geometrical and Meshed Models 20

2.3.2 Wind-Turbine Blade Structural Analysis 24

2.3.3 Wind-Turbine Blade Fatigue-Life Prediction 29

2.3.4 Wind-Turbine Blade Material Selection 37

2.4. Results and Discussion 40

2.4.1 The Baseline Case 42

2.4.2 HAWT-Blade Design Modifications 57

2.4.3 HAWT-Blade Material Selection 59

2.5. Summary and Conclusions 65

2.6. References 66

CHAPTER 3: HORIZONTAL–AXIS WIND–TURBINE: GEAR–BOX FAILURE VIA TOOTH–BENDING FATIGUE 67

3.1. Abstract 67

3.2. Introduction 68

3.2.1 Wind Energy Harvesting 69

3.2.2 Wind Turbine Gearbox Reliability 71

3.2.3 Main Modes of Gear Damage and Failure 74

3.2.4 Main Objectives 76

Table of Contents (Continued)

Page

3.2.5 Chapter Organization 78

3.3. Finite-Element Stress Analysis 79

3.3.1 Problem Formulation 80

3.3.2 Computational Analysis 81

3.4. Fatigue Strength and Life-Cycle Prediction 86

3.4.1 Fatigue-Crack Initiation 87

3.4.2 Fatigue-Crack Growth 89

3.5. Results and Discussion 91

3.5.1 Temporal Evolution/Spatial Distribution of Gear-Tooth Stresses 92

3.5.2 Fatigue-Life Prediction 102

3.6. Summary and Conclusions 106

3.7. References 107

CHAPTER 4: HORIZONTAL–AXIS WIND–TURBINE: PRELIMINARY BEARING KINEMATICS AND KINETICS 109

4.1. Abstract 109

4.2. Introduction 110

4.2.1 Wind Energy Harvesting 111

4.2.2 Wind Turbine Gear-box Reliability 113

4.2.3 Premature Failure of Wind-Turbine Gear-box Roller-Bearings 116

4.2.4 Main Objectives 119

4.3. Multibody Dynamics of a Gearbox Roller Bearing 120

Table of Contents (Continued)

Page

4.3.1 Problem Description 120

4.3.2 SIMPACK Computer Program 122

4.3.3 Roller-Bearing MBD Model 123

4.3.4 Construction of the User-defined Force Element 139

4.3.5 Kinematics-based Derivation of the Zero-Slip Roller Angular Velocity 140

4.4. Results and Discussion 142

4.5. Summary and Conclusions 147

4.6. References 148

CHAPTER 5: CONCLUSIONS AND SUGGESTIONS FOR FUTURE WORK 149

5.1. Conclusions 149

5.2. Suggestions for Future Work 151

APPENDIX A: User-defined Force Element – uforce20 source code 152

LIST OF TABLES

Table Page

Table 2-1 HAWT-Blade Composite-laminate Lay-up Sequence 45

Table 2-2 Summary of the HAWT-Blade Material Properties 46

Table 4-1 Specifications of multi-body model of cylindrical roller bearing.....126

Table 4-2 Types of joints used in the MBS model.....127

Table 4-3 Relationship between the dimensionless contact parameters [11].....130

LIST OF FIGURES

Figure Page

Figure 1-1 A photograph of a typical off-shore wind farm, with the major wind turbine sub-systems identified [8] 2

Figure 2-1 Variation of the horizontal-axis wind turbine power output and rotor diameter with the year of deployment. 11

Figure 2-2 Typical off-shore wind farm. The major wind turbine sub-systems are identified [16]. 15

Figure 2-3 Typical turbine-blade cross-sectional area in the case of: (a) the one-piece construction; and (b) the two-piece construction. 17

Figure 2-4 Typical: (a) geometrical and (b) meshed models of a single wind-turbine blade analyzed in the present work. 22

Figure 2-5 An example of the results pertaining to the 2-dimensional distribution of the coefficient of pressure and the streamlines in the region surrounding the airfoil for the case of a 10^0 angle of attack (the angle between the wind direction and the airfoil chord. 26

Figure 2-6 (a) Application of the rainflow cycle-counting algorithm to a simple load signal after the peak/valley reconstruction. Please see text for explanation; and (b) the resulting three dimensional histogram showing the number of cycles / half-cycles in each mean stress/strain – stress/strain amplitude bin. 31

List of Figures (Continued)

Figure Page

Figure 2-7 An example of the Goodman diagram showing constant fatigue-life data (dashed lines) and constant R-ratio data (the solid lines emanating from the origin).....33

Figure 2-8 An example of the three-dimensional histogram showing the effect of stress/strain amplitude and the stress/strain mean-value of the material fatigue life. 35

Figure 2-9 Baseline case of the HAWT blade analyzed in the present work: (a) the airfoil cross section; and (b) the planform. 43

Figure 2-10 Displacement magnitude distribution over the HAWT blade outer skin caused by a 70m/s gust: (a) the baseline case; and (b) a modified-design case. 48

Figure 2-11 Variation of the gust-induced HAWT-blade thickness for the blade designs analyzed in the present work. 50

Figure 2-12 Von Mises equivalent stress distribution over the HAWT interior structural members (spar-cap and shear-webs) caused by a 70m/s gust: (a) the baseline case; and (b) a modified-design case. 52

Figure 2-13 Variation of the gust-induced HAWT-blade twist angle for the blade designs analyzed in the present work. 54

Figure 2-14 Material property charts used in the HAWT-blade material selection process. Please see text for details. 62

List of Figures (Continued)

Figure Page

Figure 3-1 Schematic of a prototypical wind-turbine gearbox. The major components and sub-systems are identified. 73

Figure 3-2 (a) Geometrical model; and (b) Close-up of the meshed model consisting of two helical gears and two shafts, used in the present work....82

Figure 3-3 Typical temporal evolution and spatial distribution of the maximum principal stress over the surface of a tooth of the driven gear (for the case of perfectly aligned shafts). 93

Figure 3-4 The effect of the torque transferred by the gear-pair analyzed on the largest value of the maximum principal stress in the subject gear-tooth)....96

Figure 3-5 The effect of shaft misalignment (as quantified by the corresponding misalignment angle, α), at a constant level of the transferred-torque, on the spatial distribution and the magnitude of the gear-tooth maximum principal stress, at the instant when the subject gear-tooth experiences the largest value of the maximum principal stress: (a) $\alpha = 0°$; (b) $\alpha = 1°$; (c) $\alpha = 2°$; and (d) $\alpha = 3°$. 98

Figure 3-6 The effect of the gear-misalignment angle, at a constant level of the transferred-torque, on the largest values of the maximum principal stress.....101

Figure 3-7 The effect of the transferred-torque on the total service-life of the driven helical gear, for the case of perfectly aligned gears. 104

List of Figures (Continued)

Figure Page

Figure 3-8 The effect of the misalignment angle on the total fatigue-controlled service-life of the driven helical gear, under a constant transferred-torque condition. 105

Figure 4-1 Schematic of a prototypical wind-turbine gear-box. The major components and sub-systems are identified. Failure typically occurs within the (planet, intermediate-speed shaft and high-speed shaft) roller-bearings.....115

Figure 4-2 A labeled CAD model of the roller bearing MBD model analyzed. 125

Figure 4-3 The effect of rolling-element/race slip velocity on the coefficient of friction under elastohydrodynamic conditions [10].....132

Figure 4-4 A schematic of the single-roller/inner-race contact pair used to explain the way the contact-interaction torque is calculated within uforce20 and returned to SIMPACK.....136

Figure 4-5 The effect of the inner-race rotational speed and the outer-race rotational speed on the no-slip revolving velocity of the rollers in the case of the roller-bearing being analyzed: (a) an analytical kinematics-based solution; and (b) the numerical uforce20/SIMPACK based solution.....143

Figure 4-6 The effect of the inner-race rotational speed and the outer-race rotational speed on the no-slip angular (rotational) velocity of the rollers in the case of the roller-bearing being analyzed: (a) an analytical kinematics-based solution; and (b) the numerical uforce20/SIMPACK based solution. 144

Figure Page

Figure 4-7 The effect of (constant) inner-race rotational velocity, for the case of the initially stationary rolling elements and always stationary outer race, at the interfaces between the rolling elements and: (a) the inner race; (b) the outer race. 146

CHAPTER 1: INTRODUCTION AND BACKGROUND, AND THESIS OUTLINE

1.1. Introduction and Background

Wind energy is one of the most promising and the fastest growing installed alternative-energy production technologies. In fact, it is anticipated that by 2030, at least 20% of the U.S. energy needs will be met by various onshore and offshore wind-farms [a collection of wind-turbines (converters of wind energy into electrical energy) at the same location] [1]. A majority of wind turbines nowadays fall into the class of the so-called Horizontal Axis Wind Turbines (HAWTs). Typically, a HAWT consists of the following key functional components/assemblies: (a) rotor – consisting of three (for increased structural stability and aerodynamic efficiency) aerodynamically-shaped blades; (b) drive-train – consisting of an input/low-speed shaft, a gear-box and output/high-speed shaft; (c) electrical generator – the rotor of which is attached to the high-speed shaft; (d) nacelle – the housing of the drive-train and electrical generator; (e) bedplate – to which the drive-train, electrical generator and nacelle are mounted; and (f) tower – a tall, slender structure on the top of which the bedplate is mounted. A photograph of an offshore wind turbine is provided in Figure 1-1. All major components of the turbine are labeled for identification.

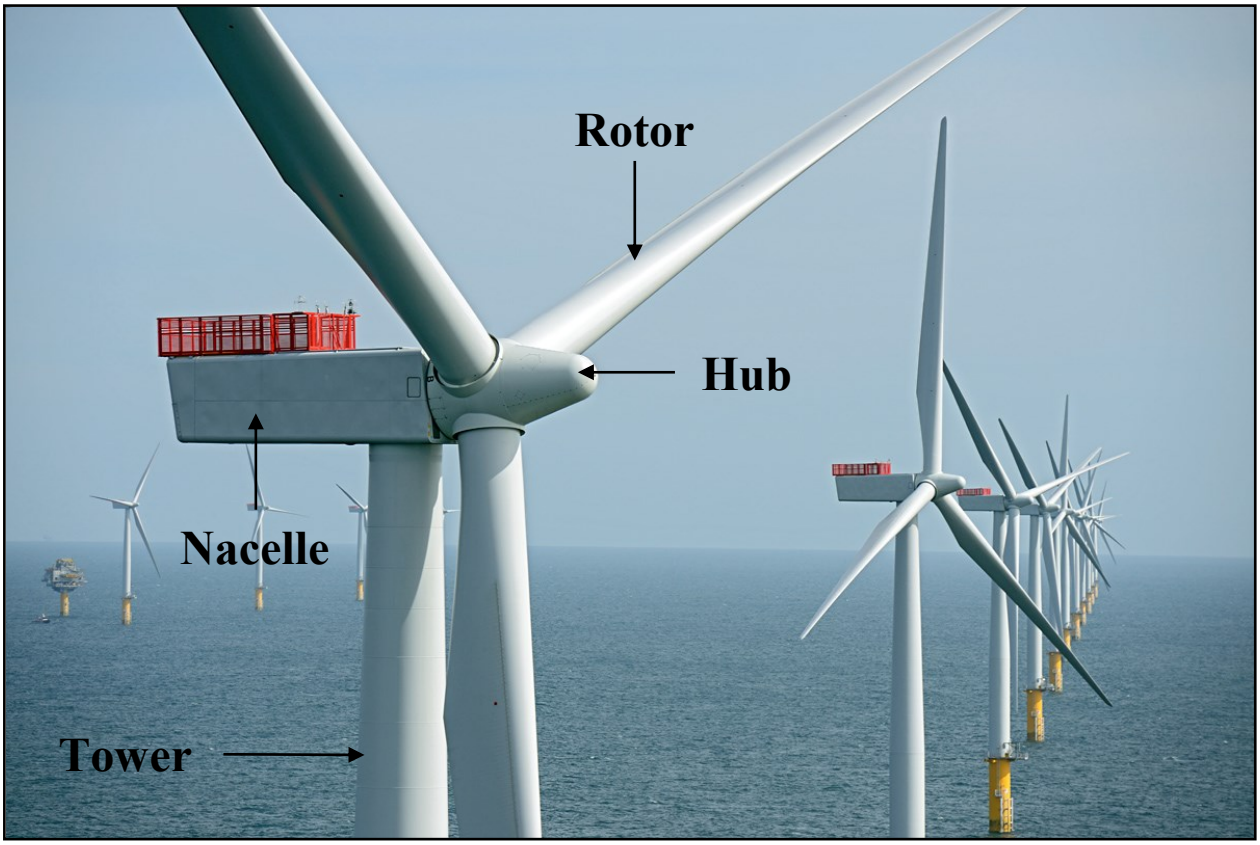

Figure 1-1 A photograph of a typical off-shore wind farm, with the major wind turbine sub-systems identified [8]

To reduce the energy production cost, commercial wind turbines have grown considerably in size over the last 30 years. The large wind-turbine economics is based on the fact that as the hub-height/wind-turbine rotor radius increases, the average wind-speed/wind-energy captured increases due to the so called wind shear effect (a natural increase in the wind speed with elevation with respect to the terrain). Consequently, for the same energy production level, fewer wind-turbine units are required, which in turn leads to a reduction in the cost of operation of the farm. As the size of the wind-turbine rotor increases, the structural performance, durability and dynamic-stability requirements tend to become more and more challenging to meet [2, 3].

Turbine blades and the gearbox are perhaps the most critical components/subsystems in the present designs of wind turbines. The combination of high failure rates (particularly those associated with turbine-blades and gear-boxes), long downtimes and the high cost of repair remains one of the major problems to the wind-energy industry [4–6]. In the earlier HAWT designs, these problems could be linked to the following root causes: (a) fundamental design errors; (b) manufacturing deficiencies; and (c) under-estimation of the operating loads. It is believed that these root causes have mainly been eliminated nowadays, through the development and application of wind-turbine blade and gear-box design standards and the establishment of good manufacturing practices [7]. Nevertheless, premature-failure of wind-turbine blades and gear-boxes remains an unresolved problem.

In the case of HAWT blades, one is typically concerned about the following two quasi-static structural-performance requirements: (a) sufficient "*flap-wise*" bending strength to withstand highly-rare extreme static-loading conditions (e.g., 50-year return-period gust, a short strong blast of wind). Flap-wise bending is blade bending in a direction normal to the rotor plane of rotation caused by the wind acting mainly over the broad faces of the blade; and (b) sufficient

turbine blade "*flap-wise*" bending stiffness in order to ensure that a minimal clearance is maintained between blade tip and the turbine tower at all times during wind turbine operation. If these two structural requirements are not met, HAWT blades typically fail prematurely.

In addition to the aforementioned quasi-static structural-performance requirements, one is also concerned about the premature-failure caused by inadequate fatigue-based durability of the HAWT blades. The durability requirement for the turbine blades is typically defined as a minimum of 20-year fatigue life (which corresponds roughly to ca. 10^8 cycles) when subjected to stochastic wind-loading conditions and cyclic gravity-induced edge-wise bending loads in the presence of thermally-fluctuating and environmentally challenging conditions. Edge-wise bending is blade bending in a direction parallel to the rotor plane of rotation.

As far as the HAWT gear-boxes are concerned, while they are designed for the entire life (ca. 20 years) of the HAWT, in practice, most gear-boxes have to be repaired or even overhauled considerably earlier (3–5 years) [5, 6]. Typically, HAWT gear-boxes fail either due to the bending-fatigue-induced failure of its gears [5, 6], or by tribo-chemical degradation and failure of its bearings.

The persistence of premature-failure of HAWT blades and gear-boxes has negatively affected wind-energy economics through increases in both the sales price of wind-turbines and the cost of ownership/operation of the wind-turbines. The combination of these high failure rates and the high cost of turbine blades and gearboxes have contributed to: (a) increased cost of wind energy; (b) increased sales price of wind-turbines due to higher warranty premiums; and (c) a higher cost of ownership due to the need for funds to cover repair after warranty expiration. Clearly, to make wind energy a more viable renewable-energy alternative, its cost must be

brought back to a decreasing trend, which entails a significant increase in the long-term reliability of turbine blades and gear-boxes.

1.2 Thesis Outline

Within the present work, three aspects of HAWTs and their failure are addressed: (a) excessive-loading and fatigue-induced failure of HAWT blades; (b) gear-tooth bending-fatigue-induced failure of HAWT gear-boxes; and (c) modeling of the unfavorable kinematics (specifically, roller skidding during transient events) of a prototypical gear-box roller bearing. Such unfavorable kinematics is believed to be one of the root causes for gear-box roller-bearing premature failure. These three aspects of the present work are discussed in detail in Chapters 2, 3 and 4, respectively. A summary of the main findings obtained and of the main conclusions reached in the present work is given in Chapter 5. Also, in Chapter 5, a list of suggestions for future work is provided.

1.3 References

1. US Department of Energy, "***20% Wind Energy by 2030, Increasing Wind Energy's Contribution to U.S. Electricity Supply***," http://www.nrel.gov/docs/fy08osti/41869.pdf, accessed March 4, 2014.

2. M. Grujicic, G. Arakere, V. Sellappan, A. Vallejo and M. Ozen, "***Structural-response Analysis, Fatigue-life Prediction and Material Selection for 1MW Horizontal-axis Wind-Turbine Blades***," Journal of Materials Engineering and Performance, 19: 780–801, 2010.

3. M. Grujicic, G. Arakere, B. Pandurangan, V. Sellappan, A. Vallejo and M. Ozen, "***Multidisciplinary Optimization for Fiber-Glass Reinforced Epoxy-Matrix Composite 5MW Horizontal-axis Wind-turbine Blades***," Journal of Materials Engineering and Performance, 19: 1116–1127, 2010.

4. B. McNiff, W.D. Musial, and R. Errichello, "***Variations in Gear Fatigue Life for Different Wind Turbine Braking Strategies***," Solar Energy Research Institute, Golden, Colorado USA, 1990.

5. M. Grujicic, R. Galgalikar, J. S. Snipes, S. Ramaswami, V. Chenna and R. Yavari, "***Finite-Element Analysis of Horizontal-axis Wind-turbine Gearbox Failure via Tooth-bending Fatigue***," International Journal of Material and Mechanical Engineering, 3, 6–15, 2014. DOI: 10.14355/ijmme.2014.0301.02

6. M. Grujicic, S. Ramaswami, J. S. Snipes, R. Galgalikar, V. Chenna and R. Yavari, "***Computer-Aided Engineering Analysis of Tooth-bending Fatigue-based Failure in Horizontal-Axis Wind-Turbine Gearboxes***," International Journal of Structural Integrity, 5, 60–82, 2014. DOI: 10.1108/IJSI-08-2013-0017

7. International Organization for Standardization, ISO/IEC 61400-4:2012, "***Wind Turbines – Part 4: Standard for Design and Specification of Gear-boxes***," ISO Geneva, Switzerland, 2012.

8. http://www.tu.no/petroleum/2012/10/15/intern-strid-i-statoil-om-vindkraft, accessed May 6, 2014

CHAPTER 2: HORIZONTAL–AXIS WIND–TURBINE BLADES: STRUCTURAL–RESPONSE ANALYSIS, FATIGUE–LIFE PREDICTION, AND MATERIAL SELECTION

2.1. Abstract

The problem of mechanical design, performance prediction (e.g. "*flap-wise*"/"*edge-wise*" bending stiffness, fatigue-controlled life, the extent of bending-to-torsion coupling), and material selection for a prototypical 1MW Horizontal Axis Wind Turbine (HAWT) blade is investigated using various computer aided engineering tools. For example, a computer program was developed which can automatically generate both a geometrical model and a full finite-element input deck for a given single HAWT blade with a given airfoil shape, size and the type and position of the interior load-bearing longitudinal beam/shear-webs. In addition, composite-material laminate lay-up can be specified and varied in order to obtain a best combination of the blade aerodynamic efficiency and longevity. A simple procedure for HAWT blade material selection is also developed which attempts to identify the optimal material candidates for a given set of functional requirements, longevity and low weight.

2.2. Introduction

In order to meet the world's ever-increasing energy needs in the presence of continuously depleting fossil-fuel reserves and stricter environmental regulations, various alternative/renewable energy sources are currently being investigated/assessed. Among the various renewable energy sources, wind energy plays a significant role and it is currently the fastest growing installed alternative-energy production technology. In fact, it is anticipated that by 2030, at least 20% of the U.S. energy needs will be met by various onshore and offshore wind-farms [1]. The wind-energy technology is commonly credited with the following two main advantages: (a) there are no raw-material availability limitations; and (b) relative ease and cost-effectiveness of the integration of wind-farms to the existing power grid.

2.2.1 Wind Energy

Due to mainly economic reasons (i.e. in order to reduce the electrical energy production cost, typically expressed in $/kW.hr), commercial wind turbines have grown considerably in size over the last 30 years, Figure 2-1. Simply stated, wind speed and, hence, wind-power captured, increases with altitude and this reduces the number of individual turbine units on a wind farm and in turn the cost of operation of the farm. As depicted in Figure 2-1, the largest wind turbine unit currently in service is rated at 5MW and has a rotor diameter of 124m. As the size of the wind turbines rotor is increasing, the structural and dynamics requirements tend to become more and more challenging to meet and it is not clear, what is the ultimate rotor diameter which can be attained with the present material/manufacturing technologies.

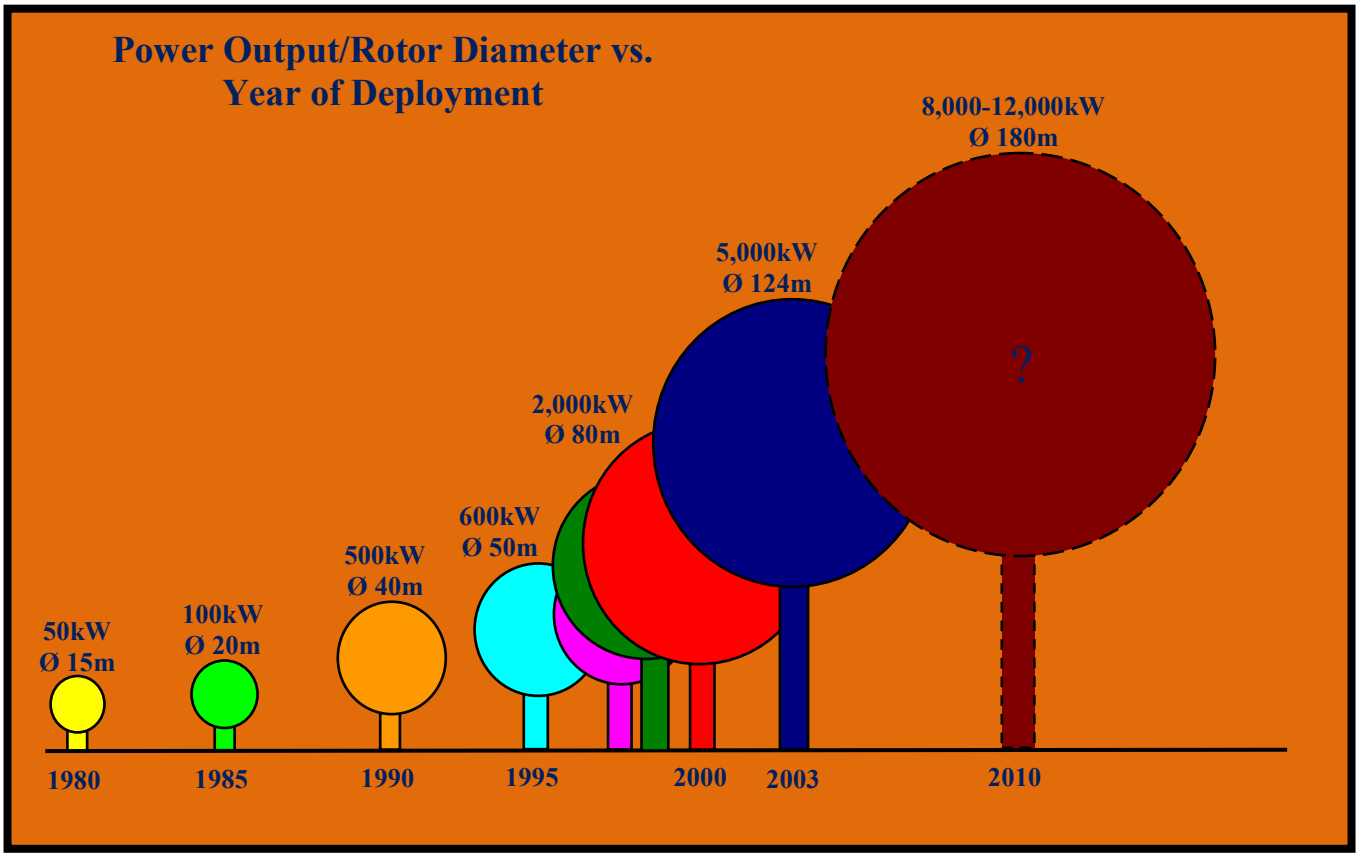

Figure 2-1 Variation of the horizontal-axis wind turbine power output and rotor diameter with the year of deployment.

2.2.2 Structural/Dynamics Requirements for HAWTs and HAWT Blades

Among the main structural/dynamics requirements for wind-turbines are: (a) sufficient strength to withstand highly-rare extreme static-loading conditions (e.g. 50-year return-period gust, a short blast of wind); (b) sufficient turbine blade "*flap-wise*" bending stiffness in order to maintain, at all times, the required minimal clearance between the blade tip and the turbine tower; (c) at least a 20-year fatigue life (corresponds roughly to ca. 10^8 cycles) when subjected to stochastic wind-loading conditions in the presence of thermally-fluctuating and environmentally challenging conditions; and (d) various structural/dynamics requirements related to a high mass of the wind-turbine blades (ca. 18 tons in the case of the 62m long blade). That is not only the blade-root and the turbine-hub to which the blades are attached need to sustain the centrifugal and hoop forces accompanying the turning of the rotor, but also the nacelle (i.e. the structure that houses all of the gear boxes and the drive train connecting the hub to the power generator), the tower and the foundations must be able to withstand the whole wind-turbine dynamics. For a more comprehensive overview of the wind-turbine design requirements, the reader is referred to the work of Burton et al. [2].

Development and construction of highly-reliable large rotor-diameter wind turbines is a major challenge since wind turbines are large, flexible, articulated structures subjected to stochastic transient aerodynamic loading conditions. It is, hence, not surprising that several wind-turbine manufacturers face serious problems in meeting the structural-dynamics and fatigue-life turbine-system requirements. The inability to meet the aforementioned requirements is often caused by failure of the transmission gear pinions, failure of bearings, blade fracture, tower buckling, etc. When these problems persist, insurance companies become reluctant in providing their services to the wind-turbine manufacturers causing production shut-down and often

company bankruptcy. In order to help prevent these dire consequences, more and more wind-turbine manufacturers are resorting to the use of advanced computer-aided engineering tools, during design, development, verification and fabrication of their products.

2.2.3 Typical Construction of HAWTs and HAWT Blades

Wind turbine is essentially a converter of wind energy into electrical energy. This energy conversion is based on the principle of having the wind drive a rotor, thereby transferring a power of

$$P = \alpha\beta\rho A v^3 \qquad (2\text{–}1)$$

to the electrical generator, where α is an aerodynamic efficiency parameter, β is a drive-train efficiency parameter; ρ is air density, A rotor surface area and v the wind speed. The P/A ratio is commonly referred to as the specific-power rating. To attain rotor rotation and a high value of α, the rotor has to be constructed as a set of three (sometime two) aerodynamically shaped blades. The blades are (typically) attached to a horizontal hub (which is connected to the rotor of the electrical generator, via a gearbox/drive–train system, housed within the nacelle). The rotor/hub/nacelle assembly is placed on a tower and the resulting wind energy converter is referred to as the Horizontal Axis Wind Turbine (HAWT). A photograph of an offshore wind turbine is provided in Figure 2-2. All major components of the turbine are labeled for identification.

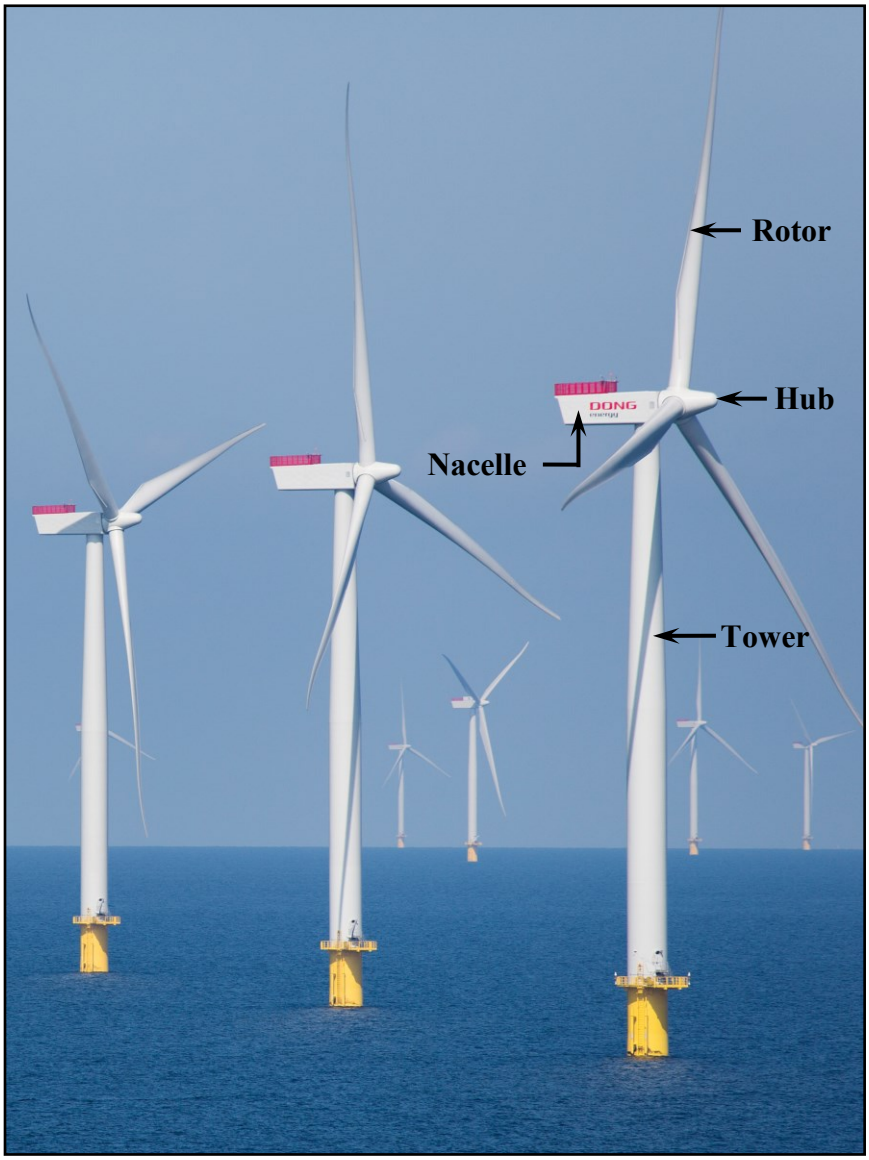

Figure 2-2 Typical off-shore wind farm. The major wind turbine sub-systems are identified [16].

Turbine blades are perhaps the most critical components in the present designs of wind turbines. There are two major designs of the wind turbine blades: (a) the so-called "one-piece" construction, Figure 2-3(a) and (b) the so-called "two–piece" construction, Figure 2-3(b). In both cases, the aerodynamic shape of the blade is obtained through the use of separately-fabricated and adhesively-joined outer-shells (often referred to as the outer skin or the upper and lower cambers). The two constructions differ with respect to the design and joining of their load-bearing interior structure (running down the blade length). In the case of the one-piece construction, the supporting structure consists of a single close box spar which is adhesively joined to the lower and upper outer shells. Since the stresses being transferred between the outer shells and the spar are lower in magnitude, a lower-strength adhesive like polyurethane is typically used. In the case of the two-piece construction, the supporting structure consists of two stiffeners/shear-webs which are also adhesively joined with the outer shells. However, since the adhesive joints have to transfer the stresses between the two stiffeners in addition to transferring stresses between the outer shells and the shear webs, higher-strength adhesives like epoxy have to be used.

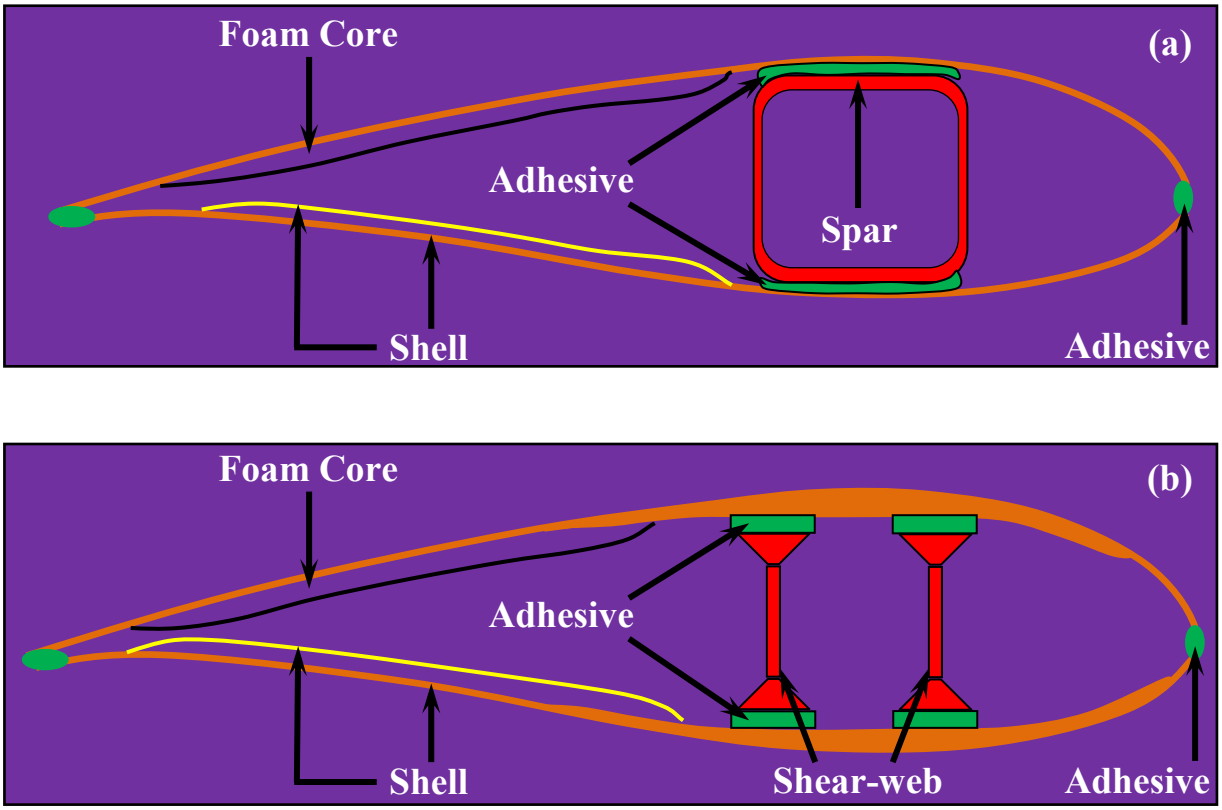

Figure 2-3 Typical turbine-blade cross-sectional area in the case of: (a) the one-piece construction; and (b) the two-piece construction.

2.2.4 Main Objectives

The main objective of the present work is to help further advance the use of computer aided engineering methods and tools (e.g. geometrical modeling, structural analysis including fatigue-controlled life-cycle prediction and material selection methodologies) to the field of design and development of HAWT blades. Consequently, many critical decisions regarding the design and fabrication of these components can be made in the earlier stages of the overall design cycle. This strategy has been proved to yield very attractive economic benefits in the case of more mature industries such as the automotive and the aerospace industries.

Specific issues addressed in the present work include the problem of automated generation of a geometrical model and a full finite-element input deck, coupled with realistic wind-induced loading conditions for a given set of HAWT blade geometrical, structural and material parameters. Also the use of a computer-aided material-selection methodology for identification of the optimal HAWT blade materials for a given set of functional, longevity and cost-efficiency requirements is considered.

2.2.5 Chapter Organization

The organization of the chapter is as follows. A brief overview of the approach used for automated HAWT-blade geometrical model and the full finite-element input deck generation is presented in Section 2.3.1. The quasi-static finite element procedure and a post-processing methodology used respectively to quantify the key blade structural-performance parameters and the blade fatigue life are described in Sections 2.3.2 and 2.3.3. A single HAWT-blade material selection procedure is presented in Section 2.3.4. The results are obtained and discussed in Section 2.4. A brief summary of the work carried out and the results obtained is presented in Section 2.5.

2.3. Computational Methods and Tools

2.3.1 Geometrical and Meshed Models

As mentioned earlier, the subject of the present investigation is a structural-response analysis, durability assessment/prediction and material selection for a single prototypical 1MW HAWT-Blade. The wind-turbine blade is essentially a cantilever beam mounted on a rotating hub. The aerodynamic shape of the blade is formed by relatively-thin outer shells. The loads acting on the blade are mainly supported by a longitudinal box-shaped spar or by a pair of the C-shaped shear webs. To reduce the bending moments in blade section away from the blade root (the section where the blade is attached to the hub), wind-turbine blades are generally tapered. Tapering typically includes not only the blade cross section but also the shell/beam/web thickness. This ensures that different blade sections experience comparable extreme loading (e.g. the maximum strain). In addition to the taper, turbine blade generally possess a certain amount of twist along their length. Twist is beneficial with respect to self-starting of the rotor and through the bending/torsion coupling effects; helps improve wind-power capture efficiency.

To create a prototypical wind-turbine blade, a computer program was first developed which can generate one of the standard airfoil profiles such as the *Wortmann FX84W*, the *Althaus AH93W* or the *NACA-23012* (e.g., [3]) of the given dimensions. The program is implemented in MATLAB, a general-purpose mathematical package [4]. Next, the program further enables the creation of the entire wind-turbine blade geometrical model (in the .stl format) and a finite-element mesh model (for a given set of parameters related to the taper, twist, shear-web lateral positions, mesh-topology, etc.).

An example of the wind-turbine blade geometrical model and of the corresponding finite-element meshed model, are displayed respectively in Figure 2-4(a)-(b). The case of a prototypical

1MW wind-turbine with a 0.44kW/m^2 specific power rating (a ratio of the power rating to the rotor swept area) was considered in the present work. Following the HAWT-blade design procedure outlined in Ref. [12], a series of HAWT-blades with the following general dimensions and geometrical parameters was constructed and analyzed: length = 30m, blade diameter at the root = 1.5m, chord length at the first airfoil station located at 25% from the root = 2.1m, chord length at the blade tip = 0.67m (with a linear taper in-between), S818 airfoil shape and a total twist angle = 10.5^o. Also, typically, the two outer skins and the two webs are meshed using ca. 4,160 and ca. 512 first-order four-node composite-shell elements, respectively, while the two thick layers of adhesives which connect the webs to the outer shells, were meshed using ca. 1,088 first-order eight-node hexahedral solid elements. To facilitate optimization of the HAWT-blade composite-laminate lay-up, all the meshes used were of a structured character.

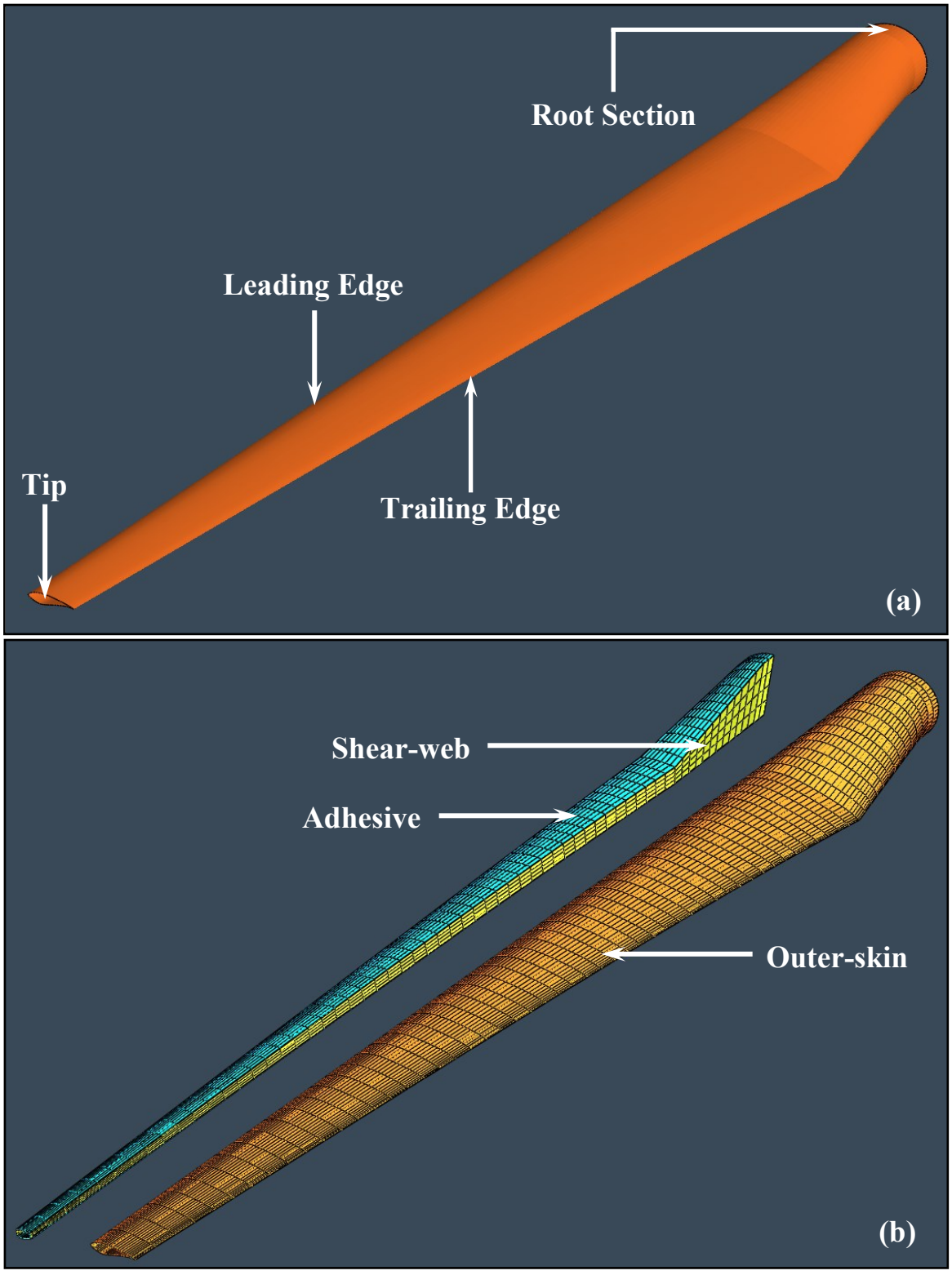

Figure 2-4 Typical: (a) geometrical and (b) meshed models of a single wind-turbine blade analyzed in the present work.

The geometry/mesh generator program described above enabled an automated generation of the entire finite-element input deck for a selected set of parameters which is a critical requirement for computer–efficient design-of-experiments and design-optimization analyses. For example, lateral/transverse locations of the two shear webs and the thicknesses of two spar-caps (horizontal beam-sections bridging the shear webs) and two adhesive layers could be readily varied.

2.3.2 Wind-Turbine Blade Structural Analysis

Wind-turbine blades are generally oriented in such a way that their wide faces are roughly parallel with the hub-rotation axis and, in the case of the so-called "*up-wind design*," with their leading edge facing the wind. In other words, the effective wind direction as experienced by the blades is in the rotational plane of the rotor although the real-wind direction is orthogonal to it. Furthermore, due to the aerodynamic shape of the blades, significant lift-induced torque is produced causing the rotor to spin.

Lift-type wind-based loads, as described above not only cause rotor to spin but also lead to the so-called "*flap-wise*" bending of the blades. It should be recognized that the lift-induced loading has both a persistent/static-like and a time-varying component (the latter one is due to natural variability of the wind). In addition, the relative fraction of the two load components changes during rotation of the rotor due to the so-called "*wind-shear*" effects (i.e. due to a natural increase in the wind speed with an increase in the height above the terrain).

In addition to the lift-related loads discussed above, wind-turbine blades are also subjected to gravity loads. These loads are the highest in magnitude when the blade is in a nearly horizontal position and they cause "*edge-wise*" bending of the wind-turbine blade. Since, the blades bend one way when they are on the right-hand side of the tower while they bend in the other direction when they are on the left-hand side of the tower; gravity loading also contains a variable component.

Wind turbine blades are also subjected to centrifugal loading due to rotation of the rotor. Nevertheless, since the upper-bound angular velocity of the rotor is typically in a 10-20rpm range, centrifugal-tensile loads along the blade length are generally not considered as design-controlling/life-limiting loads (and are, hence, ignored in the present work).

To account for the typical wind-turbine blade loading discussed above, a series of two-dimensional aerodynamic analyses was carried out using the *Javafoil* computer program [5]. This program solves the flow equations over an airfoil by implementing the boundary integral method. For the given airfoil profile and size, the wind speed and the angle of attack, the program generates a distribution of pressures over the blade surface. An example of the results pertaining to the spatial distribution of the coefficient of pressure (a ratio of the pressure minus mean-stream pressure difference and the half product of mean-stream air-density and squared wind velocity) is displayed in Figure 2-5. These analyses are repeated for up to 10 equally-spaced wind-turbine blade cross sections. The results obtained were then used within an interpolation algorithm to compute pressure distribution over the entire blade surface.

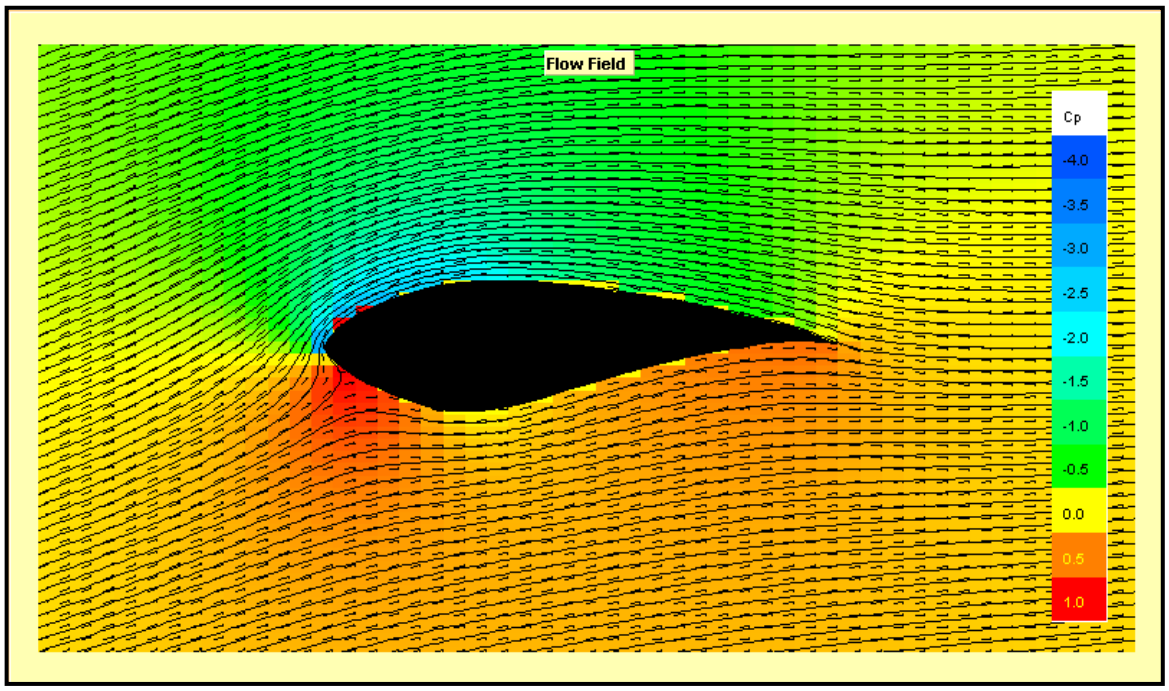

Figure 2-5 An example of the results pertaining to the 2-dimensional distribution of the coefficient of pressure and the streamlines in the region surrounding the airfoil for the case of a 10^0 angle of attack (the angle between the wind direction and the airfoil chord.

Two wind-induced loading conditions were considered:

(a) For the structural-response analysis, peak loads were derived by considering a 50-year extreme gust of 70 m/s (IEC Class 1 [13]). The blade is assumed to be in a fully feathered position (i.e. pitch of the blade is adjusted to obtain the wind attack-angle associated with the lowest aerodynamic loads) with a ±15° variation in wind direction. To attain the most conservative loading case, it was assumed that the gust-induced loading results in each blade section simultaneously reaching its local maximum-lift coefficient condition; and

(b) For the fatigue-life prediction/assessment analysis, loading was determined using the average wind speed at the wind-turbine power rating. This velocity was computed using the procedure outlined in Ref. [12]. Within this procedure, the specific power rating (taken to be $0.44 kW/m^2$) is defined as a product of rotor efficiency coefficient ($\alpha = 0.5$), a drive-train efficiency ($\beta = 0.925$), air density ($\rho = 1.225 kg/m^3$) and the third power of the wind rated speed (v = 130% of the wind mean speed at the rotor hub elevation). This procedure yielded a wind mean speed at the hub elevation of 7.67m/s in the direction of rotor axis. It should be also noted that this procedure enabled determination of the mean-level wind-induced loads in the HAWT-blade. To account for the time-varying component of the wind-induced and gravity loading, the so-called WISPER (Wind Spectrum Reference) loading history/profile [6] (a reference load spectrum typically used in the design of wind turbine blades in Europe) was used (after proper scaling).

To determine the quasi-static structural response of the blade, a static finite-element analysis was carried out in which the root-edge of the blade was fixed and the blade outer surfaces subjected to the aforementioned gust-induced loading. The results of these analyses were

used to determine the turbine-blade bending stiffness (as quantified by the average displacement of its tip section) and by the blade strength (as measured by the largest value of the von Mises equivalent stress within its interior) as well as the extent of bending-to-torsion coupling (as measured by the loading-induced twist at the blade tip). In addition due to the fact that wind-induced loading was found to be nearly proportional (i.e. the orientation of the in-plane principal coordinates system over the most highly stress blade-surface sections was found not to change significantly during loading), the results of the structural analysis were used also in the fatigue-life assessment analysis (discussed in next section). In other words, local stresses are assumed to scale linearly with the level of local wind-induced loading so that the gust-based stresses can be used to directly calculate the corresponding stresses at any level of wind-induced loading.

All the calculations pertaining to the structural response of the wind-turbine blade were done using ABAQUS/Standard, a commercially available general-purpose finite-element program [7].

2.3.3 Wind-Turbine Blade Fatigue-Life Prediction

It is well-established that in most cases the life cycle of a wind-turbine blade is controlled by its fatigue strength (in the presence of local thermal and aggressive environmental conditions). While it is generally fairly straight forward to quantify fatigue strength of the structural materials (glass- or carbon-fiber reinforced polymer-matrix composites, in the case of wind-turbine blades) under constant-amplitude loading conditions, relating the material fatigue strength to the component (a turbine blade, in the present case) is a quite challenging task. This is primarily due to the fact that time-varying loading (e.g. WISPER) is associated with non-constant amplitude. In other words, real time-varying wind-induced loading is irregular and stochastic and the associated load history affects the component fatigue life in complex ways. The procedure used in the present work to correlate the material fatigue strength with the component fatigue strength/life is based on the use of a cycle-counting algorithm (the so-called "Rainflow" cycle-counting analysis [8]), a linearized Goodman diagram [e.g. 9] to account for the effect of mean-stress/strain on the material fatigue life/strength and the Miner's linear-superposition principle/rule [10]. The Rainflow analysis, the Goodman diagram and the Miner's rule are briefly overviewed in the remainder of this section.

Rainflow Analysis

When a time-varying load signal is recorded over a sampling period, and needs to be described in terms of a three-dimensional histogram (each bin of which being characterized by a range of the signal amplitude and a range of the signal mean value), procedures like the rainflow counting algorithm are used. Within this procedure, the first step involves converting the original load signal into a sequence of load peaks and valleys. Then the cycle counting algorithm is

invoked. To help explain the rainflow cycle-counting algorithm, a simple load signal (after the peak/valley reconstruction) is depicted in Figure 2-6(a), with the time axis running downward.

Within the rainflow cycle-counting algorithm, separate counting of load half-cycles is carried out for the ones starting from the peaks and the ones starting from the valleys. In Figure 2-6(a), only the half-cycles originating from the peaks are analyzed. A half-cycle then starts from each peak and ends when one of the following three criteria is met:

(a) When the end of the signal is reached (Case A in Figure 2-6(a));

(b) When the half-cycle in question runs into a half-cycle which originated earlier and which is associated with a higher peak value(Case B in Figure 2-6(a)); and

(c) When the half-cycle in question runs into another half-cycle which originated at a later time and which is associated with a higher value of the peak (Case C in Figure 2-6(a)).

Once all the half-cycles are identified they are placed in bins, each bin being characterized by a range of the load amplitude and the load mean-value. An example of the resulting three-dimensional histogram showing the number of cycles/half-cycles present in the load signal associated with a given combination of the load amplitude and the load mean-value is depicted in Figure 2-6(b).

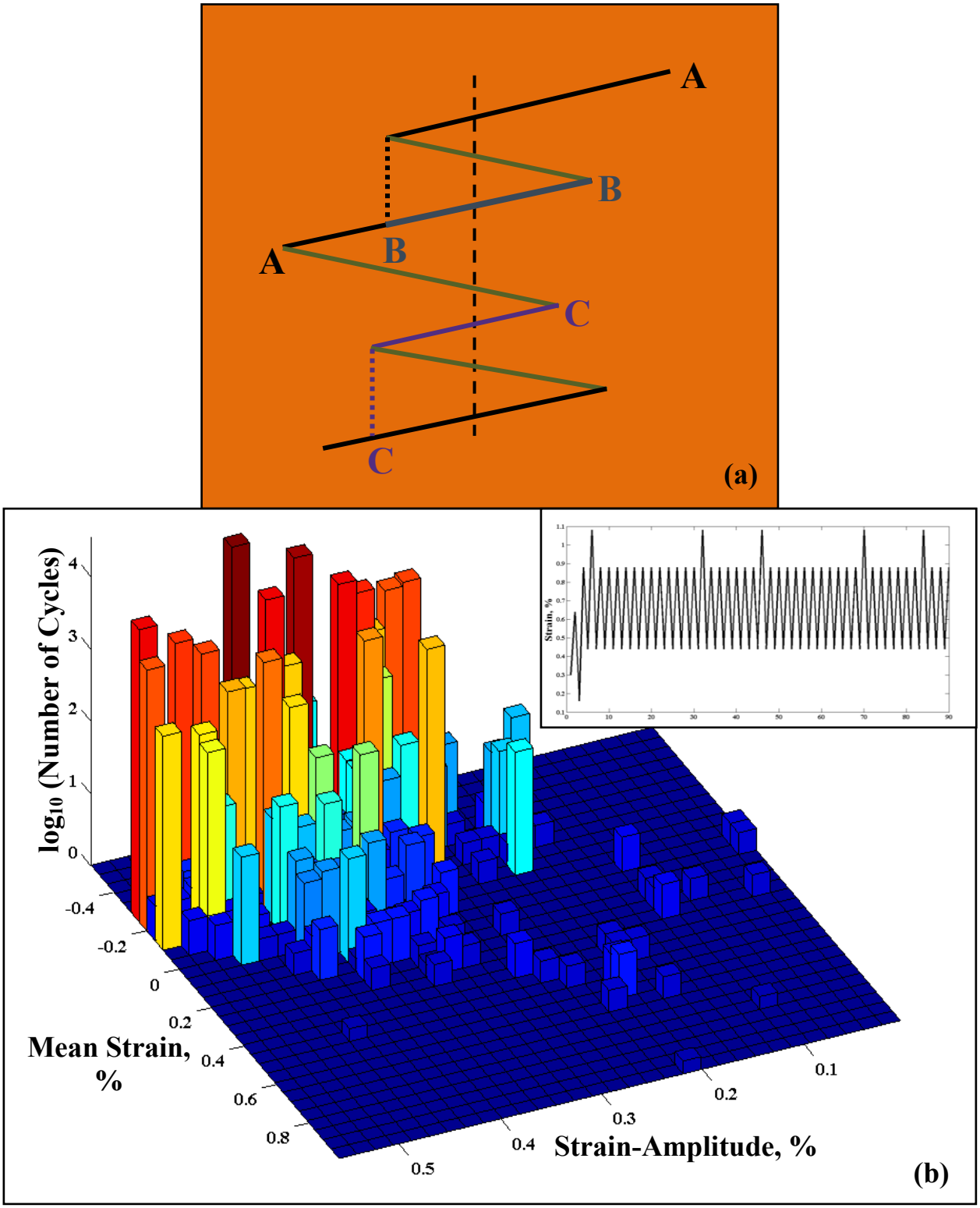

Figure 2-6 (a) Application of the rainflow cycle-counting algorithm to a simple load signal after the peak/valley reconstruction. Please see text for explanation; and (b) the resulting three dimensional histogram showing the number of cycles / half-cycles in each mean stress/strain – stress/strain amplitude bin.

Goodman Diagram

Before presenting the basics of the Goodman diagram, it is important to recognize that fatigue life of a material is a function of both the stress/strain amplitude and the stress/strain mean value. Often, the stress/strain mean values are quantified in terms of an R-ratio which is a ratio of the algebraically minimum and the algebraically maximum stress/strain values (associated with the constant-amplitude cyclic-loading tests). From the definition of the mean stress/strain, it can be readily shown that fatigue-loading tests carried out under constant R–ratio conditions, correspond to the tests in which the mean stress/strain scales with the corresponding amplitude. To construct the Goodman diagram, constant–R/constant-amplitude fatigue-test results are plotted, in a stress/strain amplitude vs. stress/strain mean-value diagram. As depicted, in Figure 2-7, constant-R data fall onto a line emanating from the origin. In Figure 2-7, R=0.1 and R=0.5 data are associated with a positive/tensile mean stress/strain value, R=-1 corresponds to a zero mean-value, while R=10 and R=2 pertain to a negative/compressive mean-value.

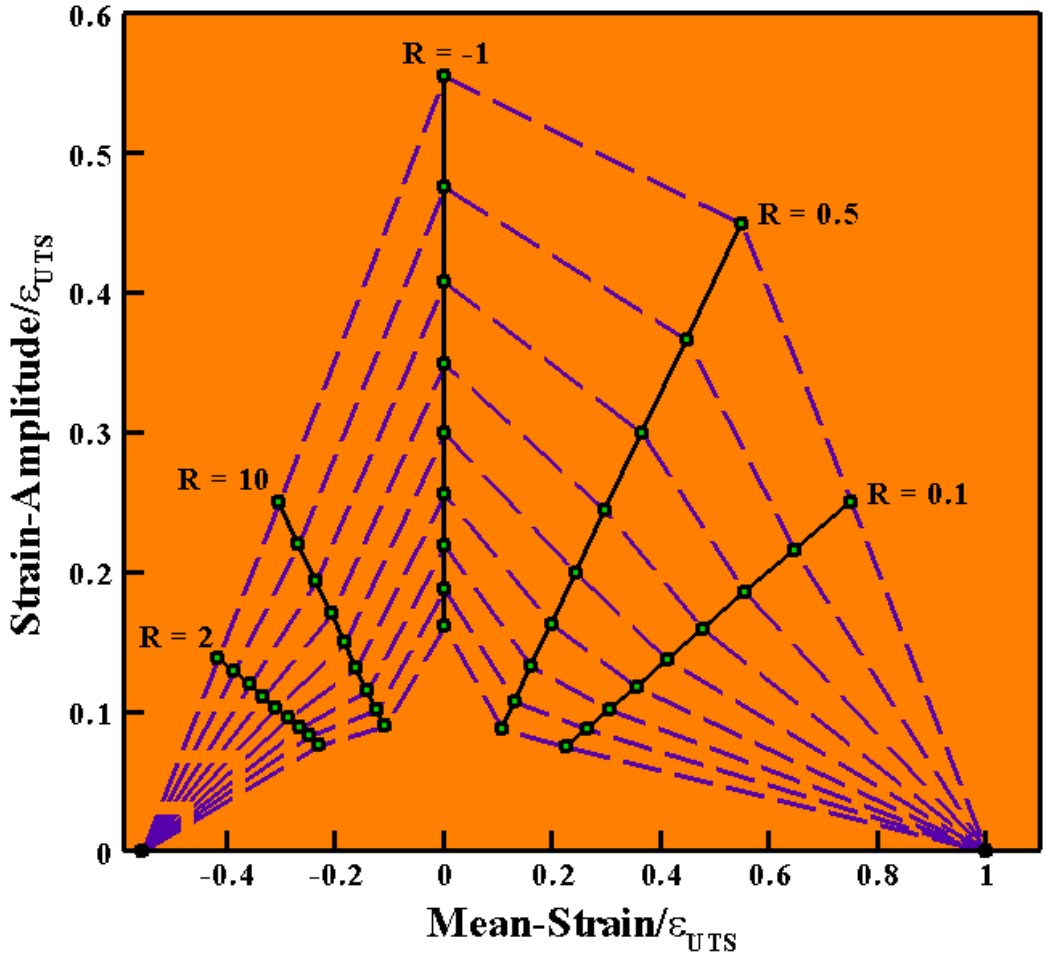

Figure 2-7 An example of the Goodman diagram showing constant fatigue-life data (dashed lines) and constant R-ratio data (the solid lines emanating from the origin).

To construct the corresponding linearized Goodman diagram, constant fatigue-life data associated with different R–ratio values are connected using straight lines. To complete the construction of the Goodman diagram, the constant fatigue-life lines are connected to the ultimate tensile stress/strain and to the ultimate compressive stress/strain points located on the zero-amplitude horizontal axis. The completed Goodman diagram displayed in Figure 2-7 then enables, through interpolation, determination of the fatigue life for any combination of the stress/strain amplitude and stress/strain mean-value. Hence, a three-dimensional histogram similar to that one shown in Figure 2-6(b) can be constructed except that the number of cycles here represents the total number of cycles to failure rather than the number of cycles in the analyzed load-signal. An example of such three-dimensional histogram is displayed in Figure 2-8.

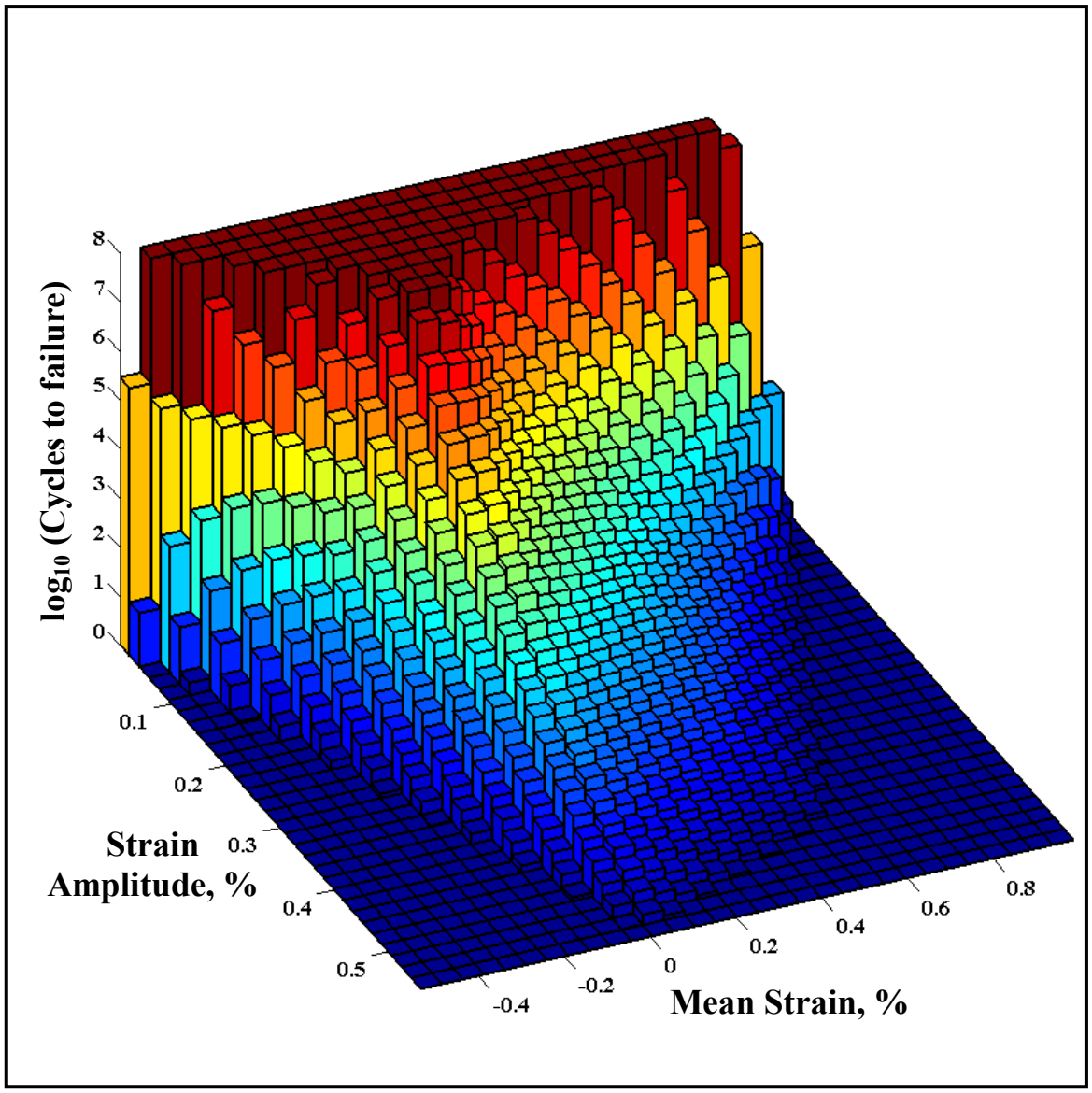

Figure 2-8 An example of the three-dimensional histogram showing the effect of stress/strain amplitude and the stress/strain mean-value of the material fatigue life.

Miner's Rule

The cycle counting procedure described earlier enables computation of the number of cycles/half-cycles in the given load signal which fall into bins of a three dimensional histogram, Figure 2-6(b). The use of the Goodman diagram, on the other hand, enables the computation of a similar tri-dimensional histogram but for the number of cycles to failure (i.e. the fatigue life), Figure 2-8. According to the Miner's rule, a ratio of the number of cycles and the corresponding total number of cycles, for a given combination of the stress/strain amplitude and stress/strain mean-value, defines a fractional damage associated with this component of the loading. The total damage is then obtained by summing the fractional damages over all combinations of the stress/strain amplitude and the stress/strain mean-value.

The total fatigue life under the given non-constant amplitude time-varying loading is obtained by dividing the load-signal duration by the total fractional damage. This procedure clearly postulates that fatigue failure corresponds to the condition when the total damage is equal to unity.

2.3.4 Wind-Turbine Blade Material Selection

From simple consideration of basic functional and longevity requirements for a HAWT blade it can be readily concluded that the main blade material-selection indices must be based on the following material properties:

(a) A high material stiffness to ensure retention of the optimal aero-dynamic shape by the blade while subjected to strong-wind loading conditions;

(b) A low mass density to minimize gravity-based loading; and

(c) A large, high-cycle fatigue strength to ensure the required 20-year life cycle with high reliability.

As mentioned earlier, the HAWT-blade is essentially a cantilever beam. If the material selection methodology proposed by Ashby [11] is utilized, then the first material selection index can be defined by requiring that the blade attains a minimal mass while meeting the specified bending-stiffness requirements (or alternatively that the blade attains maximum bending stiffness at a given mass level). Since the blade mass scales directly with its average cross-sectional area while its, stiffness scales roughly with the square of its, cross-sectional area, following Ashby's material selection procedure one can readily derive the following "*light, stiff beam*" material selection index:

$$M_1 = E^{1/2} / \rho \tag{2–2}$$

where E is the material's Young's modulus and ρ is its density.

The use of M_1 in the HAWT-blade material selection would normally identify foam-like materials as potential candidates. In these materials, their low stiffness (as quantified by the value of their Young's modulus, E) is more than compensated by their low ρ value. Consequently,

M_1 takes on a large value in the case of foam materials suggesting their suitability for use in the HAWT-blade applications. However, foam materials would yield very bulky blades which could present serious design, manufacturing, installation and operational problems. In addition, potentially open-cell structure and the associated high water-permeability/moisture-absorption can disqualify these materials from being used in the HAWT-blade applications. To overcome these problems, a second material selection index (more precisely, a lower-bound material-property limit) is proposed which requires that the HAWT-blade materials possess a minimal level of absolute stiffness, i.e.

$$M_2 \geq E \tag{2–3}$$

Typically, the minimal level of the Young's modulus required for a given-blade material is in a 15-20GPa range.

The two material selection indices defined above utilize two (E and ρ) out of the three previously identified material properties. Inclusion of the third material property (the fatigue strength) into a material selection index is, however, quite challenging. The reason is that, as discussed in the previous section, while the constant-amplitude fatigue strength associated with a given load mean-value and a given fatigue life can be readily determined HAWT-blade material selection requires the use of a variable-amplitude fatigue life.

As demonstrated in the previous section, the variable-amplitude fatigue life can be, in principle, computed for a given combination of the sustained quasi-static and time-varying loads. However, the procedure which is used in this calculation also entails the knowledge of the constant-amplitude fatigue data under different mean-value/R-ratio conditions. Since the generation of such data requires an extensive set of experimental tests, these data are not always available (in particular, in the open literature). Hence, the HAWT-blade material–selection

procedure used in the present work had to rely on more readily available material properties. Specifically, the endurance limit (i.e. the infinite-life constant-amplitude fatigue strength (under a zero mean loading, i.e., R=-1) will be used in the HAWT-blade material selection. Since materials with higher fracture toughness will fail in a more gradual manner (enabling a longer life of the blade between the time of initiation of the first cracks to the final failure). In this way, blades which have suffered fatigue-induced damage can be identified during periodic inspections and replaced, preventing more serious consequences, which may result from their unexpected catastrophic failure while in service.

Based on the discussion presented above, the third and the final HAWT-blade material selection index can be defined as:

$$M_3 = \sigma_{end} \cdot G_{Ic} \tag{2–4}$$

where, σ_{end} is the endurance limit and G_{Ic} the mode-I fracture toughness.

Clearly, the higher is the value of each of the three aforementioned material indices, the more suited is a given material for use in the HAWT-blade applications.

2.4. Results and Discussion

As discussed in Section 2.3, as part of the present work, a computer program was developed which enables automated creation of fully parameterized geometrical and meshed models, as well as the generation of a complete finite-element input deck for a large single composite-laminate 1MW HAWT blade. For a given choice of the airfoil shape, down-the-length taper and blade twist-angle, the program enables the user to specify lateral location of the shear webs, thickness for all aerodynamic (i.e. the outer skins) and structural (i.e. the shear webs, the spar caps, the adhesive layers) component thicknesses and composite- laminate ply stacking for each component as a whole or for different portions of the same component. In addition, interfacing of the model-generation computer program with an aerodynamics analysis computer program [5] enabled automated generation of the sustained wind-based loading conditions. This was complimented by the addition of non-constant amplitude reference time-varying loading to construct fairly realistic in-service loading conditions experienced by a large composite-laminate HAWT blade. The results obtained from the quasi-static finite element analyses of the HAWT-blade enabled not only investigation of the structural response of the blade (i.e. the extent of the blade tip deflection, the extent of blade-tip rotation due to bending-to-torsion coupling aero-elastic effects, etc.), but also predictions of the HAWT-blade high-cycle fatigue controlled life cycle.

Due to space limitations, only few representative results obtained in the present investigation will be shown and discussed in the following sections. This will be followed by a presentation of the results pertaining to the HAWT-blade material selection.

It should be noted that each portion of the present work included a mesh-convergence study to ensure that the finite-element mesh used was a good compromise between a

computational accuracy and computational cost. The results of the mesh convergence studies will not be shown for brevity.

2.4.1 The Baseline Case

At the beginning of the present investigation, a baseline case was first established/constructed, which is representative of the current commercial 1MW HAWT-blade designs. In the base-line case which is based on the S818 airfoil-shape [15], Figure 2-9(a), the primary structural member is a box-shape spar with (vertical) shear webs being located at distances equal to 15% and 50% of the section-chord length (as measured from the leading edge) and a substantial build-up in the spar cap thickness between the two vertical shear-webs. Examination of the HAWT-blade construction depicted in Figure 2-9(a) suggests that due to a relatively large spar-cap width and laminate thickness, good edge-wise bending stiffness/strength is expected. This is however, attained at the expense of the flat-wise bending stiffness/strength which could have been increased should the shaft portion of the shear web had been placed in the section of the blade associated with the largest blade thickness.

A typical planform, Figure 2-9(b), is assigned to the blade. The plan-form shows the variation of the blade chord-length with a radial distance r from the hub rotation axis with R being the radial location of the blade tip. Figure 2-9(b) shows that there is a linear taper from the maximum-chord section located at r/R=0.25 to the blade tip (r/R=1.0). The blade root is located at r/R=0.05 and is circular in cross section. The cross section is assumed to remain circular up to r/R=0.07 and thereafter undergoes a gradual transition to the pure airfoil section located at r/R=0.25.

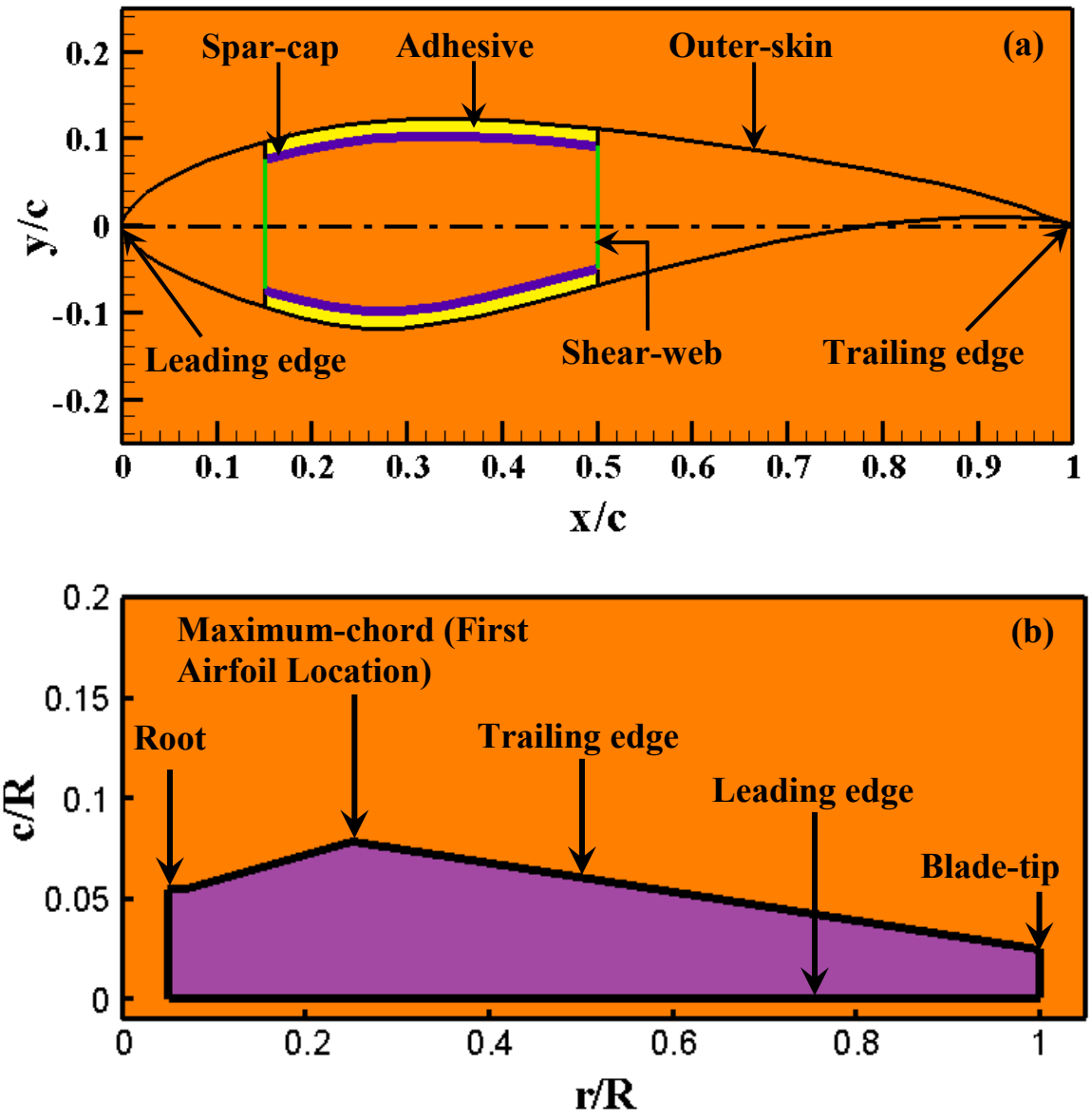

Figure 2-9 Baseline case of the HAWT blade analyzed in the present work: (a) the airfoil cross section; and (b) the planform.

As mentioned earlier, HAWT-blades are commonly twisted. Consequently, the baseline-blade case analyzed here was given a twist along its length. Specifically, the airfoil sections located at r/R=0.25, 0.5, 0.75 and 1.0 were twisted by 10^0, 2.5^0, 0^0, and -0.5^0, respectively.

The exterior airfoil skins and the interior vertical shear webs are constructed using a sandwich-like material consisting of ($-45^0/0^0/45^0$) tri-axial fiber-glass composite-laminate face-sheets separated by a balsa-wood core. The spar caps are constructed of alternating equal-thickness layers of the tri-axial laminates (described above) and unidirectional laminates making the contribution of 0^0 laminate and the off-axis laminate 70% and 30%, respectively. A summary of the composite-laminate lay-up sequences and ply thicknesses used in different sections of the baseline HAWT-blade design is provided in Table 2-1.

As mentioned earlier, all composite laminates mentioned above were based on epoxy matrix reinforced with E-glass fibers. As far as the adhesive layers connecting the spar caps to the interior faces of the skins are concerned, they were taken to be epoxy based. A summary of the stiffness, mass and composite mixture properties (where applicable) of the materials used are provided in Table 2-2. In Table 2-2, Tri, Uni and Mix are used to denote respectively the tri-axial, uni-axial and the spar-cap mixture composite laminates.

Layer Number	Material	Thickness
Exterior Skins and Internal Vertical Shear-webs		
1	**Gel Coat**	**0.68 mm**
2	**Random-mat Laminate**	**0.5 mm**
3	**Triaxial Laminate**	**1.2 mm**
4	**Balsa Core**	**0.005 × Chord-length**
5	**Triaxial Laminate**	**1.2 mm**
Spar-caps		
1	**Triaxial Laminate**	**1.2 mm**
2	**Uniaxial Laminate**	**1.2 mm**
Continued Alternating Layers of 1 and 2		

Table 2-1 HAWT-Blade Composite-laminate Lay-up Sequence

Property	Uni	Tri	Mix	Random Mat	Balsa	Gel Coat	Epoxy Adhesive
Axial Young's Modulus, E_{xx} (GPa)	**31.0**	**24.2**	**27.1**	**9.65**	**2.07**	**3.44**	**2.76**
Transverse Young's Modulus, E_{yy} (GPa)	**7.59**	**8.97**	**8.35**	**9.65**	**2.07**	**3.44**	**2.76**
In-plane Shear Modulus, G_{xy} (GPa)	**3.52**	**4.97**	**4.70**	**3.86**	**0.14**	**1.38**	**1.10**
Poisson's Ratio, v_{xy}	**0.31**	**0.39**	**0.37**	**0.30**	**0.22**	**0.3**	**0.3**
Fiber Volume Fraction, v_f	**0.40**	**0.40**	**0.40**	**–**	**N/A**	**N/A**	**N/A**
Fiber Weight Fraction w_f	**0.61**	**0.61**	**0.61**	**–**	**N/A**	**N/A**	**N/A**
Density, ρ (g/cm^3)	**1.70**	**1.70**	**1.70**	**1.67**	**0.l44**	**1.23**	**1.15**

Table 2-2 Summary of the HAWT-Blade Material Properties

Structural Response of the Baseline HAWT Blade

A set of examples of the results pertaining to the structural responses of the baseline HAWT-blade is displayed in Figure 2-10(a), 11, 12(a) and 13. These results pertain to the case when the blade is in the horizontal position; it is fixed at its root and subjected to the gravity loading, centrifugal forces along its length and the aerodynamic forces resulting from pressure difference across the blade thickness under the gust-based loads.

In Figure 2-10(a), a spatial-distribution plot of the baseline HAWT-blade external-skin displacement magnitudes is displayed. The results displayed in this figure reflect mainly the intrinsic edge-wise bending stiffness of the blade which is important for the overall wind turbine performance with respect to the ability of the blade to: (a) pass the tower with a required clearance and (b) impart the appropriate basic structural-dynamics characteristics to the HAWT-rotor and to the wind turbine, as a whole. It should be noted that an inset is provided in Figure 2-10(a) in order to display the outer-skin composite-laminate lay-up used in the baseline HAWT-blade design.

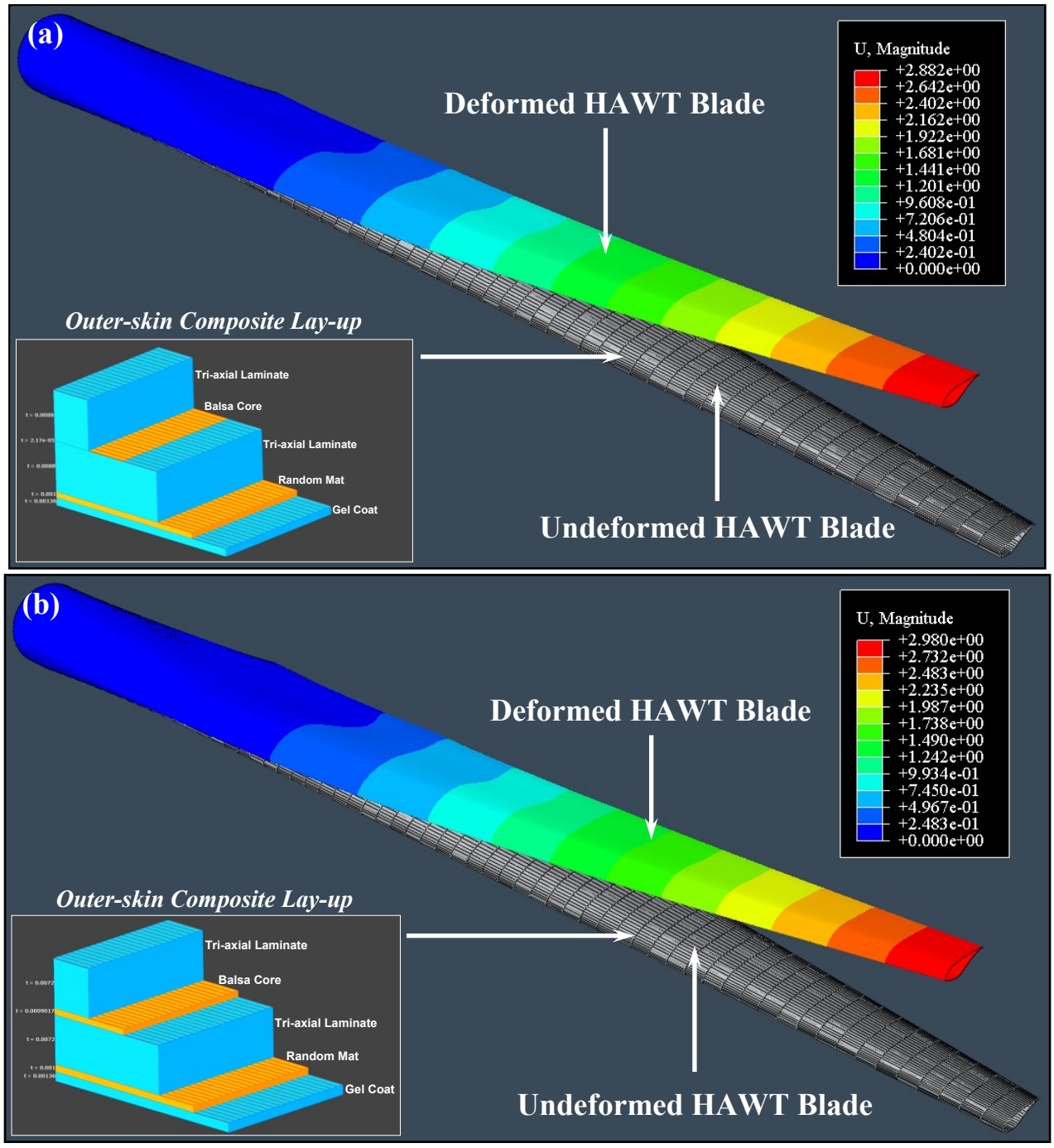

Figure 2-10 Displacement magnitude distribution over the HAWT blade outer skin caused by a 70m/s gust: (a) the baseline case; and (b) a modified-design case.

A change in the base-line HAWT-blade thickness as a function of normalized distance from the blade root is displayed in Figure 2-11 (the curve labeled the "*Baseline Design*" case). This change is a relative measure of the "*flap-wise*" stiffness of the blade.

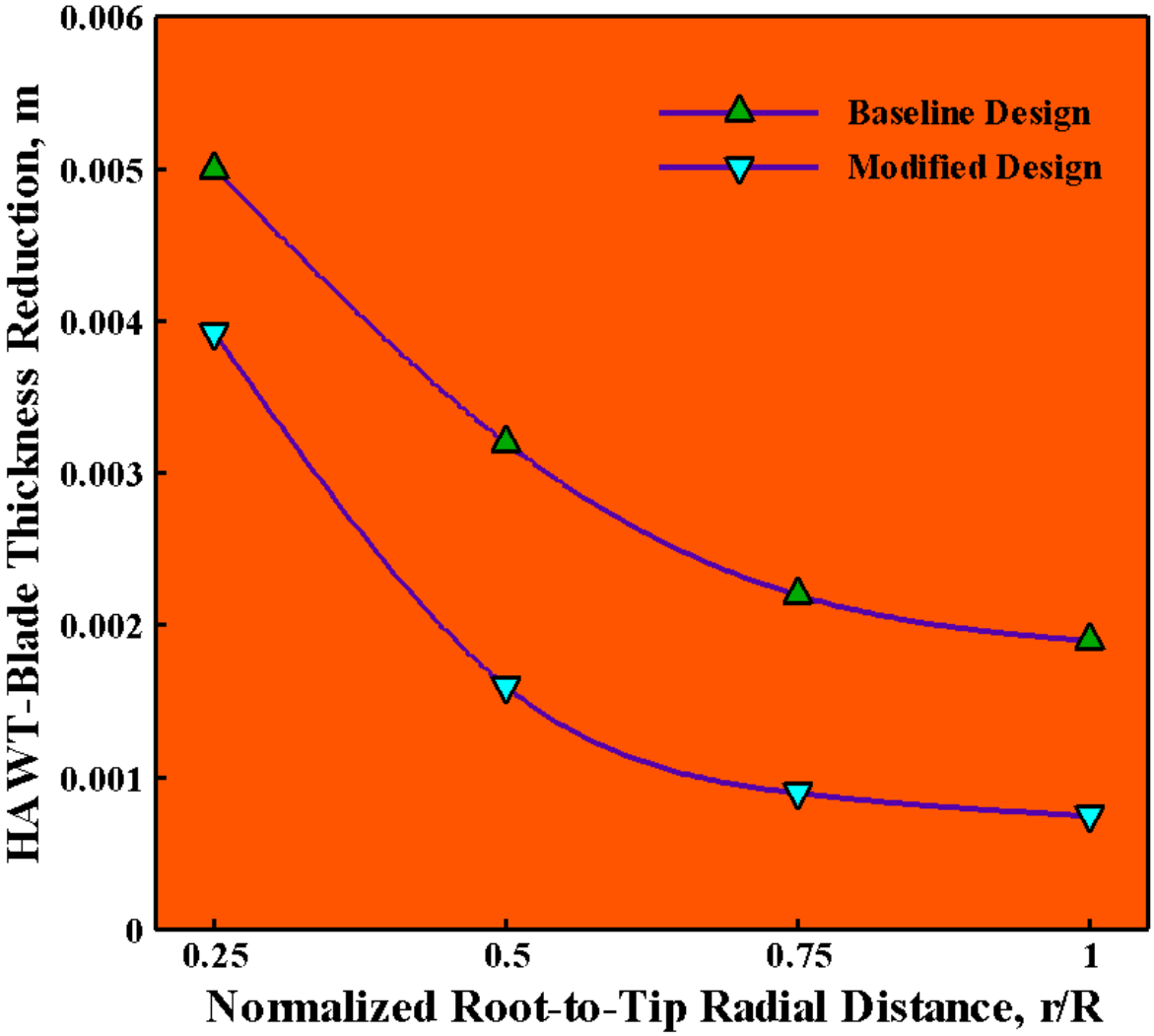

Figure 2-11 Variation of the gust-induced HAWT-blade thickness for the blade designs analyzed in the present work.

In Figure 2-12(a), a spatial-distribution plot of the von Mises equivalent stress over the interior box-shaped beam/spar is displayed. As mentioned earlier, the longitudinal spar is the key structural member of the blade and any compromise in its structural integrity implies an imminent loss of the HAWT-blade functionality and its structural failure. Before one can proceed with assessment of the HAWT-blade safety factor under the imposed gust-based loading conditions, one must recognize that the effective strength of the blade material may be reduced with respect to the nominally same material, but a material which is fabricated under normal material processing conditions and subjected to normal storage/handling practices.

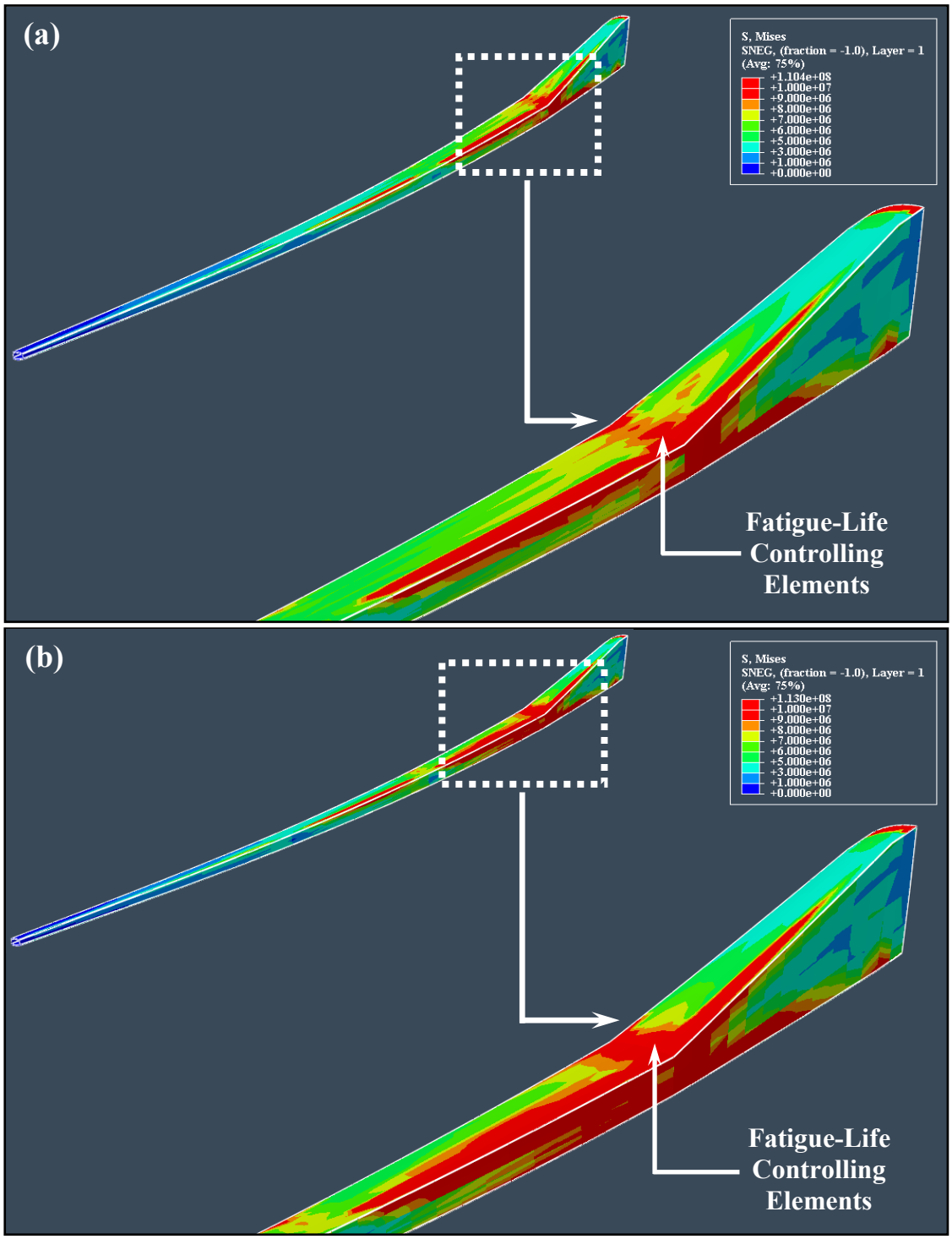

Figure 2-12 Von Mises equivalent stress distribution over the HAWT interior structural members (spar-cap and shear-webs) caused by a 70m/s gust: (a) the baseline case; and (b) a modified-design case.

In comparison to the standard materials-processing practice, the material in the HAWT-blade is generally fabricated under different conditions (i.e. the material is laid-up at the time when the blade is being manufactured) and is exposed to varying temperatures, ultraviolet-radiation, humidity, salinity, and other environmental conditions (and is, hence, prone to accelerated aging/degradation). To account for all these strength-degrading effects, the IFC 61400-1 standard [13] prescribes a set of so-called "material partial safety" factors. Following the procedure described in Ref. [12], the overall/cumulative material strength-reduction factor was assessed as 2.9. Hence for the prototypical 500MPa longitudinal strength (before it is corrected using the material partial safety factors) for the E-glass/epoxy composites used in the present work, the smallest safety factor (defined as a ratio of the corrected material strength and the maximum von Mises stresses in the blade = 110.4MPa) is estimated as (500MPa/2.9)/110.4MPa = 1.57.

In Figure 2-13 (the curve labeled the "*Baseline Design*" case), a variation of the gust-induced twist angle in the blade is plotted as a function of the normalized distance from the blade root. As discussed earlier, bending-to-torsion aero-elastic effects which are responsible for the observed gust-induced blade tip twist may play a significant role in the overall blade aerodynamic efficiency and in the passive control of the blade pitch (critical for self-protection of the blades structural integrity under excessive wind induced loads).

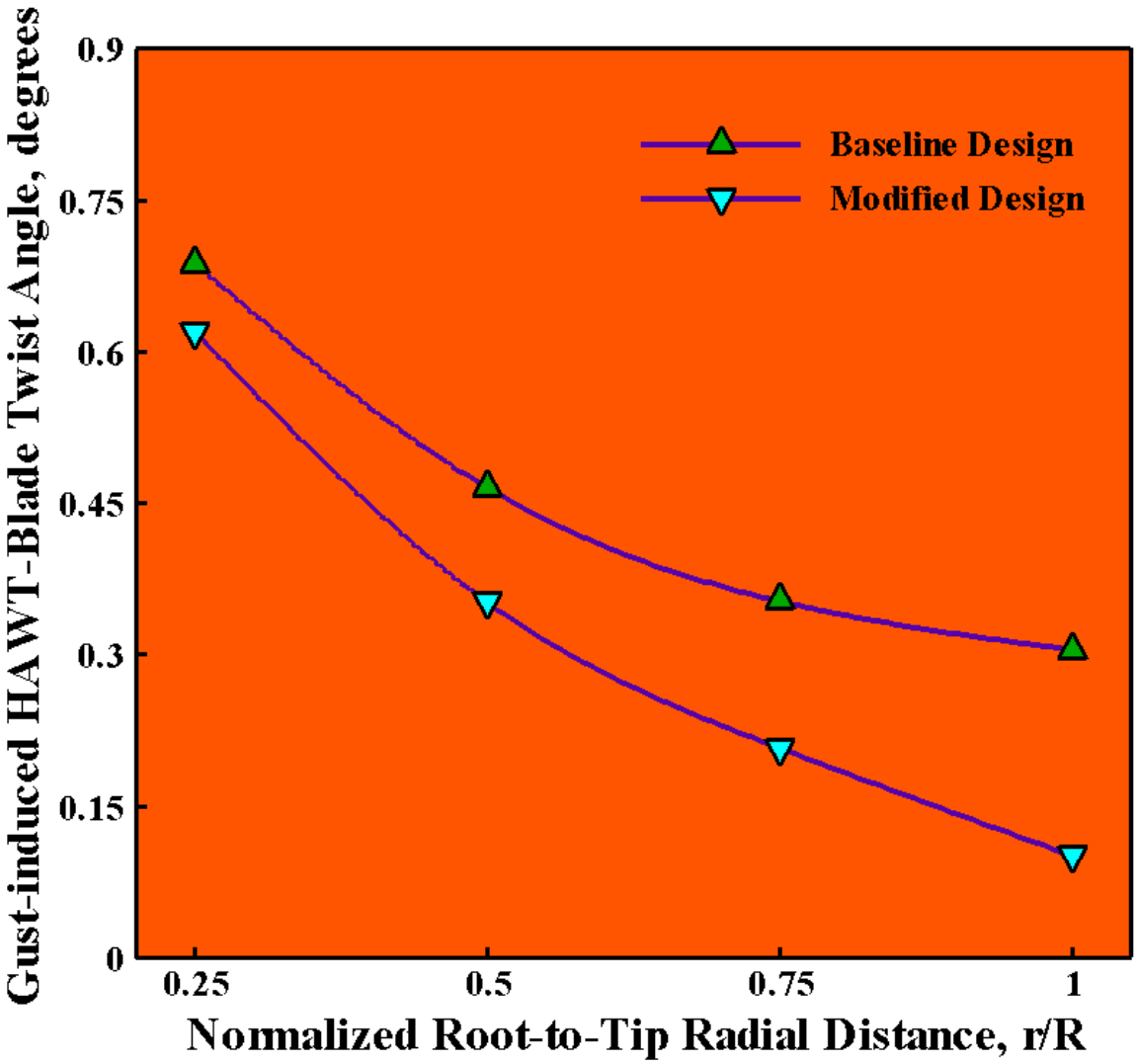

Figure 2-13 Variation of the gust-induced HAWT-blade twist angle for the blade designs analyzed in the present work.

Fatigue Life of the Baseline HAWT Blade

As mentioned earlier, the so-called "*proportional loading*" case was adopted in the present work according to which stresses scale directly with the load magnitude and the orientation of their principal components remains unchanged with a change in the load magnitude. Hence, the stress state in the blade at any instant can be calculated by simply scaling the quasi-static stress results obtained in previous section (e.g. Figure 2-12(a)), with the instantaneous wind-based load magnitude. However, before the fatigue life assessment procedure based on the rain flow cycle counting algorithm, the Goodman diagram and the Miner's rule can be applied, the issue of multi-dimensional stress state within different components of the HAWT-blade has to be addressed. While in metallic materials compressive component(s) of the time-varying stresses are not generally harmful, composite materials (due to the potential for fiber micro-buckling) are generally quite susceptible to in-place compressive stresses. To provide a fairly conservative assessment of the baseline HAWT-blade fatigue life and take into account the effect of compressive stresses, the stress multi-axiality is handled through the use of a "*signed*" von Mises equivalent stress. That is, the entire stress state is assumed to be quantified by the von Mises equivalent stress to which a sign is attached consistent with the sign of the largest (by magnitude) principal stress.

As mentioned earlier, time varying component of the wind-induced loading is modeled by the WISPER load signal. While scaling this load signal (whose values range between 1 and 64 with the level of 25 corresponding to a zero load), the WISPER mean value was assumed to correspond to the previously computed wind mean speed of 7.6 m/s.

When the procedure outlined in Section 2.3.3 was applied, the fatigue life of the baseline HAWT-blade was estimated as 32.8years. In Figure 2-12(a), the elements which control the

fatigue life of the blade are identified. As could have been expected, these elements are located in the airfoil/root transition region which is subjected to the highest in-service loads.

2.4.2 HAWT-Blade Design Modifications

The geometrical-/meshed-model generator program and the structural and fatigue life assessment analyses developed in the present work are at a level that they can be readily incorporated into a design-optimization algorithm. This will be done in our future communication and the same design-optimization methodology as presented in our recent work [14] will be used. In this section, however, a couple of examples will be shown in order to demonstrate how few minor changes in the HAWT-blade design and composite/laminate lay-up can have significant changes to the blade response/functionality.

In Figure 2-10(b), a plot is shown of the spatial distribution of displacement magnitude over the HAWT-blade surface. In comparison to the baseline HAWT-blade design, Figure 2-10(a), the design associated with the results displayed in Figure 2-10(b) corresponds to repositioning of the right shear web from x/c=0.5 to x/c=0.45. Also, the composite-laminate lay-up used in the modified design case was changed by increasing the balsa core thickness by 15% relative to the baseline case. The new composite-laminate lay-up is displayed as an inset, in Figure 2-10(b).

A comparison of the results displayed in Figure 2-10(a) and 2–10(b) shows that edge-wise stiffness of the HAWT-blade, as measured by its tip-displacement, is a fairly sensitive function of the lateral position of the right shear web.

A change in the modified-design HAWT-blade thickness as a function of the normalized distance from the blade root is displayed in Figure 2-11 (the curve labeled “Modified Design”). A comparison of the results displayed in this figure for the two HAWT-blade designs analyzed indicates that repositioning of the right shear-web has measurably compromised flap-wise bending stiffness of the blade.

In Figure 2-12(b), a spatial-distribution plot of the von Mises stress over the interior spar is displayed for the same HAWT-blade design as that used to generate the results displayed in Figure 2-10(b). A comparison between the results displayed in Figure 2-12(a) and 12(b) shows that the stresses are somewhat higher in the modified blade design. Consequently, the safety factor obtained using the same procedure as in the baseline case was found to be reduced from 1.57 to 1.52. Combining this finding with that made in conjunction with Figure 2-10(a)-(b) and 11 suggests that there is a need for the use of design-optimization technique to identify the blade design with an optimal combination of its functional-performance measures.

The effect of a change in the shear-web/spar-cap composite-laminate lay-up relative to that used in the baseline case on the extent of bending-to-torsion coupling of the HAWT-blade is shown in Figure 2-13 (the curve labeled the "*Modified Design*" case). In this figure, a variation of the gust-induced twist angle along the length of the blade is displayed. A comparison of the two sets of results displayed in Figure 2-13 shows that significant changes in the extent of bending-to- torsion coupling are feasible through modifications in the composite-laminate layup.

The fatigue-life assessment procedure based on the use of the rainflow cycle-counting algorithm, the Goodman diagram and the Miner's rule yielded a fatigue life of 27.4 years for the HAWT-blade design used to generate the results displayed in Figure 2-10(b) and 12(b). Again, it is clear that both the blade-performance and longevity are sensitive to the blade design and that the use of design-optimization methods could be quite beneficial. This aspect of the HAWT-blade design will be addressed in our future communication.

2.4.3 HAWT-Blade Material Selection

In Section 2.3.4, it was discussed that the three most important material properties which control suitability of a given material for use in the HAWT-blade applications are the density, the Young's modulus and the fatigue strength/life. Three related material-selection indices were also derived and it was argued that one of them, i.e. index M_2, Eq. (2–3), is essentially a material-property limit index which is used to screen out the materials which do not possess the sufficient level of stiffness, as quantified by their Young's modulus. Consequently, the condition $M_2 \geq 20\text{GPa}$ was applied at the onset of the present material selection process to eliminate unacceptable materials. Then, indices M_1 and M_3 are used to carry out the HAWT-blade material selection in accordance with the procedure outlined in Section 2.3.4. In constructing the corresponding material-selection charts various open-literature material-data sources were consulted. The Young's modulus data used pertain to the mean in-plane value of this quantity. The results of the material selection procedure carried out in the present work are summarized in Figure 2-14(a)-(c). It should be noted that, for clarity, materials appearing in Figure 2-14(a)-(c) are labeled using numbers and a legend is provided in Figure 2-14(d) for the number labels used.

In Figure 2-14(a), the Young's modulus vs. density data are compiled for a number of thermosetting polymer matrix composites. A log-log plot was used in Figure 2-14(a) and three lines with a constant slope were drawn in accordance with the definition of the first material selection index, M_1, Eq. (2–2). The three guide-lines (with a slope of 2.0) are associated with the M_1-levels of 10,500, 22,500 and 40,000 $\text{GPa}^{0.5}/(\text{kg/m}^3)$ with the larger M_1 value causing the guide-line to be shifted upward. Also, a 20GPa dashed guide-line is displayed in Figure 2-14(a) in order to denote the previously-established lower-bound for the Young's modulus of the candidate

materials for use in the HAWT-blade applications. With respect to the M_1 material selection index alone, the optimal materials are those located above the topmost guide-line.

In Figure 2-14(b), a linear-linear plot is shown of the data pertaining to the endurance limit (x-axis) and the toughness (y-axis) for the same set of materials as that used in Figure 2-14(a). Three solid guide-lines are also shown in Figure 2-14(b) and they correspond to the M_3-levels of 1, 7 and 13 $MPa^2 \cdot m$. Again, with respect to the M_3 material selection index alone, the optimal materials are those located above the topmost guide-line.

Since different material are identified as optimal if material selection is based on the use of a single index (M_1 or M_3), Figure 2-14(a)-(b), a procedure was developed here which takes into account both of these material indices in the HAWT-blade material-selection process. A linear-linear plot of M_3 vs. M_1 material selection indices (normalized by the values of these two indices in a commonly used HAWT- blade material, i.e., an E-glass uni-directionally-reinforced epoxy–matrix composite) is shown in Figure 2-14(c). The three solid lines displayed in Figure 2-14(c) correspond to the values of 2, 5 and 10 for a combined material selection index, M, defined as:

$$M = wM_1 + (1-w)M_3 \tag{2–5}$$

where the weighting factor w for the material selection index M_1 is set 0.5, making the weighting factor for the mutual selection index M_3 also equal 1.0-0.5=0.5.

Simple examination of the results displayed in Figure 2-14(c) reveals that, for the most part, carbon-fiber reinforced PEEK-(Poly-ether-ether-ketone) or polyimide-matrix composites are favored. In the case of E-glass fiber reinforced composites, a phenolic matrix appears to be preferred over the traditionally used epoxy or poly-ester. The main reason for the carbon fibers outperforming the E-glass fibers is their higher density-normalized stiffness, while the emergence of the phenolic polymers appears to be related to higher toughness levels imparted to the

composite material by this polymeric matrix. The main reason for the currently preferred HAWT-blade material, i.e. E-glass fiber reinforced epoxy–matrix composites, is the relatively low material cost combined with the overall good structural/fatigue-life performance.

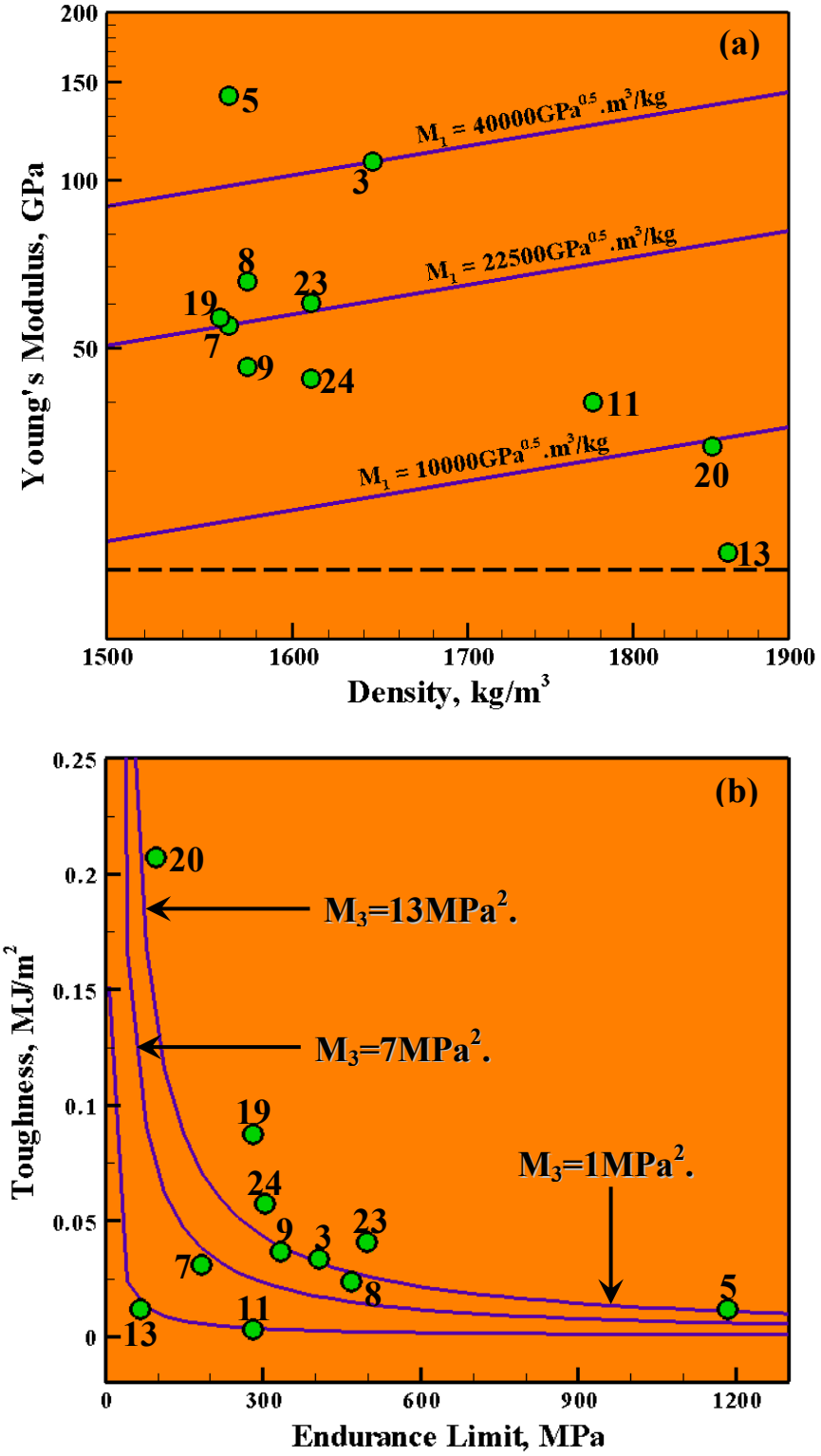

Figure 2-14 Material property charts used in the HAWT-blade material selection process. Please see text for details.

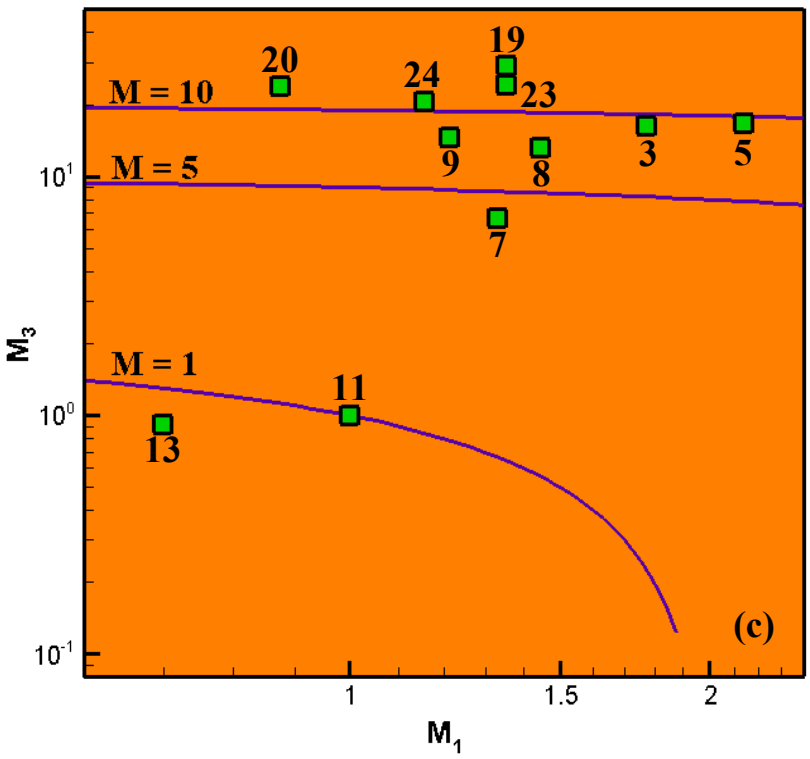

3 – Cyanate Ester HM Carbon Fibre UD Composite Quasi isotropic Laminate
5 – Epoxy HS Carbon Fibre UD Composite 0 Lamina
7 – Epoxy HS Carbon Fibre UD Composite Quasi Isotropic Lamina
8 – Epoxy HS Carbon Fibre UD Composite Quasi Isotropic Lamina
9 – Epoxy HS Carbon Fibre Woven Fabric Composite QI Laminate
11 – Glass Epoxy Unidirectional Composite
13 – Epoxy E Glass Fibre Woven Fabric Composite QI Laminate
19 – PEEK IM Carbon Fibre UD Composite Quasi Isotropic Laminate
20 – Phenolic E Glass Fibre Woven Fabric Composite Biaxial Lamina
23 – Polyimide HS Carbon Fibre Woven Fabric Composite Biaxial Lamina
24 – Polyimide HS Carbon Fibre Woven Fabric Composite QI Laminate
HM – High Modulus
IM – Intermediate Modulus
HS – High Strength
UD – Unidirectional
QI – Quasi isotropic

Figure 2-14. Continued.

It should be noted that the material-selection procedure employed in the present work is based on the use of stereotypical material properties of the common thermosetting-polymer matrix composite plies/laminae reinforced with either uni-directional or cross-woven fiber mats. Consequently, the procedure does not include the full effect of composite-laminate architecture. That is, properties of the composite laminates are derived not only from those of the associated laminae but can be tailored over relatively large range by varying plies thickness and orientation, stacking sequence as well as by hybridization of the laminate. Laminate hybridization can be carried out on the ply scale (by combining fibers of different types, e.g. by combining glass and carbon fibers within the single laminae) or on the laminate scale (by stacking plies with different fiber reinforcements, e.g., by alternate stacking of the glass-fiber reinforced plies and the carbon-fiber reinforced plies). It should be noted that ply-level hybridized laminae can be readily included in the present material selection procedure once the appropriate material properties become available. On the other hand, the effect of laminate-level hybridization can be readily included through the ply-stacking optimization procedure mentioned in Section 2.4.2.

2.5. Summary and Conclusions

Based on the results obtained in this portion of the work, the following main summary remarks and conclusions can be drawn:

1. A fully parameterized computer program has been developed for automated generation of the geometrical and finite-element meshed models of the Horizontal Axis Wind Turbine (HAWT) blades. The program enables the specification of the basic blade geometrical and structural parameters (e.g., airfoil shape, size and lateral location of the longitudinal spar/beam, thickness of the adhesive layers joining the beam to the external blade skins, etc.) as well as the basic and locally different composite-laminate architecture and lay-up sequence.

2. Fairly realistic, yet generic wind-based (sustained and time-varying) loading conditions are compiled and applied to a stereotypical 1MW HAWT-blade in order to assess its structural response as well as to assess its longevity.

3. A preliminary parameter variation study was conducted which revealed that further improvements in the HAWT-blade performance are possible with targeted changes in the blade geometry and the composite-laminate lay-up.

4. A simple HAWT-blade material selection procedure was developed which combines weighted contributions of the material indices pertaining to the blade performance and longevity. The results revealed that, as expected, from the performance point of view carbon-fiber reinforced composites are preferred over the traditionally-used E-glass fibers reinforced composites and that epoxy may not be best choice for the composite-material matrix.

2.6. References

1. "***20% Wind Energy by 2030, Increasing Wind Energy's Contribution to U.S. Electricity Supply***," DOE/GO-102008-2567, July 2008, http://www.osti.gov/bridge
2. T. Burton, D. Sharpe, N. Jenkins, E. Bossanyi, "***Wind Energy Handbook***," John Wiley & Sons Ltd, 2001.
3. M. Selig, "***UIUC Airfoil Coordinates Database – Version 2.0***," http://www.ae.uiuc.edu/mselig/ads/coord_database.html, 2006.
4. MATLAB, ***The Language of Technical Computing***, 7th Edition, 2006 (The MathWorks Inc., MA.
5. M. Hepperle, "***JavaFoil Users Manual***," http://www.mh-aerotools.de/airfoils/javafoil.htm, 2005.
6. A. A. Ten Have, "***WISPER and WISPERX: Final Definition of Two Standardized Fatigue Loading Sequences for Wind Turbine Blades***," NLR-TP-91476U, National Aerospace Laboratory NLR, Amsterdam, the Netherlands, 1992.
7. ABAQUS/Standard Version 6.8-1, ***User Documentation***, Dassault Systemes, 2008.
8. M. Matsuiski, T. Endo, ***"Fatigue of metals subjected to varying stress"***, Japan Soc. Mech. Eng, 1969.
9. J. Goodman, "***Mechanics Applied to Engineering***," London: Longman, Green, & Co., 1899.
10. M. A. Miner, "***Cumulative damage in fatigue***," J. Appl. Mech, 12:A159–64, 1945.
11. M. F. Ashby, "***Materials Selection in Mechanical Design,***" Third Edition, Elsevier Butterworth Heinemann, 2005.
12. D. A. Griffin, ***"WindPact Turbine Design Scaling Studies Technical Area-1-Composite Blades for 80- to 120-Meter Rotor"***, NREL, Washington, 2001.
13. IEC-61400-3 (2009-02) Wind turbines - Part 3: ***"Design requirements for offshore wind turbines Maintenance Result Date"***: p 201
14. M. Grujicic, G. Arakere, W. C. Bell, H. Marvi, H. V. Yalavarthy, B. Pandurangan, I. Haque and G. M. Fadel, "***Reliability-based Design Optimization for Durability of Ground-vehicle Suspension-system Components***," Journal of Materials Engineering and Performance, 19, 3, pp. 301–313, 2010.
15. D. M. Somers, "***The S816, S817 and S818 Airfoils***", NREL, Pennsylvania, 1992.
16. http://www.siemens.com/press/en/presspicture/index.php?view=list&content=&tag=EWP201309062, accessed May 6, 2014.

CHAPTER 3: HORIZONTAL–AXIS WIND–TURBINE: GEAR–BOX FAILURE VIA TOOTH–BENDING FATIGUE

3.1. Abstract

Wind energy is one of the most promising and the fastest growing alternative-energy production technologies which have been developed in response to stricter environmental regulations, the depletion of fossil-fuel reserves, and the world's ever-growing energy needs. This form of alternative energy is projected to provide 20% of the US energy needs by 2030. For economic reasons, wind turbines (articulated structures which convert wind energy into electrical energy) are expected to operate, with only regular maintenance, for at least twenty years. However, some key wind-turbine components (especially the gearbox) tend to wear down, malfunction and fail in a significantly shorter time, often three to five years after installation, causing an increase in the wind-energy cost and in the cost of ownership of the wind turbine. Clearly, to overcome this problem, a significant increase in long-term gearbox reliability needs to be achieved. While purely empirical efforts aimed at identifying shortcomings in the current design of the gearboxes are of critical importance, the use of advanced computational methods engineering analyses can also be highly beneficial. The present work demonstrates the use of the finite element analysis in modeling and elucidating the root cause of one of the gear failure modes (i.e. tooth-bending fatigue) under a variety of normal operating and extreme wind-loading conditions.

3.2. Introduction

The main objective of the present work is to address the problem of long-term reliability and the modes of failure of gearboxes used in wind (energy-harvesting) turbines. Consequently, the concepts most relevant to the present work are: (a) wind-energy harvesting; (b) wind-turbine gearbox reliability; and (c) root causes and main modes of gear damage and failure. In the remainder of this section, a brief description is provided for each of these concepts.

3.2.1 Wind Energy Harvesting

The depletion of fossil-fuel reserves, stricter environmental regulations and the world's ever-growing energy needs have led to deployment/ utilization of various alternative/renewable energy sources, among which wind energy is one of the most promising and the fastest growing installed alternative-energy production technologies. In fact, it is anticipated that by 2030, at least 20% of the U.S. energy needs will be met by various onshore and offshore wind-farms.

A wind turbine is essentially a converter of wind energy into electrical energy. This energy conversion is based on the principle of having the wind drive a rotor, thereby transferring wind power to the electrical generator. To attain greater structural stability of the rotor and a high value of aerodynamic efficiency, the rotor is usually constructed as a set of three aerodynamically shaped blades. The blades are (typically) attached to a horizontal hub (which is connected to the rotor of the electrical generator, via a gearbox/drive–train system, housed within the nacelle). The rotor/hub/nacelle assembly is placed on a tower and the resulting wind energy converter is referred to as the Horizontal Axis Wind Turbine (HAWT).

To reduce the energy production cost (typically expressed in $/kW•hr), commercial wind turbines have grown considerably in size over the last 30 years. The large wind-turbine economics is based on the fact that as the hub-height/wind-turbine rotor radius increases, the average wind speed/wind energy captured increases due to the so called "wind shear effect." Consequently, for the same energy production level, lesser number of wind turbine units is required, which in turn leads to a reduction in the cost of operation of the farm. As the size of the wind turbine rotor increases, the structural performance, durability and dynamic-stability requirements tend to become more and more challenging to meet.

Turbine blades and the gearbox are perhaps the most critical components/subsystems in the present designs of wind turbines. The present work deals only with the issues related to the performance, reliability and modes of failure of gearbox components. In our recent work [5, 6], two-level multi-disciplinary design-optimization methods and tools were developed for determination of the optimal shape and size of glass-fiber reinforced epoxy-matrix composite HAWT blades.

3.2.2 Wind Turbine Gearbox Reliability

Wind-turbine gearbox failure remains one of the major problems to the wind-energy industry [14]. The root causes of gearbox failure in the earlier designs are associated with the problems related to: (a) fundamental design errors; (b) manufacturing deficiencies; and (c) under-estimation of the operating loads. While these problems have been mainly eliminated over the last 20 years, wind-turbine gearboxes still generally fail to achieve their design life goal of twenty years. The combination of these high failure rates and the high cost of gearboxes, has contributed to: (a) increased cost of wind energy; and (b) higher sales price and cost of ownership of wind-turbines. Clearly, to make wind energy a more viable renewable-energy alternative, the long-term gearbox reliability must be significantly increased.

The current state of understanding of the basic features and processes/mechanisms related to the failure of wind-turbine gearboxes can be summarized as follows [14]: (a) gearbox failure appears to be of a generic character, i.e. not strongly related to the differences in their design; (b) gearbox failure cannot be generally attributed to poor workmanship; (c) gear failure is frequently the result of excessive and unexpected (e.g. misalignment) loading conditions. In other cases, the gearbox failure may be initiated in overloaded bearings, and the resulting bearing debris propagate to the gears, causing tooth wear and gear misalignment; and (d) the essential features and mechanisms of gearbox damage and failure appear not to change with size of the wind turbine.

A labeled schematic of a prototypical wind turbine gearbox is shown in Figure 3-1. The low-speed stage of the gearbox is a planetary configuration with either spur (the present case) or helical gears. In this configuration, the planetary-gear carrier is driven by the wind-turbine rotor,

the ring gear is stationary/reactionary, while the sun pinion shaft drives the intermediate gearbox stage, and, in turn, the high-speed stage. Typically, both the intermediate and high-speed stages are composed of helical gears (the damage and fatigue-failure of which is the subject of the present manuscript).

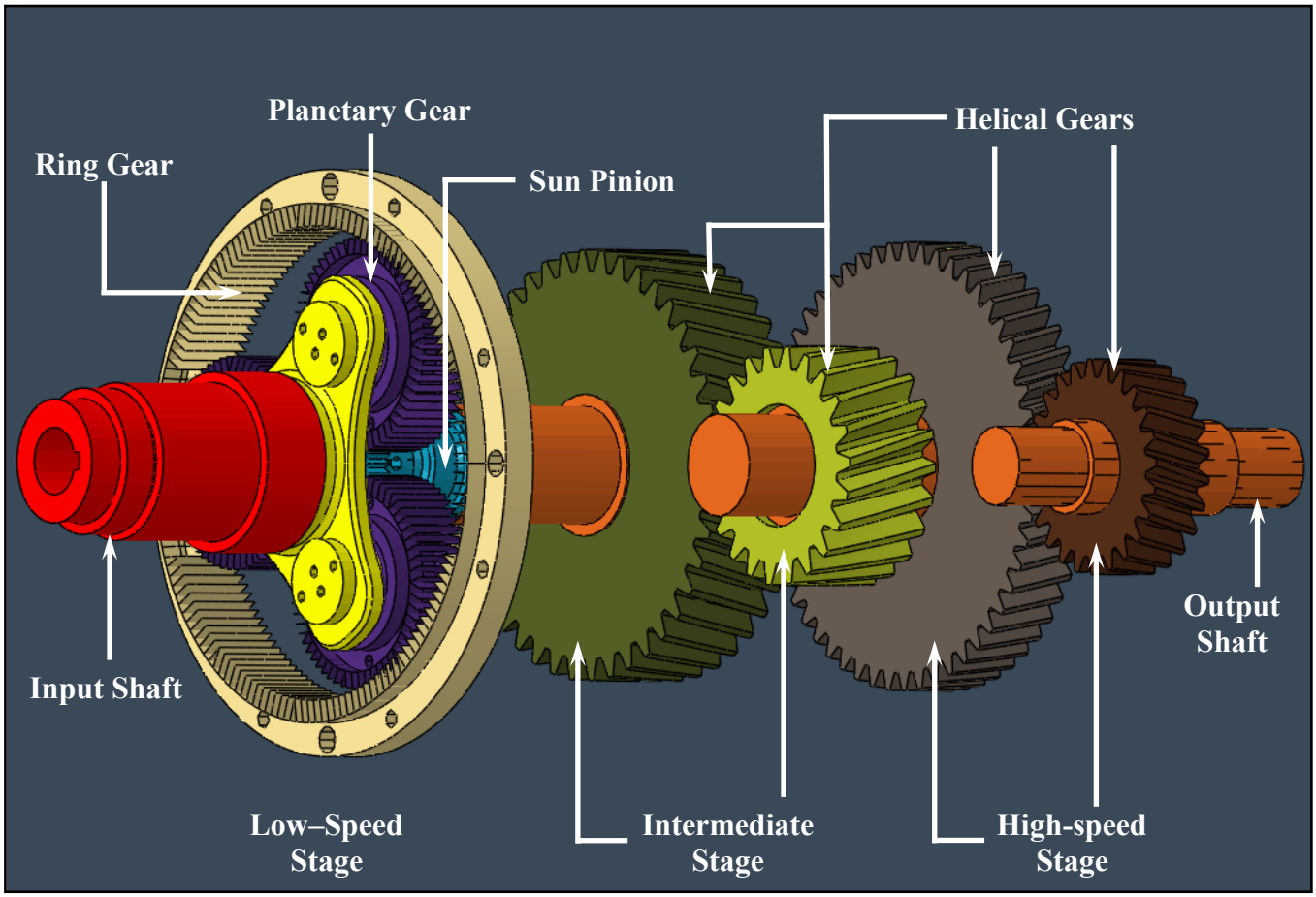

Figure 3-1 Schematic of a prototypical wind-turbine gearbox. The major components and sub-systems are identified.

3.2.3 Main Modes of Gear Damage and Failure

Post-mortem examination of the field wind-turbine gearboxes revealed two main modes of gear failure [2, 3]:

(a) *tooth-bending high-cycle fatigue failure* – The defining features of this gear-tooth failure mode can be summarized as: (i) Fatigue cracks are typically found to be initiated at the root radii on the engaged (loaded in tension) side of the gear teeth; (ii) Cracks tend to originate preferentially at the locations associated with the largest principal stresses. Under normal loading conditions, the highest stresses are typically found at the tooth base, while under abnormal loading conditions (e.g. in the case of gear misalignment), the location of the highest stresses is related to the character and extent of loading abnormality; (iii) Crack growth is generally characterized by an L-shaped trajectory, i.e. the crack, nucleated at the engaged side of the tooth initially propagates inwards and below the tooth, and then makes a turn outward towards the opposite side of the same tooth (leading to the tooth breaking off); and (iv) Due to the subsequent overloading effects, failure of one tooth is often accompanied by failure of adjacent teeth, in rapid succession; and

(b) *surface contact fatigue failure* – Depending on the character and spatial distribution of the stresses at and beneath the contact surfaces, the following three modes of this type of failure have been identified: (i) Formation of microscopic pits typically associated with rolling-contact fatigue loading conditions along the pitch-line of gear teeth. These pits mainly affect the extent and nature of the gear-tooth surface roughness; (ii) Formation of larger-size surface pits which are typically attributed to a combination of sliding- and rolling-contact fatigue loading conditions (typically away from the pitch-line, especially in the regions characterized by

"*negative*"-sliding conditions). These pits act as potent stress risers and can facilitate initiation of other gear-tooth failure mechanisms (e.g. tooth-bending fatigue failure); and (iii) Spallation, i.e. formation and shedding of large flakes from the contact surfaces. Often, the spall debris is formed as a result of fracture along the interface between the case-hardened surface layer and the tooth core.

3.2.4 Main Objectives

To respond to the aforementioned problems related to the relatively frequent and costly failure of wind-turbine gearboxes, wind-turbine manufacturers tend to re-engineer critical components and include them into new subsystems (gearbox designs). To demonstrate the utility of the new designs, the re-engineered gearboxes are installed and field testing is started. While this approach may help address the gearbox reliability concerns, it is associated with long field-test times and costly post-mortem failure analyses necessary to achieve the desired level of confidence in the new design. In addition, when the field-test results become available, it is likely that new wind-turbine, and hence new gearbox designs, will dominate the market, making the field-test results less valuable.

To overcome the foregoing shortcomings of the purely empirical approach aimed at addressing the wind-turbine gearbox reliability, the use of advanced computer-aided engineering methods and tools is advocated in the present work. While such a computational approach is not a substitute for the aforementioned re-engineer-and-field-test approach, it can provide complementary insight into the problem of wind-turbine gearbox failure and help gain insight into the nature of the main cause of this failure. In addition, computational engineering analyses enable investigation of the gear failure in a relatively short time, under: (a) a variety of wind-loading conditions comprising both the expected design-load spectrum as well as the unexpected extreme loading conditions; and (b) conditions in which the transfer of loads (both primary torque loads and non-torque loads) from the shaft and mounting reactions occurs in a non-linear or unpredicted manner.

Considering the aforementioned potential benefits of the computer-aided engineering analysis, the main objective of the present work is to carry out a computer-aided engineering analysis of the tooth-bending high-cycle fatigue-failure of wind-turbine helical gears found in the intermediate-speed stage of the gearbox. Failure of these gears is often found to be the cause of the wind-turbine gearbox failure.

3.2.5 Chapter Organization

A concise summary of the computational approach used in the investigation of wind-turbine gearbox gear-bending stress and high-cycle fatigue failure analyses is presented in Sections 3.3 and 3.4, respectively. The key results yielded by the present investigation are presented and discussed in Section 3.5, while the main conclusions resulting from the present work are summarized in Section 3.6.

3.3. Finite-Element Stress Analysis

As mentioned earlier, helical-gear tooth-bending high-cycle fatigue-failure is one of the main modes of failure of wind-turbine gearboxes. Since fatigue-cracks are generally initiated at surface locations associated with the largest contact (as well as sub-surface) stresses, one must determine accurately spatial distribution and temporal evolution of the contact (as well as through-the-volume) stresses, before attempting to assess fatigue strength and service life of wind-turbine gears. Accurate determination of these stresses is most conveniently carried out through a finite-element-based analysis. In the present section, details regarding the helical mating-gear interactions during the transfer of wind-turbine torque loads and the finite-element modeling and analysis procedure employed are presented.

3.3.1 Problem Formulation

The basic problem analyzed here involves the structural response of two mating wind-turbine helical gears located within the intermediate stage of the gearbox, during the transfer of the torque loads under different expected and abnormal wind-loading conditions. The results to be obtained will subsequently be used to assess tooth-bending high-cycle-fatigue failure-strength and service-life of the subject helical gears under imposed wind-loading conditions.

3.3.2 Computational Analysis

The finite-element analysis (FEA) used here is an adaptation of our recent work [7, 10, 12] dealing with the friction stir welding process model. In the remainder of this section, a brief overview is provided of the key aspects of the employed FEA.

1) Geometrical Model

The geometrical model/computational domain of the problem analyzed in this portion of the work is depicted in Figure 3-2(a). The model comprises two mating helical gears and their two associated shafts. Under ideal gear-meshing conditions (i.e. in the absence of gear misalignment), the axes of the two shafts are parallel and aligned in the global Cartesian y-direction, as indicated in Figure 3-2(a). On the other hand, under abnormal loading conditions involving gear misalignment, the axes of the two shafts are assumed not to be parallel.

2) Meshed Model

Each of the four components (i.e. two helical gears and two shafts) is meshed using four-node, first-order, reduced-integration, tetrahedral continuum elements. After conducting a mesh-sensitivity analysis to ensure that further refinement in the mesh size does not significantly affect the results (not shown for brevity), a meshed model containing ca. 460,000 tetrahedron elements (of comparable size and shape) was adopted for the analysis. A close-up of the meshed model used in this portion of the work is depicted in Figure 3-2(b).

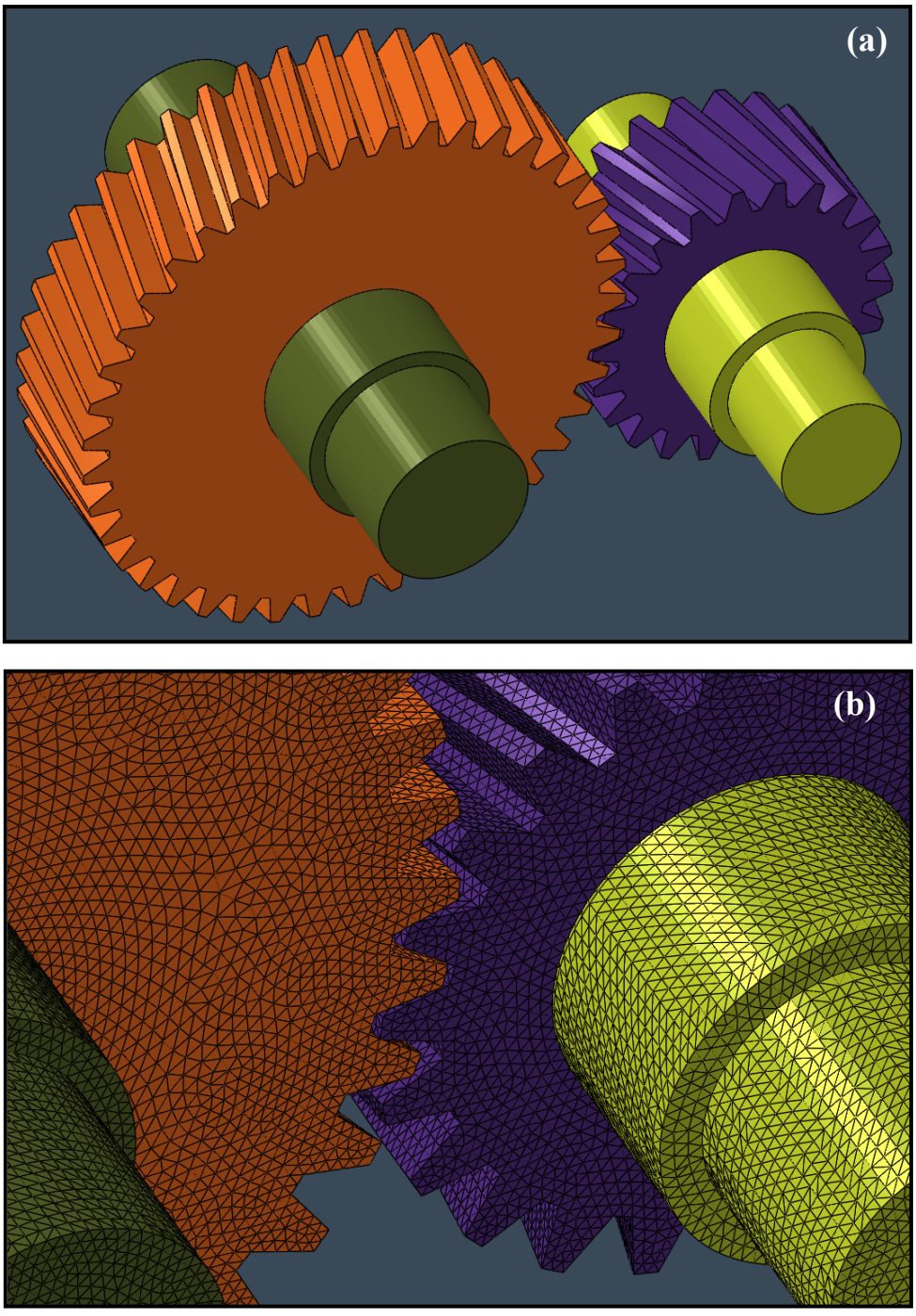

Figure 3-2 (a) Geometrical model; and (b) Close-up of the meshed model consisting of two helical gears and two shafts, used in the present work.

3) Computational Algorithm

Due All calculations are based on a transient, displacement-based, purely Lagrangian, conditionally-stable, explicit finite-element algorithm. Before the analysis is initiated, the two-gear-shaft assembly is assumed to be stationary and subject only to the gravity-induced stresses. Then, at the beginning of the analysis, the rotational speed of the shaft associated with the larger (driving) helical gear is ramped up to its final value by ensuring that: (a) the two gears are engaged; (b) the shaft of the smaller (driven) helical gear is allowed to rotate about its axis; and (c) a prescribed torque load is transmitted through engagement, and subsequent meshing of the gears. It should be noted that the shafts and their respective gears are connected so that the rotation of a shaft implies rotation of the associated gear and vice versa.

4) Initial Conditions

As mentioned above, the two-gear/shaft assembly is initially assumed to be stationary and only the stresses associated with gravity-loading are assumed to be present within each component.

5) Boundary Conditions

The following boundary conditions were utilized: (a) the center points of the shaft end-faces (treated as rigid surfaces) are prevented from undergoing translation; (b) rotational speed is prescribed to one of the end-faces of the driving shaft (i.e. the shaft associated with the larger helical gear); and (c) a constant opposing torque is applied to one of the end-faces of the driven shaft (i.e. the shaft associated with the smaller helical gear).

6) Contact Interactions

The gear-gear normal interactions are analyzed using a penalty-contact algorithm. Within this algorithm, (normal) penetration of the contacting surfaces is resisted by a set of linear springs which produces a contact pressure that is proportional to the depth of penetration. Typically, maximum default values, which still ensure computational stability, are assigned to the (penalty) spring constants. Force equilibrium in a direction collinear with the contact-interface normal then causes the penetration to acquire an equilibrium (contact-pressure dependent) value. It should be noted that no contact pressures are developed unless (and until) the nodes on the "*slave surface*" contact/penetrate the "*master surface*". On the other hand, the magnitude of the contact pressure that can be developed is unlimited. As far as the tangential gear-gear interactions (responsible for transmission of the shear stresses across the contact interface) are concerned, they are modeled using a modified Coulomb friction law. Within this law, the maximum value of the shear stresses that can be transmitted (before the contacting surfaces begin to slide) is defined by a product of the contact pressure and a static (before sliding) and a kinetic (during sliding) friction coefficient. In addition, to account for the potential occurrence of a "*sticking condition*" (sliding occurs by shear fracture of the softer of the two materials, rather than by a relative motion at the contact interface), a maximum value of shear stress (equal to the shear strength of the softer material) that can be transmitted at any level of the contact pressure is also specified.

As far as the friction coefficient is concerned, it is generally assumed that this contact parameter is controlled by the formation and shearing of micro-welds (i.e. micron-sized regions at which contacting surface asperities are bonded). Furthermore, it is recognized that the friction coefficient is a function of a number of factors such as the contact interface (mean) temperature, slip speed, contact pressure, contact surfaces' roughness/topology, etc. To assign the appropriate

value to the friction coefficient, functional relationships derived in our recent work [8] were analyzed.

7) Material Model

The helical-gear and shaft materials are assumed to be of an isotropic (linearly) elastic and (strain-hardenable) plastic character. Due to the isotropic nature of the material(s) used, the elastic response is fully defined in terms of two elastic engineering moduli (e.g. the Young's modulus, E, and the Poisson's ratio, ν). The plastic response of the material(s) is defined by specifying the following three functional relations: (a) a yield criterion; (b) a flow rule; and (c) a constitutive law. These functional relations and their parameterization for the gear and shaft reference material, AF1410, a secondary-hardening martensitic tool steel, can be found in [9, 11, 12].

8) Computational Tool

The problem of helical gear engagement, meshing and torque-load transfer is executed using an explicit solution algorithm implemented in ABAQUS/Explicit, a general-purpose finite element solver [1]. This algorithm was chosen because it is associated with comparatively low computational cost when dealing with three-dimensional problems dominated by contact (as is the present case). Since the dynamic, explicit finite-element formulation is only conditionally stable, care had to be taken to ensure that the time increments during the analysis do not exceed the critical time increment [4].

3.4. Fatigue Strength and Life-Cycle Prediction

In this section, a brief description is provided regarding the post-processing procedures applied to the results yielded by the finite element analysis (described in the previous section) in order to assess the fatigue-life of the helical gears used within the intermediate stage of the gearbox.

3.4.1 Fatigue-Crack Initiation

Fatigue-crack initiation is a complex process which is greatly influenced by factors such as material microstructure, the character and intensity of the applied stress, and on various micro- and macro-scale geometrical parameters. Since fatigue-crack initiation is often observed to be associated with the formation of persistent slip bands and plastic-accommodation zones around grain and twin boundaries, inclusions, etc. [e.g. 13], it is generally treated as a (strain-controlled) short-cycle fatigue process. In other words, formation of fatigue cracks is assumed to be preceded by the operation of highly-localized plastic-deformation processes. Furthermore, it is generally assumed that: (a) fatigue-crack initiation occurs in the region associated with the maximum value of the largest principal stress; and (b) the transition from the strain-controlled fatigue-crack initiation stage to the stress-controlled fatigue-crack growth stage occurs at a threshold crack length, (typically set to a value in the 0.1–0.2 mm range).

Due to its strain-controlled character, the fatigue-crack initiation process is modeled here by combining:

(a) the conventional Coffin-Manson equation, $\Delta\varepsilon'_p/2 = \varepsilon'_f (2N_i)^c$, where $\Delta\varepsilon'_p/2$ is the equivalent plastic strain amplitude, ε'_f is the fatigue ductility coefficient, c is the fatigue ductility exponent, N_i is the number of cycles required to reach a_{th}, and $2N_i$ is the corresponding number of stress reversals; with

(b) the additive decomposition of the total equivalent strain amplitude $\Delta\varepsilon'/2$ into its elastic, $\Delta\varepsilon'_e/2$, and plastic components;

(c) fatigue micro-yielding constitutive law, $\Delta\varepsilon'_p/2 = \varepsilon'_f \left(\Delta\sigma'/2\sigma'_f\right)^{1/n'}$, where $\Delta\sigma'/2$ is the

equivalent-stress amplitude, n' is the cyclic strain-hardening exponent and σ'_f is the fatigue strength coefficient;

(d) Hooke's law, $\Delta\sigma' = E \cdot \Delta\varepsilon'_e$, where E is the Young's modulus and

(e) stress-based fatigue-life relation, $\Delta\sigma'/2 = \sigma'_{FL} + \sigma'_f (2N_i)^b$, where σ'_{FL} is the material fatigue/endurance limit and b is a material parameter.

This procedure yields the following equation:

$$\frac{\Delta\varepsilon'}{2} = \frac{(\Delta\sigma'/2) - \sigma'_{FL}}{E} + \varepsilon'_f \left[\frac{(\Delta\sigma'/2) - \sigma'_{FL}}{2\sigma'_f} \right]^{1/n'} = \frac{\sigma'_f}{E} (2N_i)^b + \varepsilon'_f (2N_i)^c \qquad (3\text{–}1)$$

Once the region within a gear associated with the largest value of the maximum principal stress is identified and the corresponding equivalent stress amplitude computed (using the finite-element results), Eq. (3–1) can be solved iteratively to get the number of cycles to fatigue-crack initiation N_i for a given combination of gear-material and cyclic loading. To include the effect of surface condition on the fatigue-crack initiation process, σ'_{FL} is typically multiplied by a positive coefficient (smaller than 1.0) which accounts for the effect of initial surface roughness or contact-fatigue-induced surface damage.

3.4.2 Fatigue-Crack Growth

Once the crack reaches its threshold length a_{th}, the fracture process transits into the fatigue-crack growth regime. Since this regime is stress-controlled, it is modeled here using the theory of linear elastic fracture mechanics (LEFM). Specifically, fatigue-crack growth is modeled using the Paris equation, which relates the rate of increase in the sub-critical crack length with an increase in the loading-cycle number, $\mathrm{d}a/\mathrm{d}N$, with the (maximum – minimum) applied (generally mixed-mode) stress-intensity cycling range $\Delta K \geq \Delta K_{th}$ as:

$$\frac{da}{dN} = C\left[\Delta K(a)\right]^m \tag{3–2}$$

where, ΔK_{th}, C and m are material parameters. The maximum number of fatigue-loading cycles in the crack-growth regime, N_g, is obtained by integrating Eq. (3–2) as:

$$\int_0^{N_p} dN = \frac{1}{C} \cdot \int_{a_{th}}^{a_c} \frac{da}{\left[\Delta K(a)\right]^m} \tag{3–3}$$

where, a_c is the critical crack length (i.e. the crack length at which unstable fracture is initiated under static loading conditions). To carry out the integration described by Eq. (3–3), one must know the functional relationship between the ΔK (i.e. K) and the current crack length under the given crack configuration and loading conditions. While closed-form K vs. a functional relations are available for the cracks of simple geometry and for the simple loading cases, under more complex crack-geometry/-loading scenarios, this function must be evaluated numerically. In the present work, the interaction-integral finite-element method [1] is used to determine the sought-after K vs. a relation. Within this method, the K vs. a relation is obtained by: (a) introducing an initial crack of length a_{th} at the location yielded by the foregoing crack-initiation analysis; (b) setting the incremental fracture surface equal to the plane orthogonal to the

maximum principal stress; (c) controlling the crack growth by successively prescribing small crack extensions; (d) evaluating the mixed-mode stress intensity factor as a function of the associated modes I, II and III stress intensity factors as

$$K^2 = K_I^2 + K_{II}^2 + \frac{2}{1-\nu} K_{III}^2 \tag{3–4}$$

where ν is the Poisson's ratio; and (e) repeating the procedure until the computed mixed-mode stress intensity factor reaches its critical (unstable crack growth) value.

3.5. Results and Discussion

In this section, the main results of the finite-element stress analysis and the post-processing fatigue-crack initiation and growth analyses are presented and discussed. While the present computational framework enables the generation of results under numerous gear-material/transfer-torque/gear-misalignment scenarios, due to space limitations, only a few prototypical results will be presented and discussed.

3.5.1 Temporal Evolution/Spatial Distribution of Gear-Tooth Stresses

In this section, a few prototypical finite-element results pertaining to the distribution of the maximum principal stress over one tooth of the driven helical gear are presented and discussed in the context of the expected fatigue-life (in particular, the portion of the fatigue-life related to the crack-nucleation stage).

1) Aligned-Gear Case

Typical temporal evolution and spatial distribution of the maximum principal stress over the surface of a tooth of the driven gear (for the case of perfectly aligned shafts) are shown in Figure 3-3(a)–(d). It is seen that as expected, the maximum principal stress displays cyclic behavior. That is, as the gears rotate, the (unengaged) tooth in question becomes progressively engaged and subsequently disengaged. Furthermore, examination of the results displayed in Figure 3-3(a)–(d) reveals that during this process, the location associated with the largest value of the maximum principal stress changes with the extent of gear rotation. This observation is important since, as postulated by the fatigue-crack initiation model described in an earlier section, fatigue-cracks are nucleated (via the operation of plastic micro-yielding phenomena) in the region associated with the highest value of the maximum principal stress.

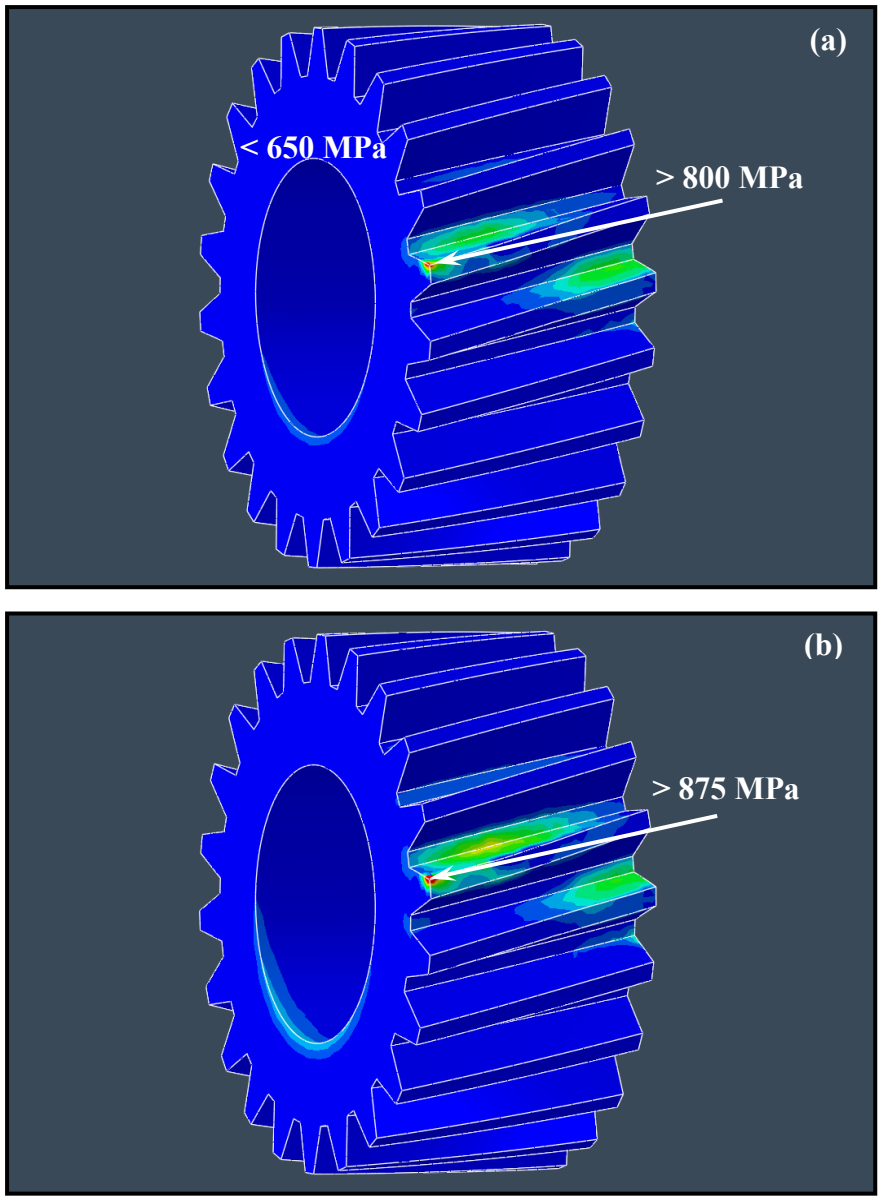

Figure 3-3 Typical temporal evolution and spatial distribution of the maximum principal stress over the surface of a tooth of the driven gear (for the case of perfectly aligned shafts).

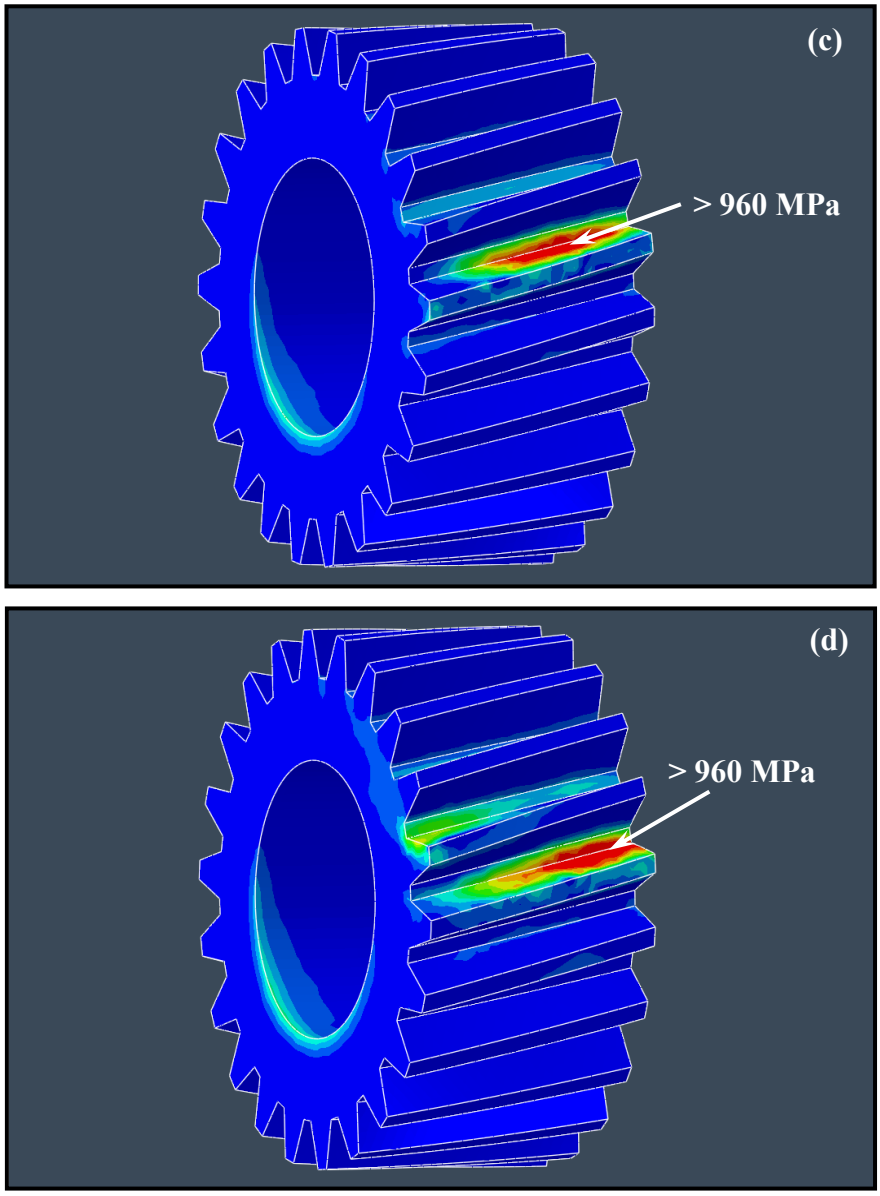

Figure 3–3 Continued

The effect of the torque transferred by the gear-pair analyzed on the largest value of the maximum principal stress, and on the corresponding value of the von Mises equivalent stress, in the subject gear-tooth (for the case of perfectly aligned shafts) is shown in Figure 3-4. It is seen that as the transferred torque increases, both the highest value of the maximum principal stress and the associated von Mises stress on the surface of the subject gear-tooth also increase (approximately linearly). This finding then implies, and the results of the fatigue-service-life analysis (presented below) will confirm, that as the transferred torque increases, the number of loading cycles required for fatigue-crack nucleation decreases.

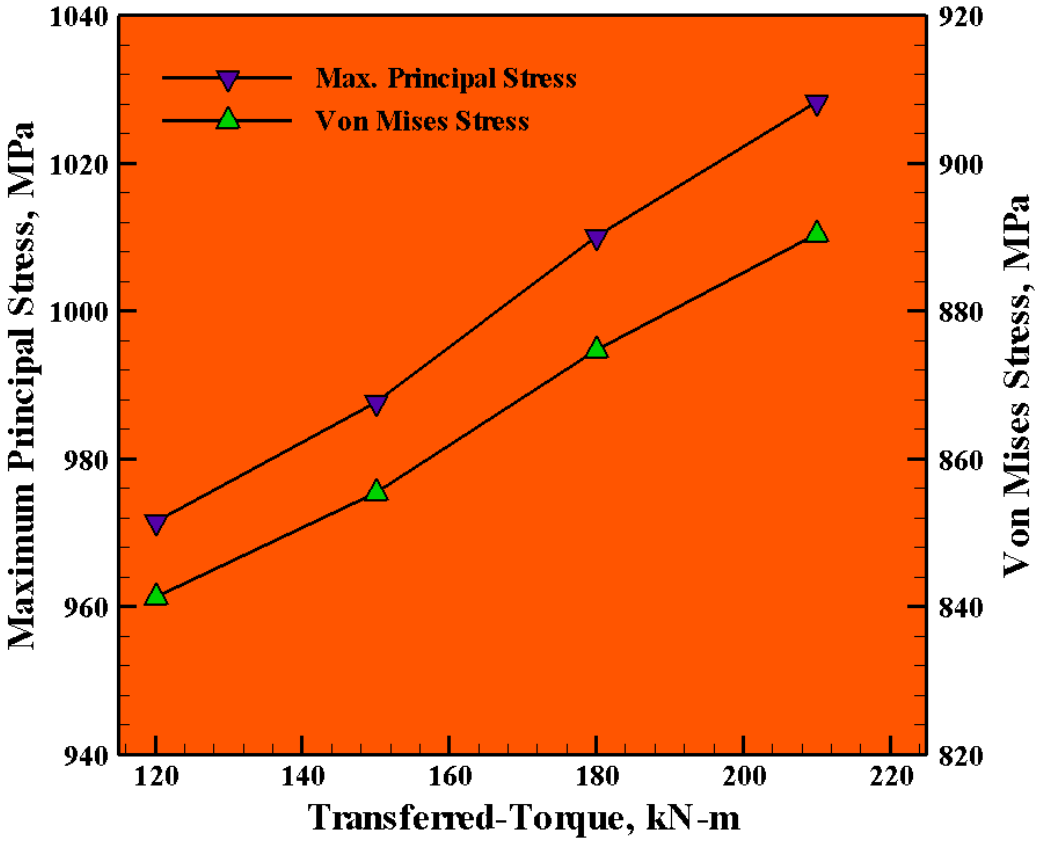

Figure 3-4 The effect of the torque transferred by the gear-pair analyzed on the largest value of the maximum principal stress in the subject gear-tooth).

2) Effect of Gear Misalignment

The effect of shaft misalignment (as quantified by the corresponding misalignment angle, α), at a constant transferred-torque of 165 kN.m, on the spatial distribution and the magnitude of the gear-tooth maximum principal stress, at the instant when the subject gear-tooth experiences the largest value of the maximum principal stress, is depicted in Figure 3-5(a)–(d). Examination of the results shown in Figure 3-5(a)–(d) reveals that as expected, as the extent of gear misalignment increases, the magnitude of the largest principal stress increases, and its location drifts (relative to that in the perfectly-aligned case). Since the location associated with the largest value of the maximum principal stress is considered to be the place of fatigue-crack initiation, the results displayed in Figure 3-5(a)–(d) suggest that the location of the fatigue-induced gear-tooth failure may change with the extent of gear misalignment. This finding further suggests that perhaps, change in the location of the gear-tooth failure (relative to that in the perfectly-aligned-gear case) can be regarded as an indication of shaft-misalignment-induced failure.

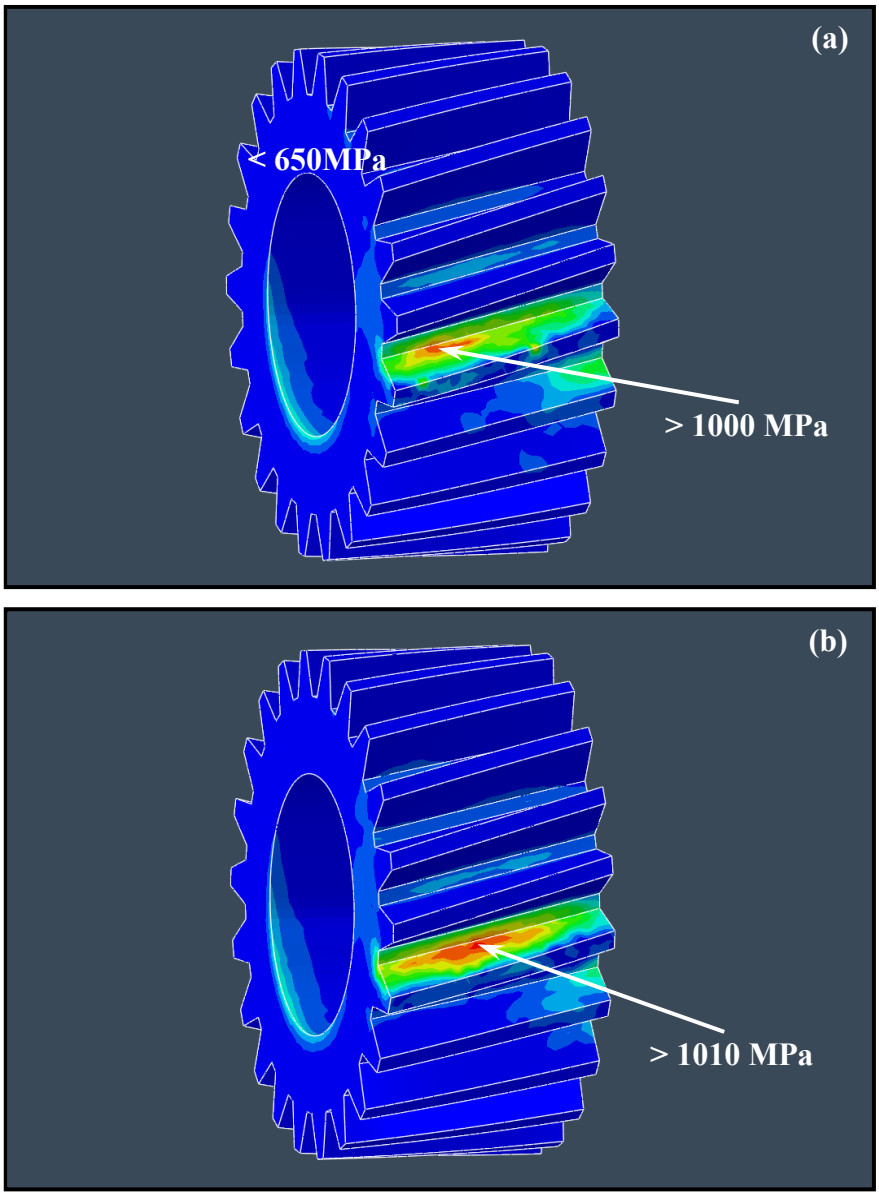

Figure 3-5 The effect of shaft misalignment (as quantified by the corresponding misalignment angle, α), at a constant level of the transferred-torque, on the spatial distribution and the magnitude of the gear-tooth maximum principal stress, at the instant when the subject gear-tooth experiences the largest value of the maximum principal stress: (a) α = 0°; (b) α = 1°; (c) α = 2°; and (d) α = 3°.

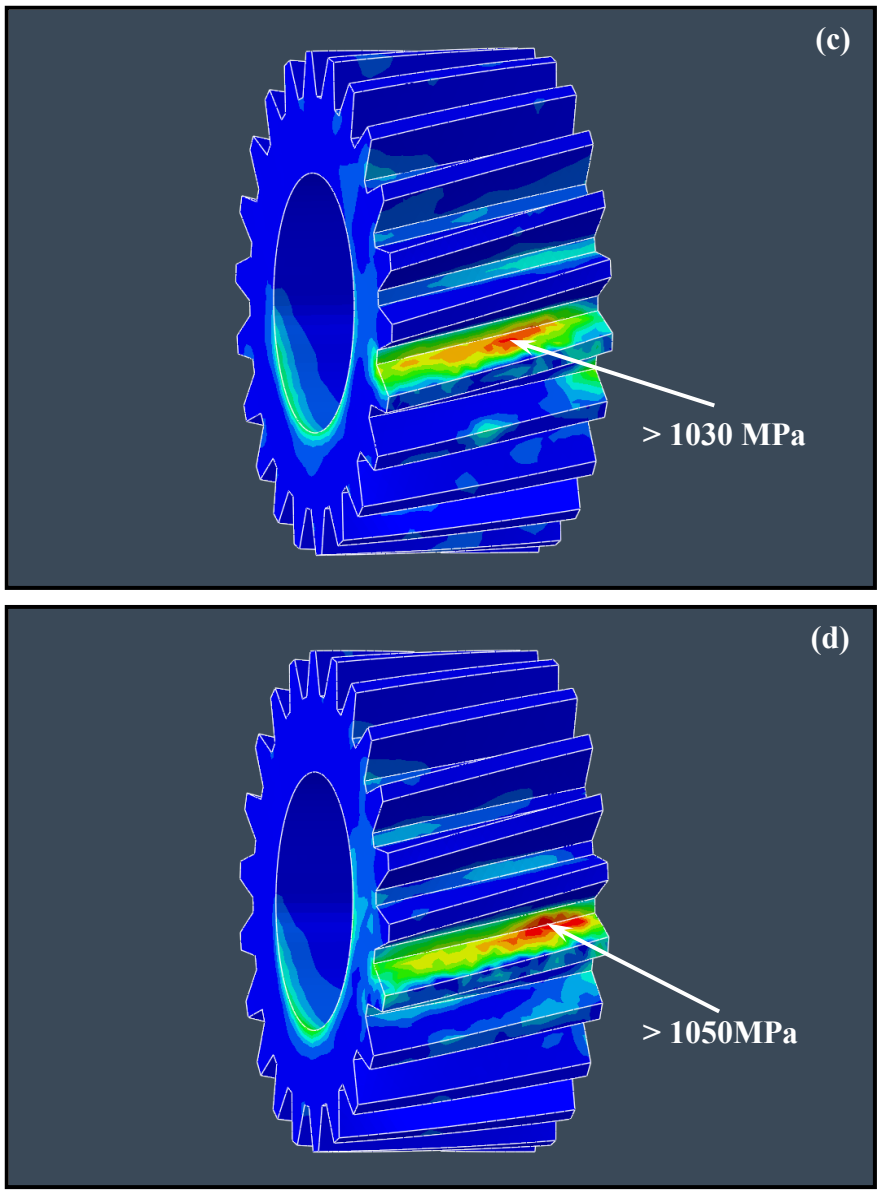

Figure.3–5. Continued

The effect of the gear-misalignment angle at a constant transferred-torque of 165 kN.m, on the largest values of the maximum principal stress and the corresponding von Mises equivalent stress is replicated, as a line graph, in Figure 3-6. It is seen that as the extent of gear misalignment increases, both the largest value of the maximum principal stress and the corresponding von Mises equivalent stress increase (at a progressively higher rate). This finding then implies, and the results of the fatigue-service-life analysis (presented below) will confirm, that as the gear-misalignment angle increases, the number of loading cycles required for fatigue-crack nucleation decrease.

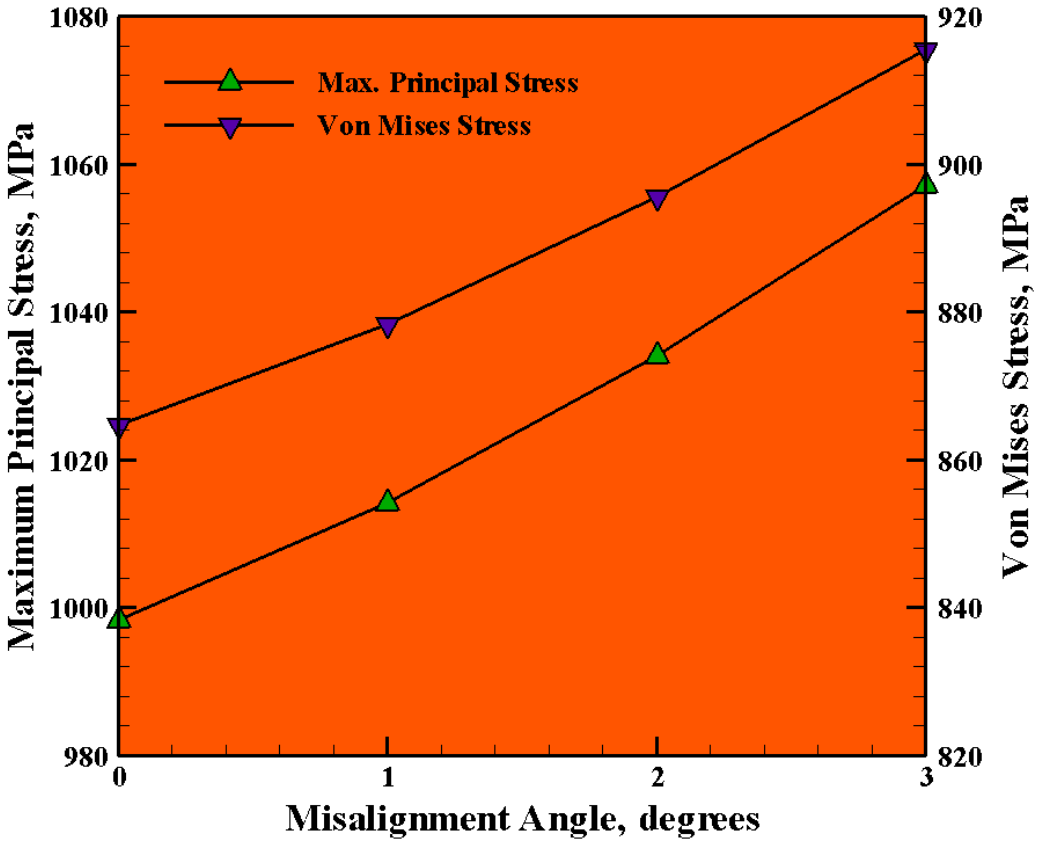

Figure 3-6 The effect of the gear-misalignment angle, at a constant level of the transferred-torque, on the largest values of the maximum principal stress.

3.5.2 Fatigue-Life Prediction

In this section, a few prototypical results are presented which exemplify the effect of transferred-torque and gear misalignment on the fatigue-life of the driven helical gear.

1) The Effect of Transferred-Torque

It should be recalled that according to the results displayed in Figure 3-4, the fatigue-controlled service-life of the driven helical gear is expected to decrease with an increase of the transferred-torque through the gear-assembly. As evidenced by the results displayed in Figure 3-6, this prediction is validated through the use of the fatigue-crack initiation and growth post-processing methodologies (described in Section 3.4). The results displayed in this figure show the effect of the transferred-torque on the number of cycles to failure (or, alternatively, on the number of years of service) of the driven helical gear, for the case of perfectly-aligned gears.

2) The Effect of Gear Misalignment

The effect of the misalignment angle on the total fatigue-controlled service-life of the driven helical gear, under a constant transferred-torque condition, is depicted in Figure 3-8. It is seen that as predicted by the results shown in Figure 3-7, gear misalignment can severely shorten the service-life of the gear (the driven helical gear in the intermediate stage of the wind-turbine gearbox, in the present case).

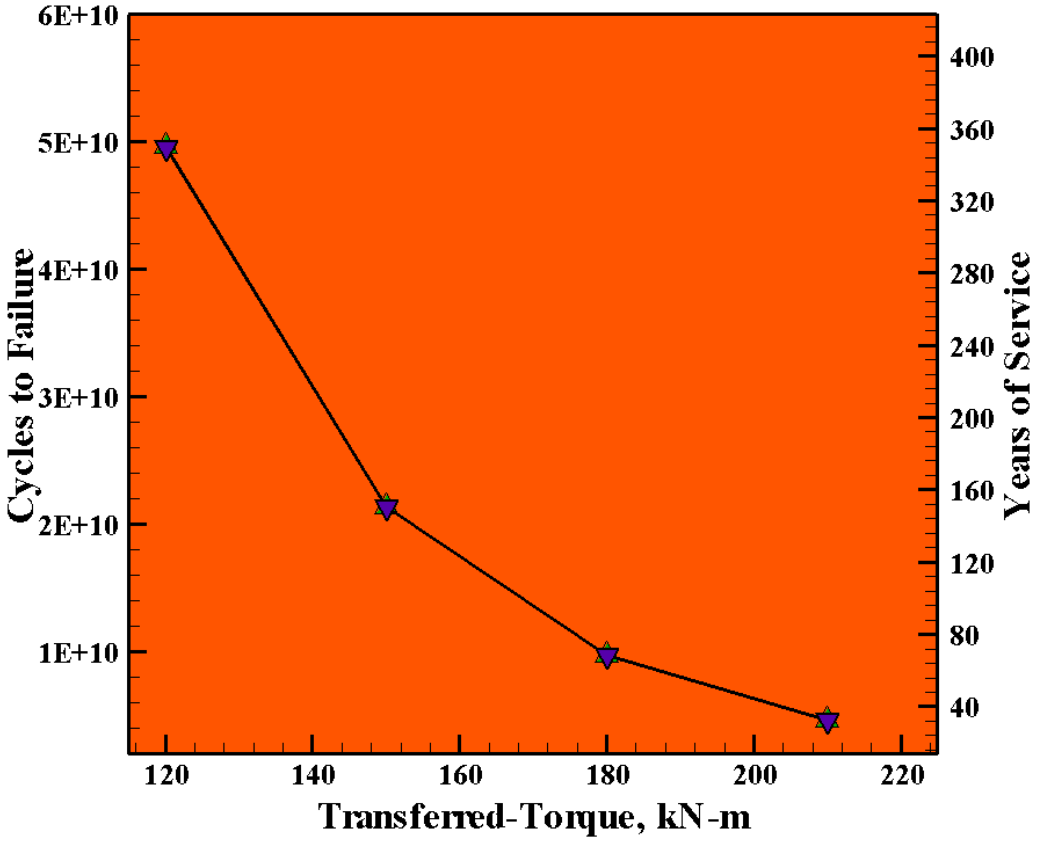

Figure 3-7 The effect of the transferred-torque on the total service-life of the driven helical gear, for the case of perfectly aligned gears.

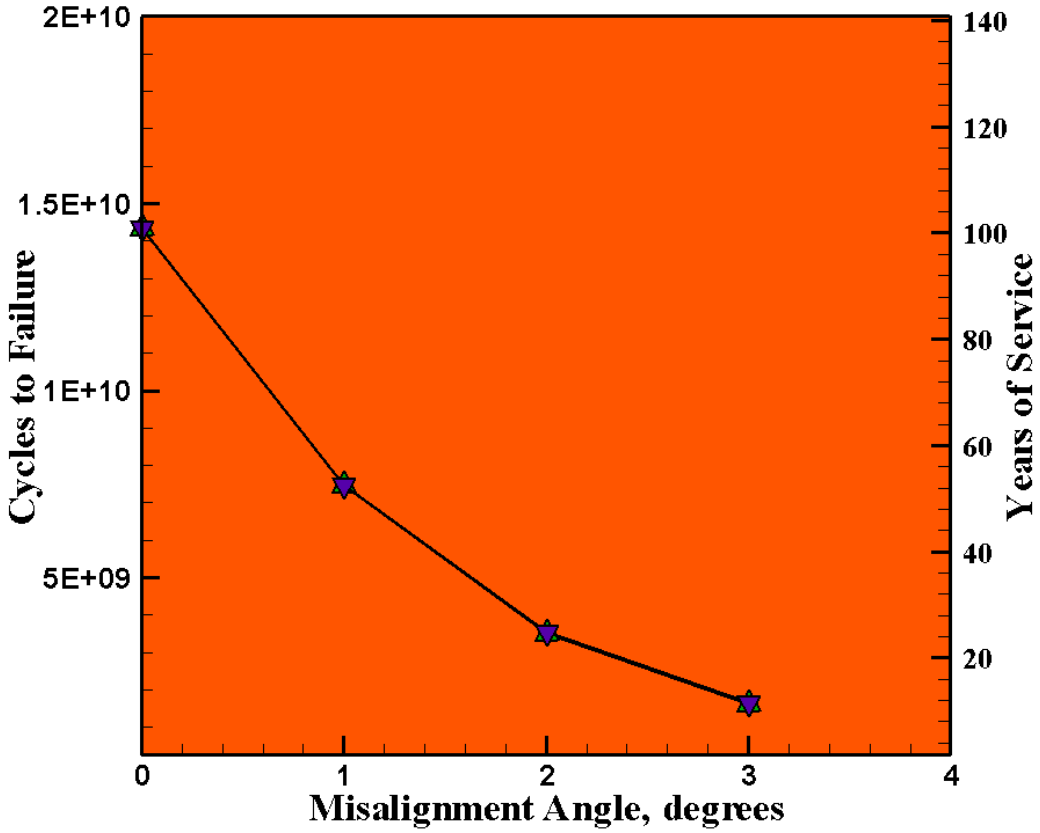

Figure 3-8 The effect of the misalignment angle on the total fatigue-controlled service-life of the driven helical gear, under a constant transferred-torque condition.

3.6. Summary and Conclusions

This portion of the work demonstrates the use of finite element analysis in modeling and investigating the root cause of one of the gear failure modes under a variety of normal operating and extreme wind-loading conditions. The main conclusions that can be drawn are as follows:

1. In the present work, it is argued that the purely empirical efforts aimed at identifying shortcomings in the current design of the gearboxes should be complemented with the appropriate advanced computational methods and engineering analyses. Such methods/analyses can help shorten the time of development of new gearbox designs and help with the identification of the root causes of failure of this wind-turbine subsystem.

2. Specifically, in the present work, a particular mode of gearbox failure (i.e. gear-tooth bending fatigue) is modeled by combining advanced finite-element structural/stress analysis with the computational procedures developed for prediction of fatigue-crack initiation and growth processes (and ultimate failure).

3. While the methodology and the procedures developed and used are of a preliminary character, the results obtained clearly revealed the effect of the service-loading conditions (as quantified by the transferred-torque and the gear-misalignment) on the fatigue-service-life of the gearbox.

3.7. References

1. ABAQUS Version 6.10EF, ***User Documentation***, Dassault Systemes, 2011.

2. P. J. L. Fernandes, "***Tooth Bending Fatigue Failures in Gears***," Engineering Failure Analysis, 3, 219–225, 1996.

3. P. J. L. Fernandes, and C. McDuling, "***Surface Contact Fatigue Failures in Gears***," Engineering Failure Analysis, 4, 99–107, 1997.

4. M. Grujicic, B. Pandurangan, U. Zecevic, K. L. Koudela and B. A. Cheeseman, "***Ballistic Performance of Alumina/S-2 Glass-Reinforced Polymer-Matrix Composite Hybrid Lightweight Armor Against Armor Piercing (AP) and Non-AP Projectiles***," Multidiscipline Modeling in Materials and Structures, 3, 287–312, 2007.

5. M. Grujicic, G. Arakere, V. Sellappan, A. Vallejo and M. Ozen, "***Structural-response Analysis, Fatigue-life Prediction and Material Selection for 1MW Horizontal-axis Wind-Turbine Blades***," Journal of Materials Engineering and Performance, 19, 780–801, 2010.

6. M. Grujicic, G. Arakere, B. Pandurangan, V. Sellappan, A. Vallejo and M. Ozen, "***Multidisciplinary Optimization for Fiber-Glass Reinforced Epoxy-Matrix Composite 5MW Horizontal-axis Wind-turbine Blades***," Journal of Materials Engineering and Performance, 19, 1116–1127, 2010.

7. M. Grujicic, G. Arakere, A. Hariharan, B. Pandurangan, "***Two-level Weld-Material Homogenization for Efficient Computational Analysis of Welded Structure Blast Survivability***," Journal of Materials Engineering and Performance 21 (2012a): 786–796.

8. M. Grujicic, A. Arakere, B. Pandurangan, C-.F. Yen and B. A. Cheeseman, "***Process Modeling of Ti-6Al-4V Linear Friction Welding (LFW)***," Journal of Materials Engineering and Performance, 21 (2012b), 2011–2023.

9. M. Grujicic, B. Pandurangan, C-F.Yen, B. A. Cheeseman, "***Modifications in the AA5083 Johnson-Cook Material Model for Use in Friction Stir Welding Computational Analyses***," Journal of Materials Engineering and Performance, 21 (2012c): 2207–2217.

10. M. Grujicic, S. Ramaswami, J. S. Snipes, R. Yavari, A. Arakere, C-.F. Yen, B. A. Cheeseman, "***Computational Modeling of Microstructure Evolution in AISI1005 Steel during Gas Metal Arc Butt Welding***," Journal of Materials Engineering and Performance 22 (2013a): 1209–1222.

11. M. Grujicic, A. Arakere, S. Ramaswami, J. S. Snipes, R. Yavari, C-.F. Yen, B. A. Cheeseman, "***Gas Metal Arc Welding Process Modeling and Prediction of Weld Microstructure in MIL A46100 Armor-Grade Martensitic Steel***," Journal of Materials Engineering and Performance 22 (2013b): 1541–1557.

12. M Grujicic, R. Galgalikar, J. S. Snipes, R Yavari, and S. Ramaswami, "***Multi-Physics Modeling of the Fabrication and Dynamic Performance of All-Metal Auxetic-Hexagonal Sandwich-Structures***." Materials and Design 51 (2013c): 113–130.

13. J. Kramberger, M. Šraml, S. Glodež, J. Flašker, I. Potrč, "***Computational model for the analysis of bending fatigue in gears***," Computers and Structures, 82, 2261–2269, 2004.

14. W.D. Musial, S. Butterfield, and B. McNiff, "***Improving Wind Turbine Gearbox Reliability***," European Wind Energy Conference, Milan, Italy, 2007.

CHAPTER 4: HORIZONTAL–AXIS WIND–TURBINE: PRELIMINARY BEARING KINEMATICS AND KINETICS

4.1. Abstract

To make wind energy economical, wind-turbines are required to operate, with only regular maintenance, for at least twenty years. However, some key wind-turbine components (especially the gear-box) often require significant repair or replacement after only three to five years in service. Consequently, the wind-energy cost and the cost of ownership of the wind turbine are increased. To bring the wind-energy cost down, durability and reliability of gear-boxes have to be substantially improved. These goals are currently being pursued using mainly laboratory and field-test experimental approaches. While these empirical approaches are valuable in identifying shortcomings in the current design of the gear-boxes and the main phenomena and processes responsible for the premature failure of wind-turbine gear-boxes, advanced computational engineering methods and tools can not only complement these approaches but also provide additional insight into the problem at hand (and do so in a relatively short time). Premature failure of wind-turbine gearboxes is, in the majority of cases, linked to the damage (and, often, failure) of their bearings. Frequently, when the gearbox failure appears to be caused by the failure of its gears, the origin of this failure can be traced back to the damage/failure of the bearings. In this section, an attempt is made to construct a multi-body dynamics (MBD) computational model which can be used to analyze the basic kinematics and kinetics of a prototypical wind-turbine gearbox bearing. The results generated by this model will be used in a future computational analysis to more closely examine the underlying physics of gear-box bearing premature failure.

4.2. Introduction

The present work addresses the problem of roller-bearing premature failure in, and the long-term reliability of, gear-boxes in wind (energy-harvesting) turbines. Consequently, the concepts most relevant to this work are: (a) wind-energy harvesting; (b) wind-turbine gear-box reliability; and (c) premature failure of wind-turbine gear-box roller-bearings.

4.2.1 Wind Energy Harvesting

Fossil-fuel reserve depletion, stricter environmental regulations and the world's ever-growing energy needs have led to various renewable energy sources being deployed/utilized. Wind energy is one of the most promising and the fastest-growing installed renewable-energy production technologies.

A wind-turbine is essentially a converter of wind energy into electrical energy. This energy conversion is based on the principle of having the wind drive a rotor, thereby transferring power to an electrical generator. To attain greater structural stability of the rotor and high aerodynamic efficiency, the rotor is usually constructed as a set of three aerodynamically-shaped blades. The blades are (typically) attached to a horizontal hub (which is connected to the rotor of the electrical generator, via a gear-box/drive-train system, housed within the nacelle). The assembly is placed on a tower and the resulting energy converter is referred to as the Horizontal Axis Wind Turbine (HAWT).

To reduce the energy-production cost, commercial wind turbines have grown considerably in size over the last 30 years. As the hub-height/rotor-radius increases, the average wind-speed/wind-energy-captured increases. Consequently, fewer wind-turbines are required to generate the same energy, which in turn leads to a reduced cost of operation. As the rotor grows larger, the structural performance, durability and dynamic-stability requirements become more challenging, and it is not clear what ultimate rotor diameter can be attained with the present design, material and manufacturing technologies.

The blades and gear-box are perhaps the most critical components/subsystems in current designs of wind turbines. In our recent work [1, 2, 3], the problem of structural integrity and

durability was investigated. The present work, on the other hand, focuses on issues related to the performance, reliability and failure-modes of gear-box components.

4.2.2 Wind Turbine Gear-box Reliability

Wind-turbine gear-box failure remains a major problem to the wind-energy industry [4]. The root causes of failure in earlier designs were associated with problems related to: (a) fundamental design errors; (b) manufacturing deficiencies; and (c) under-estimated operating loads. While these problems have been mainly eliminated by developing and applying design standards, and establishing good manufacturing practices [5], gear-boxes still generally fail to achieve their design-life goal of twenty years. High failure rates, long downtimes and the high repair cost have contributed to: (a) increased wind-energy cost; (b) increased sales price of wind-turbines due to higher warranty premiums; and (c) a higher cost of ownership due to the need for funds to cover repair after warranty expiration. To make wind-energy more viable, its cost must be brought back to a decreasing trend, which entails a significant increase in long-term gear-box reliability.

The current understanding of the basic features and processes/mechanisms of gear-box failure can be summarized as follows [4]: (a) failure is not strongly related to differences in design, and generally cannot be attributed to poor workmanship; (b) failure is often caused by excessive and unexpected (e.g. misalignment) loading conditions; (c) failure usually appears to initiate in excessively and unfavorably loaded bearings. The resulting damage-induced loading conditions and the propagation of the bearing-wear debris to the gears cause tooth wear and gear misalignment (resulting in the final failure of the gear-box); and (d) the essential features and mechanisms of damage and failure appear not to change with size of the wind-turbine.

A schematic of a prototypical wind-turbine gear-box is shown in Figure 4-1. The low-speed stage is a planetary configuration with either spur or helical gears. The planetary-gear carrier is driven by the wind-turbine rotor, the ring gear is stationary/reactionary, while the sun

pinion shaft drives the intermediate-speed stage, and, in turn, the high-speed stage (connected to the rotor of the electric generator). Typically, the latter two stages consist of helical gears. Predominantly, failure initiation is observed in planet bearings, intermediate-shaft bearings and high-speed-shaft bearings.

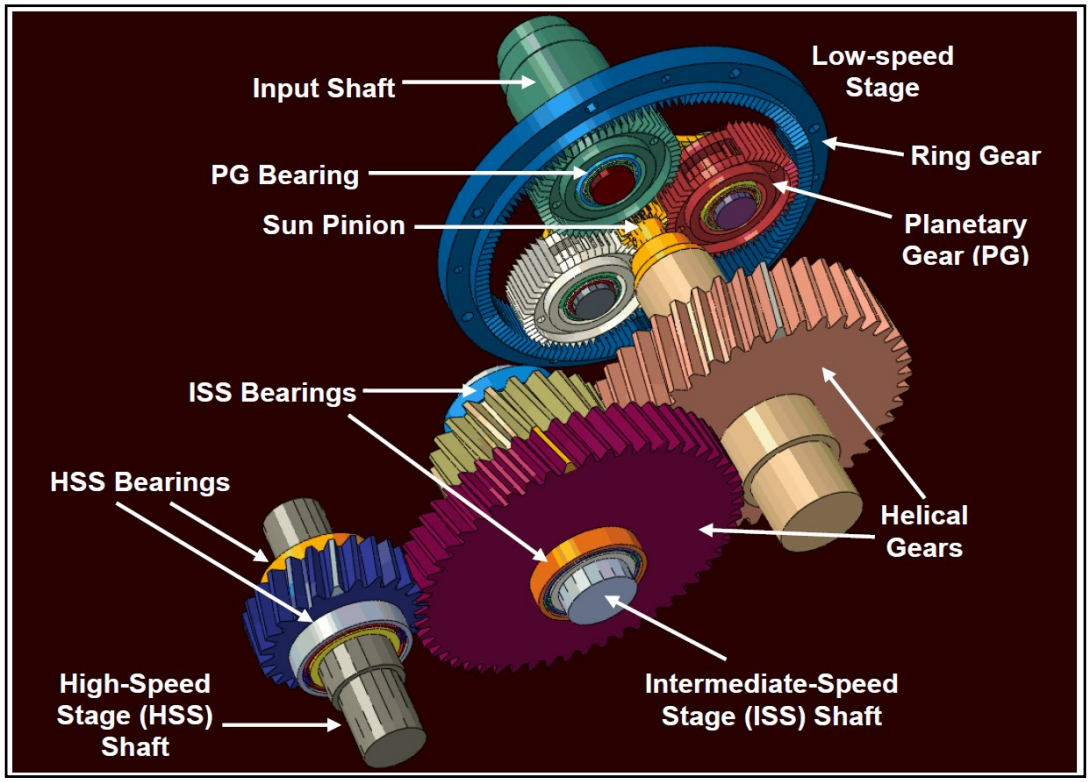

Figure 4-1 Schematic of a prototypical wind-turbine gear-box. The major components and sub-systems are identified. Failure typically occurs within the (planet, intermediate-speed shaft and high-speed shaft) roller-bearings.

4.2.3 Premature Failure of Wind-Turbine Gear-box Roller-Bearings

Provided roller-bearings are: (a) properly maintained and lubricated; and (b) not subjected to excessive and unintended loading conditions, their service-life is controlled by the material high-cycle fatigue (typically within the bearing races/rings), commonly referred to as roller-bearing contact fatigue (RCF) failure. The in-service cycling stresses arise from the repeated exposure of the ring material to ring/roller-element non-conformal contact stresses. Under well-lubricated/clean-lubricant conditions, RCF is typically initiated by subsurface-crack nucleation (in regions associated with critical combinations of the largest shear stress and the presence of high-potency microstructural defects). During subsequent repeated loading, cracks tend to advance towards the inner surfaces of the raceways, leading to spall/fragment formation. Under proper lubrication and normal loading conditions, the roller-bearing service-life is generally well-predicted by standard bearing-life calculation methods [6, 7].

Roller-bearings in wind-turbine gear-boxes tend to fail much earlier than expected. In addition, the mechanism and the appearance of roller-bearing prototypical premature-failure seem different from the classic RCF failure. In the latter mode, the sub-surface region contains dark and white bands as well as chevron-shape cracks. (The visual appearance of RCF failure is described in detail in [6]) In premature-failure, the damaged region acquires a characteristic "White Etching Crack" appearance, and is initially localized at or slightly beneath the contact surfaces. In addition to the chevron-shaped cracks, so-called butterfly white-etching cracks are also often observed in RCF failure. These cracks are formed at greater depths and are normally associated with excessive loading. By contrast, white-etch cracking in premature-failure is believed to be a surface or near-surface phenomenon [8]. Specifically, it is believed that a combination of disturbed bearing kinematics, unfavorable loading and inadequate lubrication can

lead to local tensile-stress concentrations, at the root of surface asperities and/or at inclusion/matrix interfaces near the surface. For sufficiently high stress concentrations and the number of loading cycles, surface and/or subsurface cracks can nucleate. Due to proximity of the contact surfaces, subsurface cracks can readily extend to these surfaces (becoming surface cracks).

Once formed, cracks are infiltrated by the lubricant which contains various additives and possibly contaminants like water. Passage of the rolling elements over the damaged area can have hydrodynamic effects, leading to crack spreading and branching. Newly formed "clean-metal" crack faces readily react with the lubricant, causing the formation of a chemically altered fracture-toughness-inferior region at the crack tip. These changes, in turn, lead to a transition from a purely mechanical-fatigue-cracking regime to a corrosion-assisted fatigue-cracking regime. The same reactions produce hydrogen, which diffuses into the surrounding crack-tip region, primarily along the grain boundaries. This (embrittling) process reduces grain-boundary cohesion and promotes inter-granular cracking. By contrast, in RCF failure, cracking is predominantly trans-granular and tends to spread along the bands associated with the maximum shear stresses and strains.

The defining characteristics of the roller-bearing premature-failure mode are:

(a) it preferentially occurs at the inner races/rings;

(b) the cracks nucleate predominantly at the race surfaces;

(c) the final damage is almost always associated with heavy spallation of the inner-ring raceways;

(d) roller-bearing type/design does not appear to have a first-order effect on the frequency and intensity of occurrence of premature-failure;

(e) often, surface-crack initiation is associated with improper lubrication or contamination/degradation of the lubricant, or some unfavorable tribo-chemical surface phenomena and processes. These conditions generally lead to the changes in the contact surface referred to as “surface distress,” which act as a precursor to the surface-crack formation, and include: (i) discoloration and dulling of the surface; and (ii) the presence of micro-spalls, micro-cracks or micro-pits; and

(f) subsequent spreading and branching of the surface cracks, ultimately resulting in spallation, appears to be associated with the operation of corrosion-cracking mechanisms [8] that are related to hydrogen and lubricant-breakdown products diffusing into the crack-tip region of the raceway material. As a result, crack-propagation failure is quite fast compared to classical RCF failure, which takes place mainly in the subsurface region (which is not accessible to these corrosion agents).

4.2.4 Main Objectives

The main objective of the work presented in this section is the construction of a multi-body dynamics (MBD) computational model for a prototypical wind-turbine gear-box roller bearing. For convenience, and to help facilitate a future computational investigation of the wind-turbine gear-box roller-bearing premature-failure root cause, the model is constructed within SIMPACK, a commercial general-purpose MBD code [9]. To model contact interactions between rolling elements, cage, inner race and the outer race (all modeled as rigid bodies), several user-defined force elements have to be introduced. These force elements are defined within a user subroutine (named uforce20) which is subsequently linked with the SIMPACK solver. The results to be obtained will be used in future computational investigation of the roller-bearing premature-failure underlying physics.

4.3. Multibody Dynamics of a Gearbox Roller Bearing

4.3.1 Problem Description

The main problem analyzed in this portion of the work involves multi-body-dynamics analysis of a prototypical wind-turbine gear-box roller-bearing. As will be discussed in greater detail below, the roller-bearing MBD model consists of an inner race, an outer race, twelve cylindrical rolling elements and a cage. The MBD analysis is carried out under the following conditions: (a) all six (three translational and three rotational) degrees of freedom (DOFs) for the outer race are fully constrained; (b) except for the rotational DOF about the axis of the roller-bearing (which is aligned in y-direction and subjected to a constant angular velocity) all the remaining DOFs of the inner race are constrained; (c) y-translational, x- and z-rotational DOFs of the rolling elements are constrained. In other words, each rolling element is free to rotate about its axis (aligned in y-direction) and to translate in the (x-z) plane of the roller-bearing (by revolving about the axis of the roller bearing); and (d) except for the rotational DOF about the axis of the roller-bearing (which is left unconstrained) all the remaining DOFs of the cage are constrained. To model contact forces between the rolling elements and the inner and outer races, the analysis is initiated by prescribing the values for the penetrations of the inner and outer races by the rolling elements. The initial values of the rolling-elements/inner-race and rolling-elements/outer-race are kept the same and their values varied between different analyses in order to examine the effect of rolling-elements/races contact forces on the rolling-elements skidding behavior. As far as the contact forces between the rolling elements and the cage are concerned, they are modeled in a similar way using linear-spring type of contact elements. For a given rolling element, a single force element is used to model its potential interaction with both leading and the trailing bridges

of the respective cage pocket. The rolling-element/cage force elements are also implemented in uforce20 subroutine and linked with the SIMPACK solver.

4.3.2 SIMPACK Computer Program

SIMPACK [9] is a highly-detailed general-purpose transient nonlinear-dynamics modeling and simulation computer program, capable of analyzing the response of controlled, articulated multi-body mechanical systems when subjected to various (regular or irregular) external and internal effects/excitations. The program contains an extensive library of primitive rigid and flexible bodies, kinematic joints, constraints, and force- and control-elements which can be combined in various ways in order to assemble complex-system models at a level of detail considered necessary in the problem at hand. SIMPACK comprises three main modules: (a) a pre-processor; (b) a main processor, and (c) a post-processor. Within the pre-processor, topological and parametric properties of the model are defined within an interactive environment. The main processor uses the information provided by the pre-processor to assemble the governing kinematics and dynamics equations. In addition, the processor may take advantage of one or more user-interface subroutines which allow the incorporation of highly nonlinear system properties (e.g. contact forces between the races/cage and the rolling elements) and, thus, can yield quite representative/realistic models.

4.3.3 Roller-Bearing MBD Model

Rigid Bodies

The roller-bearing MBD model used in this portion of the work comprises only rigid bodies. Specifically, the model includes: (a) an inner race; (b) an outer race; (c) twelve cylindrical rolling elements; and (d) a cage/retainer. A CAD model of the roller-bearing analyzed in this portion of the work is depicted and labeled in Figure 4-2. For each of the rigid bodies displayed in this figure, the MBD analysis requires specification of its center of mass, mass, and the moment of inertia (a second-order tensor). These characteristics of the rigid bodies present in the MBD model are summarized in Table 4-1.

Kinematic Constraints

As discussed in Section 4.3.1, rigid bodies present in the MBD model are subjected to different kinematic constraints. These constraints were defined within the MBD model using the appropriate "*joints*". For example, full kinematic constraints of the outer race were achieved by placing a zero-degree joint between its reference frame and the global reference frame of the surrounding. A complete definition of a (kinematic) joint requires specification of the joint name (i.e. identification label), joint type (each joint type is associated with a set of active and constrained DOFs), a frame attached to the "*master body*" and a frame attached to the "*slave body*". These details for all the joints used in the present roller-bearing MBD model are summarized in Table 4-2. In addition to the kinematic joints listed in Table 4-2, a kinematic constraint named ("*Massless Link*") is used to ensure that revolving of the rolling elements takes place over a circular path with the center of the circular path being coincident with the roller-bearing axis. In other words, the use of the massless link constrained displacement of the rolling elements in the radial direction with respect to the axis of the roller-bearing.

Contact interactions between rolling elements and inner-race, outer-race, and cage are represented within the MBD model using the appropriate force elements. Two distinct types of force elements are used: (a) one to define the contact interactions between the rolling elements and inner-race/outer-race; (b) and the other to define the contact interactions between the rolling elements and cage. In the remainder of this sub-section, a brief description is provided of the equations governing the behavior of these two types of force elements.

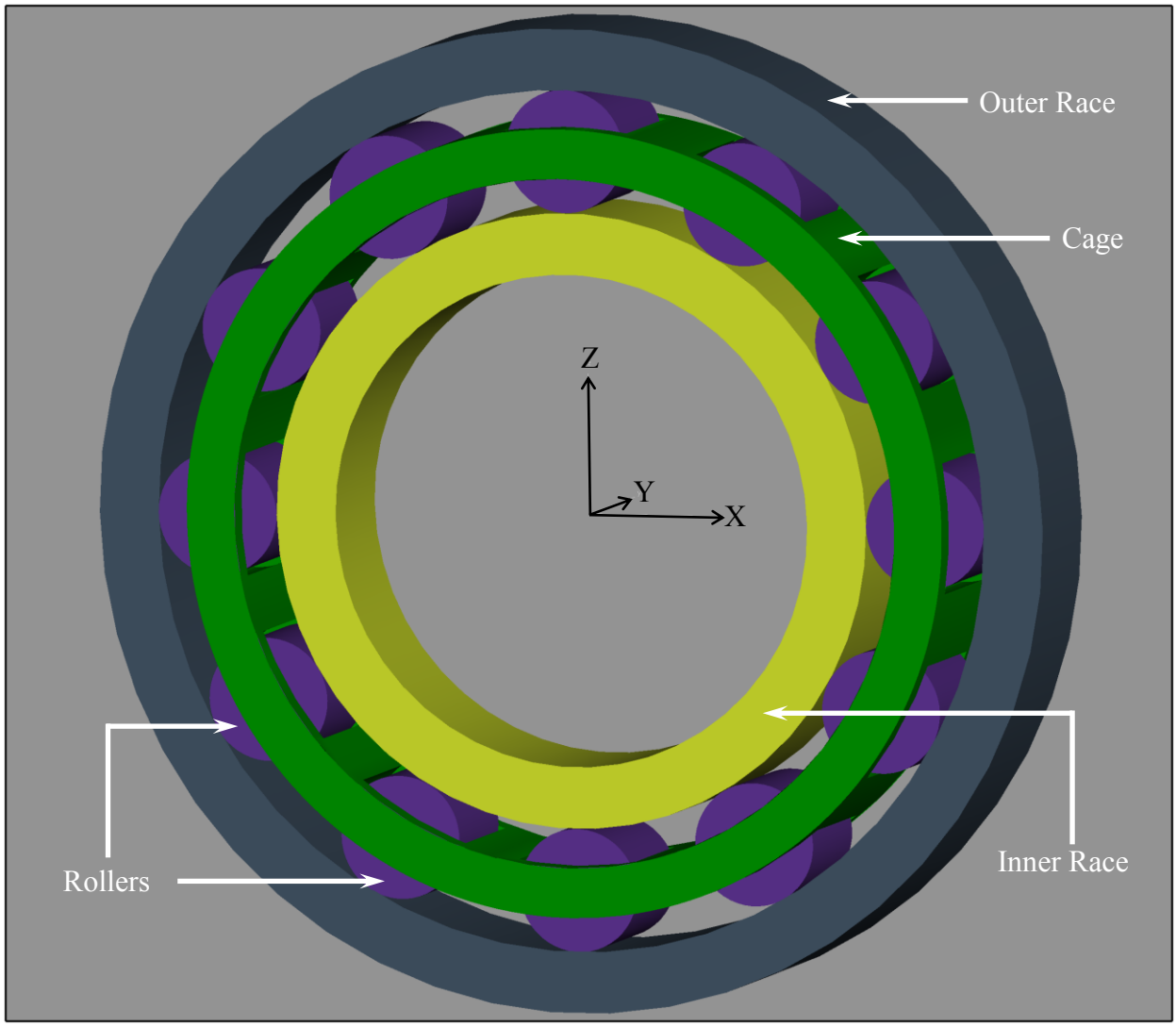

Figure 4-2 A labeled CAD model of the roller bearing MBD model analyzed.

Component Name	Mass [kg]	Principal Moments of Inertia* [kg-m^2]	x, y, z coordinates of Center of Gravity (C.G)** [m]
Inner Race	442.74	(46.74, 90.523, 46.74)	(0, 0, 0)
Outer Race	737.90	(210.37, 415.82, 210.37)	(0, 0, 0)
Roller 1	49.20	(28.66×10^{-2}, 24.53×10^{-2}, 28.66×10^{-2})	(0, 0, 0.6)
Roller 2	49.20	(28.66×10^{-2}, 24.53×10^{-2}, 28.66×10^{-2})	(0.3, 0, 0.52)
Roller 3	49.20	(28.66×10^{-2}, 24.53×10^{-2}, 28.66×10^{-2})	(0.52, 0, 0.3)
Roller 4	49.20	(28.66×10^{-2}, 24.53×10^{-2}, 28.66×10^{-2})	(0.6, 0, 0)
Roller 5	49.20	(28.66×10^{-2}, 24.53×10^{-2}, 28.66×10^{-2})	(0.52, 0, -0.3)
Roller 6	49.20	(28.66×10^{-2}, 24.53×10^{-2}, 28.66×10^{-2})	(0.3, 0, -0.52)
Roller 7	49.20	(28.66×10^{-2}, 24.53×10^{-2}, 28.66×10^{-2})	(0, 0, -0.6)
Roller 8	49.20	(28.66×10^{-2}, 24.53×10^{-2}, 28.66×10^{-2})	(-0.3, 0, -0.52)
Roller 9	49.20	(28.66×10^{-2}, 24.53×10^{-2}, 28.66×10^{-2})	(-0.52, 0, -0.3)
Roller 10	49.20	(28.66×10^{-2}, 24.53×10^{-2}, 28.66×10^{-2})	(-0.6, 0, 0)
Roller 11	49.20	(28.66×10^{-2}, 24.53×10^{-2}, 28.66×10^{-2})	(-0.52, 0, 0.3)
Roller 12	49.20	(28.66×10^{-2}, 24.53×10^{-2}, 28.66×10^{-2})	(-0.3, 0, 0.52)
Cage	195.30	(37.53, 70.93, 37.52)	(0, 0, 0)

* about the component center of gravity (C.G.)

** at time t = 0, relative to the roller-bearing center (0,0,0)

Table 4-1 Specifications of multi-body model of cylindrical roller bearing

Joint Name	Master Body	Slave Body	Joint Type	Active DOFs
$J_Inner_Race	Global Reference	Inner Race	Single Axis Constant Velocity	None
$J_Outer_Ring	Global Reference	Outer Race	Zero DOF	None
$J_RollerX*	Global Reference	RollerX*	User Defined Joint	x , z , β
$J_Cage	Global Reference	Cage	Revolute Joint be	β

* X indicates the number of roller (1 – 12)

Table 4-2 Types of joints used in the MBS model

Rolling-elements/bearing-races contact interactions

Two types of forces (i.e. normal and tangential), are considered to result from the contact interactions between the rolling elements and the inner/outer races. The tangential force which acts at the contact interface between the rolling elements and the races can be represented as a superposition of a collinear/equal magnitude force (acting on the rolling-element center) and a torque (with a magnitude equal to the product of the tangential force and rolling-element radius) about the axis of the rolling element. The latter force is responsible for the revolving motion while the torque causes the spinning motion of the rolling elements.

The normal contact-interaction force between the rolling-elements and the races is modeled using a "*Hertzian-type*" spring with the following constitutive relation:

$$F_n = K_n \delta^{3/2} \tag{4–1}$$

where δ is the extent of rolling-element/race penetration. For example, in the case of the rolling-elements/inner-race interaction δ is defined as the difference of the sum of the rolling-element and inner-race radii and the rolling-element/inner-race center-to-center distance. It should be noted that Eq. (4–1) is strictly valid for the case of sphere-shaped rolling elements. For the case of cylindrical-shaped rolling elements, the power should be changed to 3/2 to 10/9. The normal-spring constant, K_n is defined in terms of the rolling-elements radius, R_{roller}, inner-race radius, $R_{in-race}$, outer-race radius, $R_{out-race}$, and the elastic modulus E and the Poisson's ratio ν of the materials used in the construction of rolling elements, inner race and outer race. For the case of sphere-shaped rolling elements, this expression takes the following respective forms at the rolling-element/inner-race and rolling-element/outer-race interfaces:

$$K_n^{inner} = \frac{2^{2.5}\left(\frac{2}{R_{roller}} + \frac{1}{R_{in-race}}\right)^{-0.5}\left(\delta^*\right)^{-1.5}}{3\left(\frac{1-\nu_{roller}^2}{E_{roller}} + \frac{1-\nu_{in-race}^2}{E_{in-race}}\right)} \tag{4–2}$$

$$K_n^{outer} = \frac{2^{2.5}\left(\frac{2}{R_{roller}} + \frac{1}{R_{out-race}}\right)^{-0.5}\left(\delta^*\right)^{-1.5}}{3\left(\frac{1-\nu_{roller}^2}{E_{roller}} + \frac{1-\nu_{out-race}^2}{E_{out-race}}\right)} \tag{4–3}$$

where the subscripts $roller, in-race, out-race$ are self-explanatory, and dimensionless parameter δ^* is defined using tabular representation given in Table 4-3. In Table 4-3, the quantity $F(\rho)$ is defined as:

$$F(\rho) = \frac{\left(\frac{1}{R_{race}}\right)}{\left(\frac{2}{R_{roller}} + \frac{1}{R_{race}}\right)} \tag{4–4}$$

where R_{race} is replaced with $R_{in-race}$ or $R_{out-race}$ as needed.

$F(\rho)$	δ^*
0	1
0.1075	0.997
0.3204	0.9761
0.4795	0.9429
0.5916	0.9077
0.6716	0.8733
0.7332	0.8394
0.7948	0.7961
0.83595	0.7602
0.87366	0.7169
0.90999	0.6636
0.93657	0.6112
0.95738	0.5551
0.97290	0.4960
0.983797	0.4352
0.990902	0.3745
0.995112	0.3176
0.997300	0.2705
0.9981847	0.2427
0.9989156	0.2106
0.9994785	0.17167
0.9998527	0.11995
1	0

Table 4-3 Relationship between the dimensionless contact parameters [11]

The tangential contact-interaction force between the rolling-elements and the races is assumed to be defined by the Coulomb law as:

$$F_t = \mu F_n \tag{4–5}$$

where μ is the friction coefficient. Under the elastohydrodynamic conditions (associated with the presence of a lubricant within the bearing element), μ is generally considered to be a function of the rolling-element/race slip velocity, V_s. The μ vs V_s functional relationship used in the present work was taken from [10] and is depicted in Figure 4-3. This functional relationship was used in its tabulated form in the present work. The slip velocity between a rolling-element and the inner-race, V_{s-in} is defined in terms of the rolling-element revolving velocity, V_{r-rev}, the rolling-element rotational velocity, ω_{r-rot} and the inner-race rotational velocity, $\omega_{in-race}$ as:

$$V_{s-in} = \omega_{in-race} R_{in-race} - V_{r-rev} + \omega_{r-rot} R_{roller} \tag{4–6}$$

V_{r-rev} is obtained using the following two-step procedure: (a) first, a component of the rolling-element velocity vector (located within the x-z plane) in the (instantaneous) tangent direction is determined; (b) then, this velocity component is multiplied by a ratio of the $R_{in-race}$ and rolling-element/inner-race center-to-center distance. An analogous procedure is used to determine the slip velocity at the rolling-element/outer-race contact interface, V_{s-out} and to establish its effect on the associated friction coefficient (and, in turn, the tangential force).

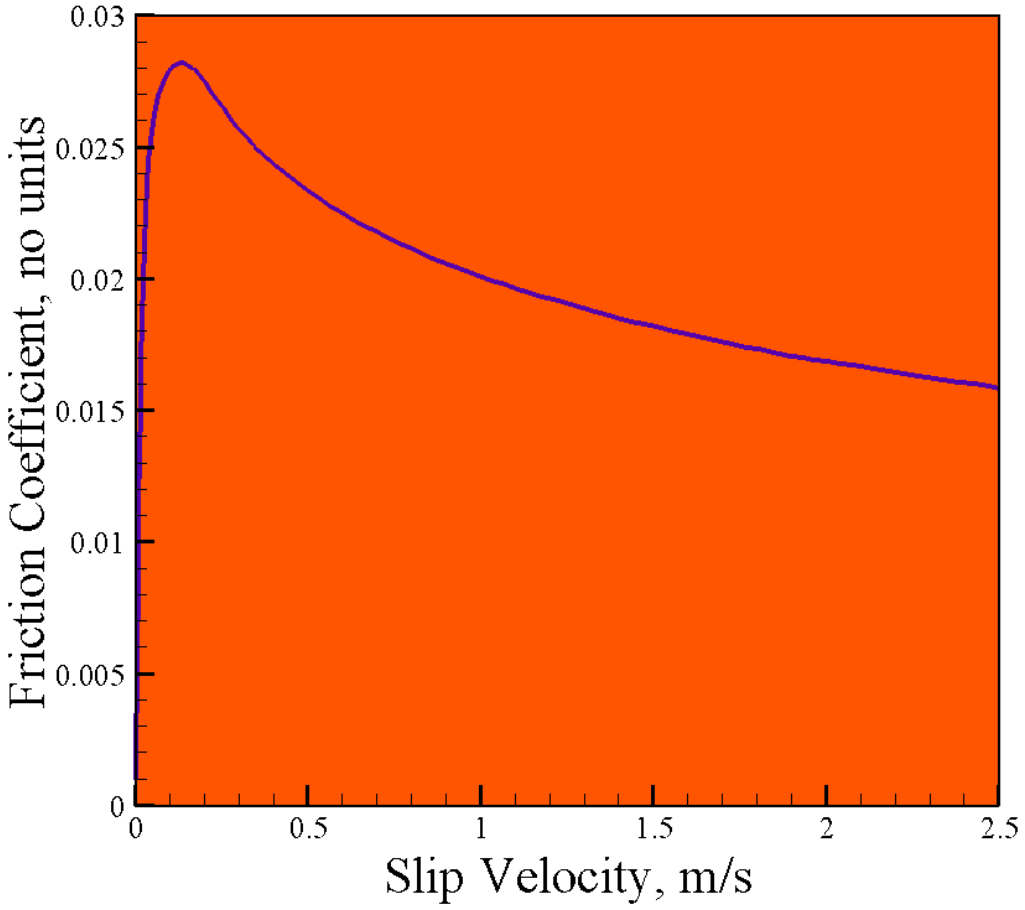

Figure 4-3 The effect of rolling-element/race slip velocity on the coefficient of friction under elastohydrodynamic conditions [10].

The contact interactions between the rolling elements and the races are implemented as user-defined force elements within the uforce20 SIMPACK subroutine. The kinematic relationships between a rolling element and a contacting race is established through the use of a "*from*" marker (a coordinate system attached to the center of the rolling element) and the "*to*" marker (a coordinate system attached to the center of the race). Per request made by the user, SIMPACK will provide the requested kinematic parameters within the two markers. For example, the user may request the position vector of the from-marker origin relative to the to-marker origin expressed in the global reference frame. This information can be used to compute δ and, in turn, F_n. SIMPACK expects the user to return to it the values of the interaction-force and interaction-torque components all expressed in the reference-frame of the body associated with the from-marker (a rolling-element, in the present case). Due to the regular-cylindrical geometry of the rolling elements, their reference-frame is coincident with their from-marker. Thus, the interaction forces and torques have to be returned in the from-marker coordinate system. It should be noted that F_n and F_t act respectively in a direction normal to and in a direction tangential to the rolling-element/race contact patch. To compute and superpose the components of F_n and F_t along the axes of the from-marker, the following three-step procedure is used: (a) first, the knowledge of the position vector of the from-marker origin relative to the to-marker origin expressed in the global frame is first used to determine the directional cosines of the vectors associated with F_n and F_t; (b) this knowledge is used to project F_n and F_t to the global-frame axes and to determine the resulting interaction-force components acting along the axes of the global frame, and (c) lastly, SIMPACK is asked to provide a rotation matrix relating the from-marker to the global frame and this rotational matrix is used to compute the interaction-force

components acting along the axes of the from-marker. These components of the force are returned by uforce20 to SIMPACK and, then SIMPACK-solver applies the same forces but with a negative sign to the to-marker.

Calculation of the reaction torques is somewhat complex and not very intuitive. In the remainder of this section, a brief description is provided of the procedure used for the calculation of the interaction torques within uforce20 and for their return to SIMPACK. To facilitate this description a simple schematic of the inner race and one of the rollers is given in Figure 4-4. For simplicity, the roller is placed on top of the inner-race so that only the z-component of the position vector of its from-marker relative to the inner-race to-marker is non-zero. Also, the inner-race is assumed to rotate clockwise (i.e. in the +y direction) while, at the instant in question, the roller is assumed to be stationary. The tangential component of the interaction force acting on the roller, $F_{t,roller}$ is thus aligned in the +x direction. By virtue of the newton's action/reaction law, the corresponding force acting on the inner race is, $F_{t,race} = -F_{t,roller}$. Using the standard definition for the torque as a cross product between the position vector (of the point at which the force is applied relative to the origin of the marker in question) and the force, the only non-zero (y) component of the interaction torques acting on the rolling element and the inner race are as follows:

$$\tau_{roller} = -r_{roller} \times F_{t,roller} = -R_{roller} F_{t,roller} \tag{4–7}$$

$$\tau_{race} = r_{race} \times F_{t,race} = R_{in-race}\left(-F_{t,roller}\right) = -R_{in-race} F_{t,roller} \tag{4–8}$$

These torques should be applied using uforce20 to the respective from- and to-markers. However, SIMPACK solver itself applies to the from-marker the so-called reaction torque defined as a cross product of the to-marker origin relative to the from-marker origin and $F_{t,roller}$, i.e.

$$\tau_{reaction} = -\left(R_{roller} + R_{in-race}\right) F_{t,roller} \tag{4–9}$$

Since $\tau_{reaction}$ is not equal to τ_{roller} and no reaction torque is prescribed to the to-marker, one must return to SIMPACK, not the actual torques acting on the from- and to-markers, but rather corrections to $\tau_{reaction}$ which should yield correct values for τ_{roller} and τ_{race}. This must be done while recognizing that single torque (vector) returned by uforce20 to SIMPACK is applied to the from-marker and a negative value of this torque to the to-marker. Simple examination of Eqs. (4–5) to (4–7) reveals that the torque correction term (i.e. the torque which uforce20 will return to SIMPACK) should be:

$$\tau_{correction} = R_{in-race} F_{t,roller} \tag{4–10}$$

The net torque acting on the from-marker is then:

$$\tau_{roller,net} = \tau_{reaction} + \tau_{correction} = -R_{roller} F_{t,roller} = \tau_{roller} \tag{4–11}$$

Likewise, since $-\tau_{correction}$ is applied to the to-marker, the net torque acting on this marker is:

$$\tau_{race,net} = -\tau_{correction} = -R_{in-race} F_{t,roller} = \tau_{race} \tag{4–12}$$

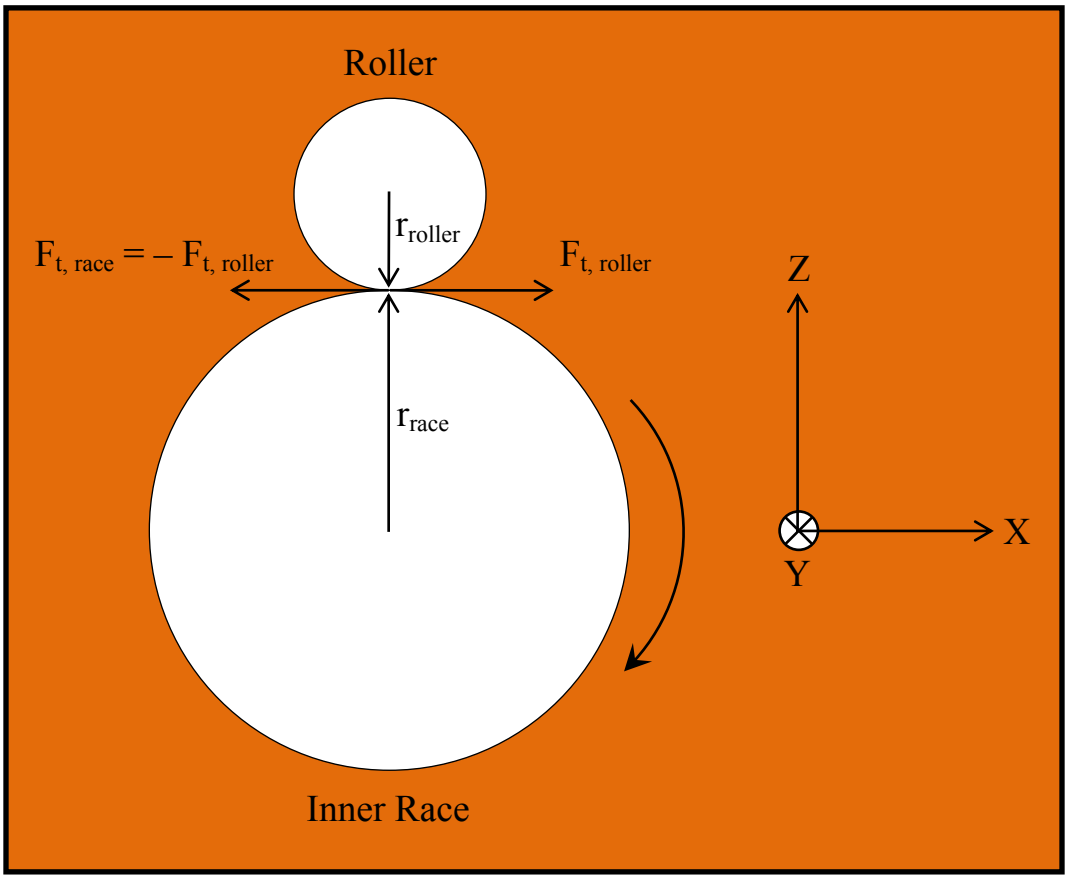

Figure 4-4 A schematic of the single-roller/inner-race contact pair used to explain the way the contact-interaction torque is calculated within uforce20 and returned to SIMPACK.

Rolling-elements/bearing-cage contact interactions

Force elements are also used to model interactions between each rolling element and the respective pocket of the cage. One such force element was used per rolling element. In other words, a single force element is used to model the interaction of a rolling element with both leading and trailing bridges of respective cage pocket. To formulate a rolling-element/cage force element, the from-marker is placed at the center of the rolling element. The respective pocket was positioned symmetrically with respect to the rolling and the to-marker placed at the center of the pocket. In this way, the two markers are made initially made coincident. The orientation of the two markers is set to coincide with the radial, tangential and bearing-axial directions where, the radial and tangential directions are defined by the initial position of the rolling element and the bearing-element axis. To determine the interaction force, angular positions of the rolling-element and the cage-pocket center are monitored. When the magnitude of the difference in these two angular positions, $abs(\theta)$, is larger than the one corresponding to the initial clearance between the rolling-element and the cage-pocket bridge, $abs(\theta_{critical})$, the interaction force (in the global frame) is assumed to acquire non-zero values as:

$$\begin{bmatrix} F_x \\ F_y \\ F_z \end{bmatrix} = K_{roller-cage}\left(abs(\theta) - abs(\theta_{critical})\right)\left(R_{in-race} + R_{roller}\right)\begin{bmatrix} \dfrac{x_{cage} - x_{roller}}{\left|r_{cage} - r_{roller}\right|} \\ 0 \\ \dfrac{z_{cage} - z_{roller}}{\left|r_{cage} - r_{roller}\right|} \end{bmatrix} \quad (4\text{–}13)$$

where $K_{roller-cage}$ denotes spring constant, r is the position vector of the respective marker, x and z the corresponding components of this vector.

Potential problem with the implementation of Eq. (4–13) in uforce20 is that angular positions of roller and/or cage can abruptly change by $+/-2\pi$ upon completion of a full revolution. To identify such instances and prevent erroneous determination of the roller/cage interaction force, $abs(\theta)$ was monitored closely for its abrupt change and an excessive value. Details of this procedure can be inferred by analyzing uforce20 source code provided in the APPENDIX A.

4.3.4 Construction of the User-defined Force Element

The In accordance with the SIMPACK user-subroutine format, uforce20 is composed of three individual subroutines: (a) uforce20_type; (b) uforce20_setup; (c) uforce20. Within the uforce20_type subroutine, the following tasks are accomplished: (i) user force-element name is defined which is recognized by the SIMPACK GUI; (ii) global variables are defined by including "simpack.ins" file; (iii) the nature of the element, force vs control is defined; and (iv) the number of model parameters, dynamic states, output variables are specified. Within the uforce20_setup subroutine, the following tasks are accomplished: (i) element specific parameters are defined; (ii) parameters are checked by carrying out a pre-processing procedure; and (iii) names of the parameters, dynamic states and output variables are specified. Within the uforce20 subroutine, the main task is to, compute the forces and torques in the reference frame of the body associated with the from-marker and return it to SIMPACK.

A script of the source codes of the three subroutines mentioned above for the cases of force elements developed and used in the present work is provided in the APPENDIX A.

4.3.5 Kinematics-based Derivation of the Zero-Slip Roller Angular Velocity

In this section, an analytical procedure is used to derive equations relating the revolving and rotational speeds of the rolling elements in contact with the inner and the outer races under zero-slip conditions and the geometrical and kinematic parameters of the rolling elements and the races. This procedure starts by defining the slip velocities at the rolling-element/inner-race and rolling-element/outer-race surfaces and setting them both to zero as:

$$\begin{aligned} V_{s-in} &= \omega_{in-race} R_{in-race} - V_{r-rev}^{in-race} + \omega_{r-rot} R_{roller} \\ &= \omega_{in-race} R_{in-race} - V_{r-rev} \frac{R_{in-race}}{\left(R_{in-race} + R_{roller}\right)} + \omega_{r-rot} R_{roller} \end{aligned} \tag{4–13}$$

$$\begin{aligned} V_{s-out} &= \omega_{out-race} R_{out-race} - V_{r-rev}^{out-race} - \omega_{r-rot} R_{roller} \\ &= \omega_{out-race} R_{out-race} - V_{r-rev} \frac{R_{out-race}}{\left(R_{out-race} - R_{roller}\right)} - \omega_{r-rot} R_{roller} \end{aligned} \tag{4–14}$$

Eqs. (4–11) and (4–12) represent a linear system of two algebraic equations with two unknowns which can be readily solved (analytically), to yield solutions for the unknown variables:

$$V_{r-rev} = \left(\frac{R_{out-race} - R_{roller}}{R_{in-race} + R_{out-race}} \right) \left(\omega_{in-race} R_{in-race} + \omega_{out-race} R_{out-race} \right) \tag{4–15}$$

$$\omega_{r-rot} = \left(\frac{R_{out-race} R_{in-race}}{R_{roller} \left(R_{in-race} + R_{out-race} \right)} \right) \left(\omega_{out-race} - \omega_{in-race} \right) \tag{4–16}$$

To validate the uforce20 code, MBD simulations are carried out within SIMPACK using a number of combinations of $\omega_{in-race}$ and $\omega_{out-race}$. After a transient period each simulation would begin to approach the steady (zero-slip) condition associated with nearly constant values of V_{r-rev} and ω_{r-rot}. The computed values of these quantities are then compared with their analytical counterparts as defined respectively by Eqs. (4–13) and (4–14) to, judge the validity of

the contact-interaction force-element constitutive relations in uforce20. The results of this comparison are presented in the next section.

4.4. Results and Discussion

As explained earlier, the work presented in this chapter was aimed at constructing the foundation for a more comprehensive MBD computational investigation of the dynamic behavior of a prototypical wind-turbine gear-box bearing element. The kinematic and kinetic behavior of the roller bearings particularly during particular events/scenarios such as extreme gust, wind-turbine emergency shutdown, wind-turbine restart, etc. is believed to be one of the main contributors to the root cause of roller-bearing premature failure. The main objective of the work presented in this chapter is to successfully implement user-defined contact-interaction force elements into a SIMPACK user subroutine uforce20. The success of this implementation is shown in Figure 4-5 and Figure 4-6. Figures 4–5 and 4–6 show respectively the variations of V_{r-rev} and ω_{r-rot} with $\omega_{in-race}$ and $\omega_{out-race}$, as contour plots. In the case of each figure, part (a) shows the results as predicted by the analytical procedure presented in 4.3.5 while, part (b) shows the corresponding results obtained directly through the use of uforce20 and SIMPACK. A comparison of the results displayed in parts (a) and (b) of Figures 4–5 and 4–6 reveals that the present implementation of the contact-interaction force elements in uforce20 and linking of this subroutine with SIMPACK is correct.

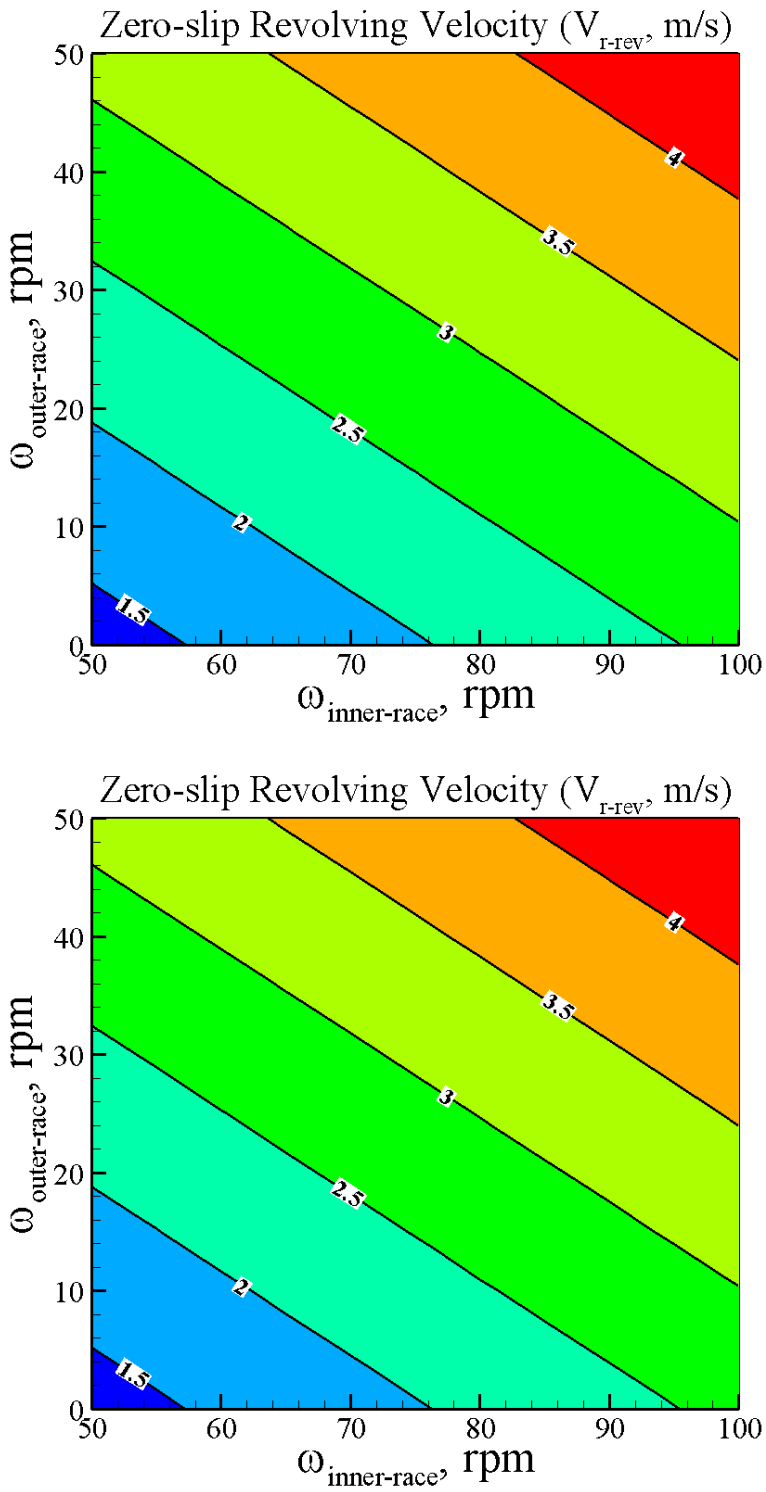

Figure 4-5 The effect of the inner-race rotational speed and the outer-race rotational speed on the no-slip revolving velocity of the rollers in the case of the roller-bearing being analyzed: (a) an analytical kinematics-based solution; and (b) the numerical uforce20/SIMPACK based solution.

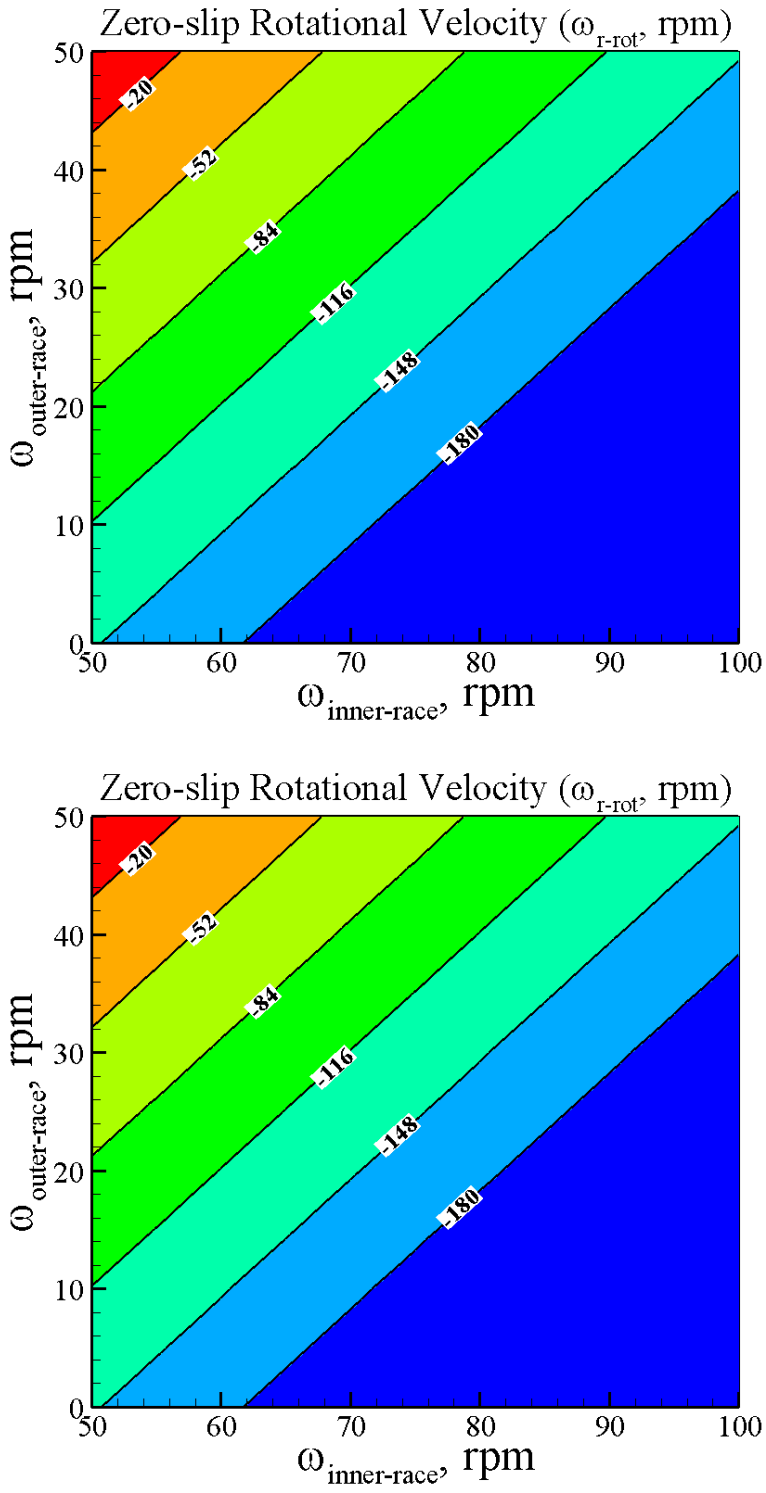

Figure 4-6 The effect of the inner-race rotational speed and the outer-race rotational speed on the no-slip angular (rotational) velocity of the rollers in the case of the roller-bearing being analyzed: (a) an analytical kinematics-based solution; and (b) the numerical uforce20/SIMPACK based solution.

The effect of the inner-race rotational velocity, for the case of the initially stationary rolling elements and a zero rotational-velocity of the outer race, on the slip velocity at the interfaces between the rolling elements and: (a) the inner; (b) the outer race is depicted in Figures 4–7(a)–(b), respectively. Examination of the results displayed in Figure 4-7(a) shows that: (a) as expected, the initial slip velocity at the rolling-element/inner-race interface is simply a product of the inner-race rotational velocity and the inner-race radius; and (b) the time required for the roller-bearing to attain the no-slip state increases with an increase in the initial slip-velocity at the rolling-element/inner-race interface. Furthermore, examination of the results displayed in Figure 4-7(b) shows that: (a) as expected, the initial slip velocity at the rolling-element/outer-race interface is zero; and (b) as the simulation proceeds, the slip velocity at the rolling-element/outer-race interface first begins to deviate from zero, attains the largest magnitude, and then gradually begins to approach its zero value (corresponding to the no-slip condition at the rolling-element/outer-race interface).

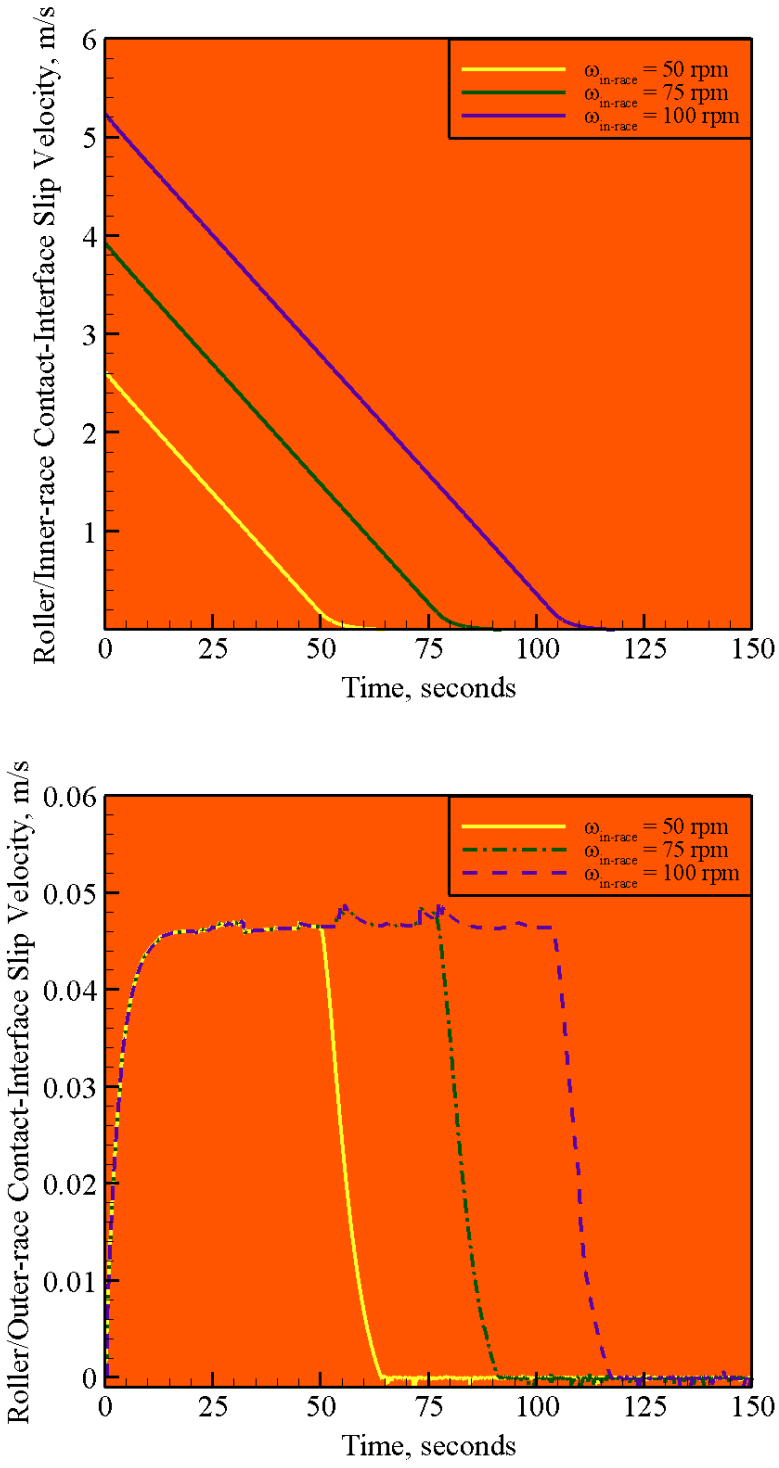

Figure 4-7 The effect of (constant) inner-race rotational velocity, for the case of the initially stationary rolling elements and always stationary outer race, at the interfaces between the rolling elements and: (a) the inner race; (b) the outer race.

4.5. Summary and Conclusions

Based on the results obtained in this portion of the work, the following main summary remarks and conclusions can be drawn:

1. To facilitate future work related to the effect of unfavorable bearing kinematics on the premature failure of wind-turbine gearboxes, a multi-body dynamics (MBD) computational model has been developed for a prototypical roller bearing.

2. While constructing the MBD model for the bearing, standard built-in options available in SIMPACK – a general purpose MBD code, such as rigid bodies, joints and kinematic constraints are utilized.

3. To account more realistically for the interactions between rolling elements and the inner/outer race as well as between rolling elements and cage/retainer, a set of user defined force elements is constructed. To link these elements with SIMPACK solver, a user subroutine uforce20 has been developed and validated.

4. The validity of the overall bearing-element MDB model is validated by comparing its predictions and the corresponding close-form analytical results pertaining to the no-slip rotational and revolving velocities of the rolling elements. In addition, the model is used to show the effect of the magnitude of the transient-stage perturbation on the time required for the bearing to regain its steady no-slip condition.

4.6. References

1. M. Grujicic, B. Pandurangan, Y. Huang, B. A. Cheeseman, W. N. Roy, and R. R. Skaggs, "***Impulse Loading Resulting from Shallow Buried Explosives in Water-saturated Sand***", Journal of Materials: Design and Applications 221: 21-35, (2007a).

2. M. Grujicic, B. Pandurangan, U. Zecevic, K.L. Koudela, and B. A. Cheeseman, "***Ballistic Performance of Alumina/S-2 Glass-Reinforced Polymer-Matrix Composite Hybrid Lightweight Armor Against Armor Piercing (AP) and Non-AP Projectiles***," Multidiscipline Modeling in Materials and Structures 3: 287–312, (2007b).

3. M. Grujicic, and W.C. Bell, "***A Computational Analysis of Survivability of a Pick-Up Truck Subjected to Mine Detonation Loads***," Multidiscipline Modeling in Materials and Structures, 7: 386-423, (2011a).

4. W. D. Musial, S. Butterfield, and B. McNiff, "***Improving Wind Turbine Gearbox Reliability***," Proceedings of the European Wind Energy Conference, Milan, Italy, May 7–10, 2007.

5. ISO/IEC 81400-4:2005, "***Wind Turbines – Part 4: Standard for Design and Specification of Gear-boxes***," International Organization for Standardization, Geneva, Switzerland, 2005.

6. ISO 15243:2004, "***Rolling bearings – Damage and failures – Terms, characteristics and causes***," International Organization for Standardization, Geneva, Switzerland, 2004.

7. SKF Company Brochure. "***Bearing Failures and Their Causes***," Publication Number 401 E. Accessed August 8, 2013. http://www.skf.com/group/knowledge-centre/aptitude-exchange/articles/index.html

8. K. Stadler and A. Stubenrauch, "***Premature Bearing Failures in Industrial Gear-boxes***," National Renewable Energy Laboratory. Accessed on August 8, 2013. www.nrel.gov/wind/grc/pdfs/12_premature_bearing_failures.pdf

9. SIMPACK Release 9.3, "***SIMPACK Reference Guide***," SIMDOC v9.31, January 2013.

10. W. Tu, Y. Shao, and C. K. Mechefske, "***An analytical model to investigate skidding in rolling element bearings during acceleration***," Journal of Mechanical Science and Technology, 26 (8), 2451-2458, 2012.

11. T. A. Harris, and M. N. Kotzalas, "***Essential Concepts of Bearing Technology, Fifth Edition***," CRC Press, 2006, ISBN: 978-1-4200-0659-9.

CHAPTER 5: CONCLUSIONS AND SUGGESTIONS FOR FUTURE WORK

5.1. Conclusions

While each of the chapters 2 through 4 contains a summary of the conclusions resulting from the work reported in these chapters, a list of more general conclusions arrived at the end of the present work is presented in the remainder of this section. This list includes:

1. Computer aided engineering (CAE) analysis and material selection methods and tools have achieved the level of physical fidelity, computational robustness and accuracy that they can greatly help in the design of a new horizontal axis wind turbine blades. Specific areas in which these methods and tools could be particularly beneficial include predictions of the blade's structural integrity, its durability and reliability. The methods and tools identified in the present work as having key role include finite element analysis, Rainflow analysis, Goodman diagram, Miner's rule, material selection charts and indices, etc.
2. Computer aided engineering methods and tools can also play a major role in helping identify the root cause method of the wind-turbine gearbox premature failure. In the present work, this point was demonstrated by analyzing a particular mode of gearbox failure (i.e. gear-tooth bending fatigue). To model this failure mode, advanced finite-element structural/stress analysis is combined with the computational procedures developed for prediction of fatigue-crack initiation and growth processes (and ultimate failure). The results obtained clearly revealed the effect of the service-loading conditions (as quantified by the transferred-torque and the gear-misalignment) on the fatigue-service-life of the gearbox.
3. Since unfavorable kinematics of wind-turbine gear-box bearing elements is believed to be one of the root causes of their premature failure. The starting point in approaching this

complex problem is establishment of reliable multi-body dynamics (MBD) model for a prototypical cylindrical roller bearing. One of the most challenging aspects of such roller-bearing MBD model is the establishment and evaluation of the forces and torques generated as a result of contact interactions between rolling elements and inner-outer races, as well as between the rolling elements and the cage/retainer. Such interactions are quantified and validated in the present work through the use of a user-defined MBD force element.

5.2. Suggestions for Future Work

The work reported in this thesis can be extended in a multiple directions. In the remainder of this sub-section, one of such directions per topic covered in this thesis is briefly discussed.

1. The work presented in Chapter 2, can be naturally extended in the direction of a coupling the computational analyses developed with a multi-objective/multi-constraint engineering optimization analysis. Within such an optimization analysis, various aspects of the wind-turbine performance such as its structural integrity, durability, reliability, weight, cost, etc. can be simultaneously optimized by varying different blade-design and material parameters while ensuring that the design and functional constraints are satisfied.
2. In the case of the work presented in Chapter 3, one extension would involve modeling of the structural behavior (including failure) of wind turbine gears under the conditions of bearing-debris being caught between the meshing teeth of the wind-turbine gears. These conditions are occasionally found to lead to gear misalignment, excessive tooth-loading and ultimate (premature) failure.
3. The work presented in Chapter 4 should be extended in the direction of modeling the effect of unfavorable bearing kinematics (associated with various wind turbine transient events, e.g. occasional gusts, emergency shutdown, startup, etc.) on the initiation of surface and sub-surface damage within the bearing races, the phenomenon which is believed to be closely related to the problem of wind-turbine gear-box roller-bearing premature failure.

APPENDIX A: USER-DEFINED FORCE ELEMENT – UFORCE20 SOURCE CODE

User Defined Force Element is developed which calculates Contact Forces developed within a Roller bearing, due to the interactions between the bearing elements. This subroutine contains commented lines to help understand the logic in the code. This is used for the model with 12 rolling elements to verfiy the analytical solution. Although the cage is present, it does not affect steady state values but a force element applies forces or torques on it.

```
!*******************************************************************************
!> SIMPACK User Force/Control Element Type 20
!> Author: Varun (Dr.Grujicic Research Team)
!*******************************************************************************

      subroutine uforce20_type( str_dim      !< [in ] name string length
     +                        , type_name !< [out] force type name
     +                        , ierr          !< [out] error code
     +                  )

#if defined(WINDOWS)
    !DEC$ ATTRIBUTES DLLEXPORT::uforce20_type
#endif

C -------------------------------------------------------------------
C Declaration of Global Variables
C -------------------------------------------------------------------
      implicit none
      include 'simpack.ins'

C -------------------------------------------------------------------
C Declaration of Interface Parameters
C -------------------------------------------------------------------
      integer :: str_dim
      integer :: ierr
      character(len=*) :: type_name

C -------------------------------------------------------------------
C Initialization
C -------------------------------------------------------------------
      ierr = 0
```

```
C -----------------------------------------------------------------------
C Execution
C -----------------------------------------------------------------------
     ! name  12345678901234567890123456789012345678901234567890'
     ! name of user-defined force element  '
     type_name = 'CRB Contact Forces      '

     call spck_df_FClass(fclass_force,ierr)  ! force element
     call spck_df_ForceParDim(10,ierr)       ! parameters
     call spck_df_ForceStDynDim(0,ierr)      ! dynamic states
     call spck_df_ForceOvDim(20,ierr)        ! output values

     return
     end subroutine

!******************** END OF SUBROUTINE uforce20_type ************************

     subroutine uforce20_setup( task       !< [in    ] |-1 | 5 | 0 | 1 | 2 | 4 | task flag
    +                         , par_dim    !< [in    ] | i | i | i | i | i | i | number of parameters
     +                        , stdyn_dim !< [in    ] | i | i | i | i | i | i | number of dynamic states
     +                        , ov_dim     !< [in    ] | i | i | i | i | i | i | number of output values
     +                        , str_dim    !< [in    ] | i | i | i | - | - | - | max. length of names
     +                        , id         !< [in    ] | i | i | i | i | i | i | element id
     +                        , mk_from    !< [in    ] | i | i | i | i | i | i | from-marker id
     +                        , mk_to      !< [in    ] | i | i | i | i | i | i | to-marker id
     +                        , par        !< [in,out] | i |i/o| i |i/o|i/o| i | parameters
     +                        , par_typ    !< [   out] | - | - | o | - | - | - | parameter types
     +                        , par_str    !< [   out] | - | - | o | - | - | - | parameter names
     +                        , par_u      !< [   out] | - | - | o | - | - | - | parameter unit types
     +                        , stdyn_str  !< [   out] | - | - | o | - | - | - | dynamic state names
     +                        , stdyn_u    !< [   out] | - | - | o | - | - | - | dynamic state unit types
     +                        , ov_str     !< [   out] | - | - | o | - | - | - | output value names
     +                        , ov_u       !< [   out] | - | - | o | - | - | - | output value unit types
     +                        , res_flg    !< [   out] | - | - | - | o | - | - | output flag
     +                        , stdyn_nr   !< [      ] | - | - | - | - | - | - | (obsolete)
     +                        , stroot_nr  !< [      ] | - | - | - | - | - | - | (obsolete)
     +                        , str_flg    !< [   out] | - | - | - | o | - | - | state reset flag
     +                        , ierr       !< [   out] | o | o | o | o | o | o | error code
     +                  )

#if defined(WINDOWS)
     !DEC$ ATTRIBUTES DLLEXPORT::uforce20_setup
#endif

C -----------------------------------------------------------------------
C Declaration of Global Variables
```

```
C ---------------------------------------------------------------------
      implicit none
      include 'simpack.ins'

C ---------------------------------------------------------------------
C Declaration of Interface Parameters
C ---------------------------------------------------------------------
      integer task
      integer par_dim
      integer stdyn_dim
      integer ov_dim
      integer str_dim
      integer id
      integer mk_from
      integer mk_to
      integer par_typ(par_dim)
      integer par_u(par_dim)
      integer stdyn_u(stdyn_dim)
      integer ov_u(ov_dim)
      integer res_flg
      integer stdyn_nr
      integer stroot_nr
      integer str_flg
      integer ierr
      double precision :: par(par_dim)
      character(len=*) :: par_str(par_dim)
      character(len=*) :: stdyn_str(stdyn_dim)
      character(len=*) :: ov_str(ov_dim)

C ---------------------------------------------------------------------
C Initialization
C ---------------------------------------------------------------------
      ierr = 0

C ---------------------------------------------------------------------
C task = -1 : Parameter-dependent Dimensions
C ---------------------------------------------------------------------
      if ( task .eq. -1 ) then
        continue

C ---------------------------------------------------------------------
C task = 0 : Names and Types
C ---------------------------------------------------------------------
      else if ( task .eq. 0 ) then

        ! initialise outputs
```

```
      !-------------------
      par_str(1:par_dim) = ' '
      par_typ(1:par_dim) = knodef
      par_u(1:par_dim) = knodef
      stdyn_str(1:stdyn_dim) = ' '
      stdyn_u(1:stdyn_dim) = knodef
      ov_str(1:ov_dim) = ' '
      ov_u(1:ov_dim) = knodef

      ! parameters
      ! ----------
      ! name '12345678901234567890123456789012 ' | parameter type          | unit type
      ! These parameter names will appear on the force element properties dialog box in
SIMPACK GUI
      par_str( 1) = 'Nominal_Length   ' ; par_typ( 1) = knr_double  ; par_u( 1) = Kp_length
      par_str( 2) = 'Normal_Stiffness ' ; par_typ( 2) = knr_double  ; par_u( 2) = Kp_stiffness
      par_str( 3) = 'Roller_Diameter  ' ; par_typ( 3) = knr_double  ; par_u( 3) = Kp_length
      par_str( 4) = 'Race_Diameter    ' ; par_typ( 4) = knr_double  ; par_u( 4) = Kp_length
      par_str( 5) = 'Race_Flag        ' ; par_typ( 5) = knr_integer ; par_u( 5) = Kp_undefined
      par_str( 6) = 'Critical_Angle   ' ; par_typ( 6) = knr_double  ; par_u( 6) = Kp_angle

      ! output values
      ! -------------
      ! name '12345678901234567890123456789012' | unit type
      ! These output values names appear on FE properties in SIMPACK GUI
      ov_str( 1) = 'Normal_Force    ' ; ov_u( 1) = Kp_force
      ov_str( 2) = 'Friction_Force  ' ; ov_u( 2) = Kp_force
      ov_str( 3) = 'Thrust_Force    ' ; ov_u( 3) = Kp_force
      ov_str( 4) = 'Friction_Torque ' ; ov_u( 4) = Kp_torque
      ov_str( 5) = 'Normal_Fx       ' ; ov_u( 5) = Kp_force
      ov_str( 6) = 'Normal_Fz       ' ; ov_u( 6) = Kp_force
      ov_str( 7) = 'Tangential_Fx   ' ; ov_u( 7) = Kp_force
      ov_str( 8) = 'Tangential_Fz   ' ; ov_u( 8) = Kp_force
      ov_str( 9) = 'Total_Fx        ' ; ov_u( 9) = Kp_force
      ov_str(10) = 'Total_Fz        ' ; ov_u(10) = Kp_force
      ov_str(11) = 'V_slip          ' ; ov_u(11) = Kp_velocity
      ov_str(12) = 'Roller_Angle    ' ; ov_u(12) = Kp_angle
      ov_str(13) = 'V_Rev_Roller    ' ; ov_u(13) = Kp_velocity
      ov_str(14) = 'Cage_Angle      ' ; ov_u(14) = Kp_angle
      ov_str(15) = 'cage_pos_x      ' ; ov_u(15) = Kp_length
      ov_str(16) = 'roller_pos_x    ' ; ov_u(16) = Kp_length

C ---------------------------------------------------------------------
C task = 1 : Element-specific Infos
C ---------------------------------------------------------------------
    else if ( task .eq. 1 ) then
```

```
      res_flg   = 3 ! output flag
      str_flg   = 0 ! state reset flag (see also spck_slv_StRstInit)
      stdyn_nr  = 0 ! Number of Force States
      stroot_nr = 0 ! Number of Root Functions

C -------------------------------------------------------------------
C task = 2 : Check Parameters and Pre-Processing
C -------------------------------------------------------------------
    else if ( task .eq. 2 ) then
      continue

C -------------------------------------------------------------------
C task = 4 : Final Call
C -------------------------------------------------------------------
    else if ( task .eq. 4 ) then
      continue

C -------------------------------------------------------------------
C task = 5 : Default Parameters
C -------------------------------------------------------------------
    else if ( task .eq. 5 ) then
      continue
    end if

    return
    end subroutine

!*********************** END OF SUBROUTINE uforce20_setup ********************

    subroutine uforce20( task       !< [in    ] | 0 | 1 | 2 | 3 | 4 | task flag
   +           , par_dim     !< [in    ] | i | i | i | i | i | number of parameters
   +           , uin_dim     !< [in    ] | i | i | i | i | i | number of u-vector components
   +           , stdyn_dim   !< [in    ] | i | i | i | i | i | number of dynamic states
   +           , stroot_dim  !< [in    ] | i | i | i | i | i | number of root states
   +           , ov_dim      !< [in    ] | i | i | i | i | i | number of output values
   +           , id          !< [in    ] | i | i | i | i | i | element id
   +           , par         !< [in    ] | i | i | i | i | i | parameters
   +           , mk_from     !< [in    ] | i | i | i | i | i | from-marker id
   +           , mk_to       !< [in    ] | i | i | i | i | i | to-marker id
   +           , time        !< [in    ] | i | i | i | i | i | time
   +           , uin         !< [in    ] | i | i | i | i | i | u-vector
   +           , stdyn       !< [in,out] | i | i | i | i |i/o| dynamic states
   +           , stroot      !< [in,out] |i/o| i | i | i |i/o| root states
   +           , stdynd      !< [   out] | o | - | - | - | - | dynamic state derivatives
   +           , force       !< [   out] | o | - | - | - | - | force vector acting at from-marker w.r.t. from-brf
   +         , torque    !< [   out] | o | - | - | - | - | torque vector acting at from-marker w.r.t. from-brf
```

```
     +         , ov         !< [   out] | o | - | - | - | - | output values
     +         , valroot    !< [   out] | - | o | - | - | - | root function values
     +         , ierr       !< [   out] | o | o | o | o | o | error code
     +                 )

#if defined(WINDOWS)
    !DEC$ ATTRIBUTES DLLEXPORT::uforce20
#endif

C -----------------------------------------------------------------------
C Declaration of Global Variables
C -----------------------------------------------------------------------
     implicit none
     include 'simpack.ins'

C -----------------------------------------------------------------------
C Declaration of Interface Parameters
C -----------------------------------------------------------------------
     integer task
     integer par_dim
     integer uin_dim
     integer stdyn_dim
     integer stroot_dim
     integer ov_dim
     integer id
     integer mk_from
     integer mk_to
     integer stroot(stroot_dim)
     integer ierr
     integer err

     double precision par(par_dim)
     double precision time
     double precision uin(uin_dim)
     double precision stdyn(stdyn_dim)
     double precision stdynd(stdyn_dim)
     double precision force(3)
     double precision torque(3)
     double precision ov(ov_dim)
     double precision valroot(stroot_dim)

     character(len=50) :: message

C -----------------------------------------------------------------------
C Declaration of Local Variables
C -----------------------------------------------------------------------
```

```
      double precision  zero
      parameter(zero = 0.0d+00)
      double precision  PI
      parameter(PI = 3.141592654)

      ! Input Parameters ----------
      double precision  Nominal_Length    ! The length of the force element (spring) at which normal force is zero
      double precision  Normal_Stiffness ! The stiffness of roller-race/-cage contact, normal to contact surface
      double precision  Roller_Diameter ! Diameter of the cylindrical rolling element
      double precision  Race_Diameter  ! Outer Diameter of the Inner Raceway and Inner Diameter of the Outer Raceway
      integer           Race_Flag       ! Flag used to detect which contact interface is being analyzed
      double precision  Critical_Angle   ! Critical value of angular displacement between cage and roller

      ! Variables to calculate position of roller center
      double precision  d_roller   ! distance between the roller center and the race center
      double precision  delta_r    ! difference between distance and the nominal length of the userFE
      double precision  xyz_cmp_roller(3) ! cmps of position vector of roller center relative to race center
      double precision  roller_pos_x     ! x position of the roller center
      double precision  roller_pos_y     ! y position of the roller center
      double precision  roller_pos_z     ! z position of the roller center

      ! Variables to calculate position of cage pocket center
      double precision  d_cage         ! distance between the roller center and the cage pocket center
      double precision  xyz_cmp_cage(3)! cmps of position vector of cage pocket center relative to race center
      double precision  cage_pos_x     ! x position of the cage pocket center
      double precision  cage_pos_y     ! y position of the cage pocket center
      double precision  cage_pos_z     ! z position of the cage pocket center
      double precision  delta_angle  ! difference between angular position of cage pocket center and roller center
      double precision  delta_cage   ! circumferential displacement between roller center and cage pocket center

      ! Variables to calculate distance between the roller center and the cage pocket center
      double precision  x_distance    ! difference between x-components of the roller-to-cage
      double precision  z_distance    ! difference between z-components of the roller-to-cage
      double precision  d_cage_roller ! distance between the roller center and cage pocket center

      ! Parameters to calculate velocities of rolling elements
      double precision  Omega_Roller     ! rotational velocity of the roller about its own axis
      double precision  Velocity_Roller  ! tangential (peripheral) velocity of the roller
```

```
      double precision  Omega_Race       ! rotational velocity of the race
      double precision  Velocity_Race    ! tangential (peripheral) velocity of the race
      double precision  Omega_Rev_Roller ! rotational velocity of the roller center (revolution) about bearing axis
      double precision  Tang_Vel_Roller  ! tangential velocity of roller center at the roller-race contact interface
      double precision  V_abs  ! magnitude of velocity of roller center relative to Global Ref. Frame
      double precision  V_ptp  ! magnitude of velocity of roller center relative to Global Ref, Frame
      double precision  V_cmp(3) ! cmps of velocity vector of roller center relative to Global Ref. Frame

      ! Parameters to evaluate the friction coefficient
      double precision  Min_Slip_Vel      ! Value of Slip Velocity beyond which Mu is constant
      double precision  Min_Friction_Coeff ! Value of Friction Coefficient when Slip Velocity = 0
      double precision  Max_Friction_Coeff ! Value of Friction Coefficient when Slip Velocity = Min Slip Vel
      double precision  Slope             ! Slope of the linear part of the curve
      double precision  Mu                ! Coefficient of Friction

      double precision  trmat_roller(3,3)  ! Transformation Matrix between global frame and roller center

      ! Output Parameters ----------
      double precision  Normal_Force ! Magnitude of force normal to roller-race/-cage contact interface
      double precision  Friction_Force  ! Magnitude of Force tangential to contact interface
      double precision  Thrust_Force    ! Magnitude of Force perpendicular to bearing plane
      double precision  Friction_Torque ! Magnitude of Torque applied to contacting bodies
      double precision  Normal_Fx       ! Normal Force component in x-dir of Global Ref. Frame
      double precision  Normal_Fz       ! Normal Force component in z-dir of Global Ref. Frame
      double precision  Tangential_Fx  ! Tangential Force component in x-dir of Global Ref. Frame
      double precision  Tangential_Fz  ! Tangential Force component in z-dir of Global Ref. Frame
      double precision  Total_Fx         ! Total Force component in x-dir of Global Reference Frame
      double precision  Total_Fz         ! Total Force component in z-dir of Global Reference Frame
      double precision  V_slip           ! Relative velocity at the roller-race contact interface
      double precision  Roller_Angle   ! Angle defining the angular position of the roller center
      double precision  V_Rev_Roller    ! translational velocity of the roller center
      double precision  Cage_Angle      ! Angle defining the angular position of the cage pocket

c ---------------------------------------------------------------------
c User defined parameters
c ---------------------------------------------------------------------
      Nominal_Length  = par( 1)
      Normal_Stiffness = par( 2)
      Roller_Diameter  = par( 3)
      Race_Diameter    = par( 4)
```

```
      Race_Flag          = par( 5)
      Critical_Angle     = par( 6)

C -------------------------------------------------------------------
C Initialization
C -------------------------------------------------------------------
      ierr = 0

C -------------------------------------------------------------------
C task = 0 : Determine force, torque and output values
C -------------------------------------------------------------------

      if ( task .eq. 0 ) then

c     ! Calculate the Normal Force ***************
c     ------------------------------------------------------------
        ! Roller-Race Contact Interface *************
        ! ----------------------------------------------------------
        ! Calculate angular position of Roller Center relative to z-axis of Global ($M_Isys)
        call SPCK_AV_DXYZ(d_roller,xyz_cmp_roller,mk_from,0,0,ierr)
        delta_r = d_roller - Nominal_Length
        roller_pos_x = xyz_cmp_roller(1)
        roller_pos_y = xyz_cmp_roller(2)
        roller_pos_z = xyz_cmp_roller(3)
        if (roller_pos_x.lt.zero) then
           Roller_Angle = 2*PI + atan2(roller_pos_x,roller_pos_z)
        else
           Roller_Angle = atan2(roller_pos_x,roller_pos_z)
        end if

        ! Calculate the magnitude of the Normal Force at roller-race contact interface
        if (Race_Flag.eq.1) then
           if (d_roller.lt.Nominal_Length) then
              Normal_Force = Normal_Stiffness*(-delta_r)**(3.0/2.0)
           else
              Normal_Force = zero
           end if
        else if (Race_Flag.eq.2) then
           if (d_roller.gt.Nominal_Length) then
              Normal_Force = -Normal_Stiffness*(delta_r)**(3.0/2.0)
           else
              Normal_Force = zero
           end if
        end if

        ! Calculate components of Normal Force in $M_Isys for roller-race contact interface
```

```
if (Race_Flag.eq.1.or.Race_Flag.eq.2) then
   Normal_Fx = Normal_Force * sin(Roller_Angle)
   Normal_Fz = Normal_Force * cos(Roller_Angle)
end if

! Roller-Cage Contact Interface **********************
! ------------------------------------------------------------------------
! Calculate angular position of Cage-Pocket Center relative to z-axis of $M_Isys
if (Race_Flag.eq.3) then
   call SPCK_AV_DXYZ(d_cage,xyz_cmp_cage,mk_to,0,0,ierr)
   cage_pos_x = xyz_cmp_cage(1)
   cage_pos_y = xyz_cmp_cage(2)
   cage_pos_z = xyz_cmp_cage(3)
   if (cage_pos_x.lt.zero) then
      Cage_Angle = 2*PI + atan2(cage_pos_x,cage_pos_z)
   else
      Cage_Angle = atan2(cage_pos_x,cage_pos_z)
   end if
else
   Cage_Angle = zero
end if

! Calculate distance between cage pocket center and roller center
! The vector is drawn from roller center to the cage pocket center
if (Race_Flag.eq.3) then
   x_distance = (cage_pos_x - roller_pos_x)
   z_distance = (cage_pos_z - roller_pos_z)
   d_cage_roller = sqrt(x_distance**2.0 + z_distance**2.0)
else
   cage_pos_x = zero
end if

! Calculate the magnitude of the Normal Force at roller-cage contact interface
if (Race_Flag.eq.3) then
   delta_angle = Roller_Angle - Cage_Angle
   if (delta_angle.lt.-PI) then
      Cage_Angle = Cage_Angle - 2*PI
   end if
   if (delta_angle.gt.PI) then
      Roller_Angle = Roller_Angle - 2*PI
   end if
   delta_angle = Roller_Angle - Cage_Angle
   delta_cage = (abs(delta_angle) - Critical_Angle)*d_cage
   if (abs(delta_angle).gt.Critical_Angle) then
      Normal_Force = (Normal_Stiffness/100)*(delta_cage)
   else
```

```
            Normal_Force = zero
          end if
        end if

        ! Calculate components of Normal Force in $M_Isys for roller-cage contact interface
        if (Race_Flag.eq.3) then
          if (d_cage_roller.eq.zero) then
            Normal_Fx = zero
            Normal_Fz = zero
          else
            Normal_Fx = Normal_Force * (x_distance)/d_cage_roller
            Normal_Fz = Normal_Force * (z_distance)/d_cage_roller
          end if
        end if

c   ! Calculate the Tangential Force ******************************
c   ------------------------------------------------------------------------------------
        ! Calculate Tangential Velocity of the roller at the contact interface
        ! Rotation ---------------------------------------
        call SPCK_AS_WY(Omega_Roller,mk_from,0,0,ierr)
        Velocity_Roller = Omega_Roller * (Roller_Diameter/2)

        ! Calculate Tangential Velocity of the race at the contact interface
        call SPCK_AS_WY(Omega_Race,mk_to,0,0,ierr)
        Velocity_Race = Omega_Race * (Race_Diameter/2)

        ! Calculate Translational Velocity of the roller center
        ! Revolution -------------------------------------------------
        call SPCK_AV_VXYZ(V_abs,V_ptp,V_cmp,mk_from,0,0,0,ierr)
        V_Rev_Roller = V_cmp(1) * cos(Roller_Angle)
     & - V_cmp(3) * sin(Roller_Angle)

        ! Calculate Tangential Velocity of roller center at contact interface
        Omega_Rev_Roller = V_Rev_Roller/d_roller
        Tang_Vel_Roller = Omega_Rev_Roller * (Race_Diameter/2)

        ! Calculate Slip Velocity between the surfaces at the contact interface
        if (Race_Flag.eq.1) then
          V_slip = Velocity_Roller + Velocity_Race - Tang_Vel_Roller
        else
          V_slip = -Velocity_Roller + Velocity_Race - Tang_Vel_Roller
        end if

        ! Calculate the Friction Coefficient which is a function of Slip Velocity
        Min_Slip_Vel = 0.2
        Min_Friction_Coeff = 0.0010
```

```
      Max_Friction_Coeff = 0.03
      Slope = Max_Friction_Coeff/Min_Slip_Vel

      if (abs(V_slip).le.Min_Slip_Vel) then
         Mu = Min_Friction_Coeff + Slope*abs(V_slip)
      else
         Mu = Max_Friction_Coeff
      end if

      ! Determine the direction of Friction Force based on the Slip Velocity
      if (Race_Flag.eq.1) then
         if (V_slip.gt.0.0) then
            Friction_Force = Mu*Normal_Force
         else
            Friction_Force = -Mu*Normal_Force
         end if
      elseif (Race_Flag.eq.2) then
         if (V_slip.gt.0.0) then
            Friction_Force = -Mu*Normal_Force
         else
            Friction_Force = Mu*Normal_Force
         end if
      else
         Friction_Force = zero
      end if

      ! Calculate the components of Tangential Force in Global Reference Frame ($M_Isys)
      Tangential_Fx = Friction_Force * sin(Roller_Angle + (PI/2))
      Tangential_Fz = Friction_Force * cos(Roller_Angle + (PI/2))

c     ! Calculate the Axial Force ******************
c     ------------------------------------------------------------

      ! Calculate Thrust Forces (Axial Direction)
      Thrust_Force = zero

c     ! Calculate Total Force **********************
c     ------------------------------------------------------------

      ! Calculate the components of Total Force in Global Reference Frame ($M_Isys)
      ! Roller-Race Contact Interface and Roller-Cage Contact Interface
      Total_Fx = Normal_Fx + Tangential_Fx
      Total_Fz = Normal_Fz + Tangential_Fz

c     ! Calculate the Torque ***********************
c     ------------------------------------------------------------
```

```
      ! Calculate Moment (Torque about the roller y-axis)
      Friction_Torque = Friction_Force*(Race_Diameter/2)

c     ! Transform the Forces into Roller BRF ("From" Body BRF)
c     ------------------------------------------------------------------------
      call SPCK_AV_TrMat(trmat_roller,mk_from,0,ierr )

      ! Assign force values using transpose of trmat_roller
      ! ---------------------------------------------------
      force(1) = trmat_roller(1,1)*Total_Fx
     & + trmat_roller(2,1)*Thrust_Force + trmat_roller(3,1)*Total_Fz

      force(2) = trmat_roller(1,2)*Total_Fx
     & + trmat_roller(2,2)*Thrust_Force + trmat_roller(3,2)*Total_Fz

      force(3) = trmat_roller(1,3)*Total_Fx
     & + trmat_roller(2,3)*Thrust_Force + trmat_roller(3,3)*Total_Fz

      ! Assign torque values
      ! --------------------------------
      torque(1) = zero
      torque(2) = Friction_Torque
      torque(3) = zero

      if (Race_Flag.eq.3) then
         torque(1) = zero
         torque(2) = zero
         torque(3) = zero
      end if

      ! Update output values
      ! ----------------------------
      ov(1) = Normal_Force
      ov(2) = Friction_Force
      ov(3) = Thrust_Force
      ov(4) = Friction_Torque
      ov(5) = Normal_Fx
      ov(6) = Normal_Fz
      ov(7) = Tangential_Fx
      ov(8) = Tangential_Fz
      ov(9) = Total_Fx
      ov(10) = Total_Fz
      ov(11) = V_slip
      ov(12) = Roller_Angle
      ov(13) = V_Rev_Roller
```

```
        ov(14) = Cage_Angle
        ov(15) = cage_pos_x
        ov(16) = roller_pos_x
        continue

C -------------------------------------------------------------------
C task = 1 : Evaluate root functions
C -------------------------------------------------------------------
      else if ( task .eq. 1 ) then
        continue

C -------------------------------------------------------------------
C task = 2 : Perform state reset after root state switch
C -------------------------------------------------------------------
      else if ( task .eq. 2 ) then
        continue

C -------------------------------------------------------------------
C task = 3 : Determine algebraic state residuals
C -------------------------------------------------------------------
      else if ( task .eq. 3 ) then
        continue

C -------------------------------------------------------------------
C task = 4 : Initialise states after calculation of consistent states
C -------------------------------------------------------------------
      else if ( task .eq. 4 ) then
        continue
      end if

      return
      end subroutine

!************************ END OF SUBROUTINE uforce20 ************************
```